UNIVERSIDADE FEDERAL DO RIO DE JANEIRO
OBSERVATÓRIO DO VALONGO

Ultra-high energy cosmic ray phenomenology using data collected by the Pierre Auger Observatory

Cynthia Ahiezer Vizcarra Ventura

Dissertação de Mestrado apresentada ao Programa de Pós-Graduação em Astronomia da Universidade Federal do Rio de Janeiro - UFRJ, como parte dos requisitos necessários à obtenção do título de Mestre em Ciências (Astronomia).

Advisor: **João R. T. de Mello Neto**

Co-Advisor: **Rogerio Menezes de Almeida**

Rio de Janeiro

June 2017

V864 Vizcarra Ventura, Cynthia Ahiezer

Ultra high energy cosmic ray phenomenology using data collected by the Pierre Auger Observatory / Cynthia Ahiezer Vizcarra Ventura - Rio de Janeiro: UFRJ/OV, 2017.

122f.

Orientador: João R. T. de Mello Neto

Coorientador: Rogerio Menezes de Almeida

Dissertação (mestrado) - UFRJ / Observatório do Valongo / Programa de Pós-graduação em Astronomia, 2017.

Referências Bibliográficas: f. 124-145.

1. Raios cósmicos. 2. Anisotropia. 3. Observatório Pierre Auger. I. Ramos, Torres de Mello Neto, João, Orientador. II. Almeida, Rogerio Menezes de, Co-orientador. III. Universidade Federal do Rio de Janeiro, Observatório do Valongo, Programa de Pós-graduação em Astronomia. IV. Ultra high energy cosmic ray phenomenology using data collected by the Pierre Auger Observatory.

Acknowledgements

I want to thank everyone who made this work possible with their assistance and their support.

First of all, special thanks go to my mother Gaby, and to my brothers Gustavo and Emiliano. Their encouragement during my studies and their support in my professional choices have been fundamental. I am blessed with such a nice family whom I love, and who I know love me. Thanks you for always being there for me and for giving me the feeling that, no matter what happens, I always have a save place to return to.

I would like to thank to my advisor, João T. de Mello Neto, for his excellent ideas and great support and useful discussions. Thanks for always being so understanding during these two years.

I would also like to thank to my co-advisor Rogerio Menezes de Almeida for his collaboration, for his limitless helps in every step of my work from the beginning to the end and time for all the Skype meetings and helpful discussions.

Here I would like to thank members of cosmic ray group of the IF-UFRJ, for always making me feel welcome here, for the help they provided over and over again, and for the fun times we had together. Thank you Ugo Giaccari, Bruno Lago, Jaime Souza. And, of course, my warmest thanks also to Rafael Batista and Eliel Alves for their help in understanding the CRPropa3 program used in this work and their help with programming-related topics. Their companionship and support have been invaluable to me.

I would like to express my deepest gratitudes to my boyfriend, Saúl, thanks for being so understanding and supportive during all the years of my graduate and postgraduate studies. I am also very thankful for all your help with my dissertation. Your support and encouragement is indeed the greatest.

There are too many friends who had great influences in my life to name them all individually, but I would like to thank Fabiola for always being there; Malu for the great moments we had during our graduate years, even though I moved away our friendship has lasted and even became stronger. Thank you for coming to visit me here and thank you for all the support and fun times; Astrid for being a true friend in the most important years of my life and my many classmates both at UNSA and OV-UFRJ.

Next I would like to thank also the Valongo Observatory (OV-UFRJ), for its hospitality during these two years, and all the friends with whom I have spent a very productive and pleasant period of my postgrade studies.

To the secretary of Pos-Graduation Claudia F., my gratitude for all the help and patience.

Finally I would like to thank CAPES for financial support.

I dedicate this work to all my family for their endless love and support.

"Study hard what interests you
the most in the most
undisciplined, irreverent and
original manner possible."
Richard Feynman

Resumo

Fenomenologia dos raios cósmicos de ultra alta energia usando os dados coletados pelo Observatório Pierre Auger

Cynthia Ahiezer Vizcarra Ventura

Orientador: João R. Torres de Mello Neto

Coorientador: Rogerio Menezes de Almeida

Resumo da Dissertação de Mestrado submetida ao Programa de Pós-graduação em Astronomia da Universidade Federal do Rio de Janeiro - UFRJ, como parte dos requisitos necessários à obtenção do título de Mestre em Ciências (Astronomia).

Estudos recentes realizados pela Colaboração Pierre Auger utilizando a análise de Rayleigh em ascensão reta e azimute com energias acima de 8 EeV (1EeV $= 10^{18}$ eV) mostram um desvio da isotropia com amplitude dipolar de $d = 0.073 \pm 0.015$. Não se observa um desvio significativo da isotropia no bin de energia entre 4 e 8 EeV. Embora existam ainda muitas incertezas quanto à origem e composição dos UHECRs, há um consenso de que quase todos eles são partículas extra-galácticas carregadas. Essas partículas interagem com fótons da radiação de fundo extragaláctico difuso afetando seu espectro de energia e composição quimica. Supondo que o fluxo de raios cósmicos provenientes de nosso universo local é proporcional ao número de galáxias próximas, enquanto o fluxo proveniente de distâncias maiores é isotrópico, estudamos através de simulações de Monte Carlo as implicações dos dados do Observatório Pierre Auger sobre cenários astrofísicos, assumindo perdas de energia usuais e efeitos de Violação da Invariância de Lorentz ao longo da propagação dos raios cósmicos.

Palavras-chave: Raios Cósmicos. Observatório Pierre Auger. Anisotropia. Violação da Invariância de Lorentz.

Abstract

Ultra-high energy cosmic ray phenomenology using data collected by the Pierre Auger Observatory

Cynthia Ahiezer Vizcarra Ventura

Orientador: João R. Torres de Mello Neto

Coorientador: Rogerio Menezes de Almeida

Abstract da Dissertação de Mestrado submetida ao Programa de Pós-graduação em Astronomia da Universidade Federal do Rio de Janeiro - UFRJ, como parte dos requisitos necessários à obtenção do título de Mestre em Ciências (Astronomia).

Recent studies performed by the Pierre Auger Collaboration using the two Rayleigh analysis in the right ascension and azimuth angles with energies above 8 EeV (1EeV $= 10^{18}$ eV) show a departure from isotropy with dipolar amplitude of d $= 0.073 \pm 0.015$. No significant departure from isotropy is observed in the energy bin between 4 and 8 EeV. While there are still many uncertainties about the origin and composition of UHECRs, there is a consensus that almost all of them are extra-galactic charged particles. Those particles interact with photons of the diffuse extragalactic background radiation affecting their energy spectrum and mass composition. Assuming that the flux of cosmic rays coming from our local universe is proportional to the number of nearby galaxies while the flux coming from larger distances is isotropic, we studied through Monte Carlo simulations the implications of the auger data on astrophysical scenarios, assuming usual energy losses and the effects of Lorentz Invariance Violations along the propagation of cosmic rays.

Keywords: Cosmic Rays. Pierre Auger Observatory. Anisotropy. Lorentz invariance violations.

Contents

List of Figures

List of Tables

Abbreviations

AGASA	The **A**keno **G**iant **A**ir **S**hower
AGN	**A**ctive **G**alactic **N**uclei
CLF	**C**entral **L**aser **F**acility
CIB	**C**osmic **I**nfrared **B**ackground
CMB	**C**osmic **M**icrowave **B**ackground radiation
CR	**C**osmic **R**ay
DAQ	**D**ata **A**cquisition **S**ystem
EBL	**E**xtragalactic **B**ackground **L**ight
EGMF	**E**xtragalactic **M**agnetic **F**ields
FADC	**F**lash **A**nalog to **D**igital **C**onverter
FD	**F**luorescence **D**etector
SD	**S**urface **D**etector
GZK	**G**reisen-**Z**atsepin-**Kuzmin** effect
NKG	**N**ishimura **K**amata and **G**reisen lateral distribution function
SNR	**S**upernova **R**emnants
GMF	**G**alactic **M**agnetic **F**ields
GRB	**G**amma-**R**ay **B**ursts
HIRES	**H**igh **R**esolution **F**ly's **E**ye **E**xperiment
HEAT	**H**igh **E**levation **A**uger **T**elescopes
IGM	**I**ntergalactic **M**edium
LDF	**L**ateral **D**istribution **F**unction
LIDAR	**L**ight **D**etection and **R**anging
PMT	**P**hoto-multiplier **T**ube
TA	**T**elescope **A**rray

UHECR	**U**ltra-**H**igh **E**nergy **C**osmic **R**ay
XLF	e**X**treme **L**aser **F**acility

Chapter 1

INTRODUCTION

Cosmic ray science is a very wide topic which is deeply rooted in many fields of physics, ranging from nuclear and particle physics to astrophysics and cosmology. Moreover, modern elementary particle physics in accelerators has evolved from studies of elementary particle processes in cosmic radiation.

Subatomic particles, such as nucleons, or atomic nuclei, that propagate from space to our planet, here defined as "cosmic rays", carry information that is revealing about the Universe. In particular, for those with energies E $\gtrsim$ 1 eV called Ultra-High Energy Cosmic Rays (UHECRs), the interactions with the Earth's atmosphere make it possible to estimate its energy and chemical composition, as well as to relate its arrival directions with potential astrophysical sources. The observed energy spectrum of UHECRs is close to a power law with index $\gamma \approx 3$. The slope of the observed energy spectrum of UHECRs shows a flattening at around 5×10^{18} eV, the so called "ankle". The origin of this ankle is still unclear. Proposed reasons for it are, amongst others, a transition from galactic to extragalactic sources, a transition from an extragalactic proton component to a different extragalactic heavy nuclei component, or a transition from lighter to heavier elements coming from the same sources (see Section 2.4).

There is a theoretical prediction of a pronounced cutoff in the spectrum of cosmic ray energies (GZK cutoff, see Section 2.3.3) due to interactions with the cosmic microwave background radiation. Because of this interaction, protons with energies above $\sim 4 \times 10^{19}$ eV (GZK energy) rapidly lose their energy through photo-pion production. The existence of such a cutoff implies that events above GZK energy must have an extremely low flux, much less than the flux of an E^{-3} decaying spectrum. The distance a particle can travel with energy above GZK energy defines the radius of the so-called GZK sphere. For protons, the sphere's radius of GZK is $\sim$ 100 Mpc. If events are detected with energies above the GZK energy and their flux is incompatible with the GZK cutoff, there is a probability of a violation of a fundamental principle, such as Lorentz invariance, or there are powerful sources within the surrounding sphere at a distance less than 100 Mpc.

The main motivation in this work is improve the combined fit analysis reported by the Pierre Auger Collaboration using energy spectrum and composition data. The data analysis of this thesis is based on two internal notes of the Pierre Auger Collaboration: *A combined fit of spectrum and composition Auger data considering a very simple case of Lorentz Invariance Violation along the cosmic ray propagation*, GAP 2017-012, R. A. Batista, F. Catalani, E. Alves Júnion, R. M. de Almeida, J. R. T. de Mello Neto, J. S. de Oliveira, U. Giaccari, B. Lago, R. G. Lang, C. Todero, and C. A. V. Ventura [R. A. Batista et al., 2017] and *Phenomenological analysis of the large scale anisotropies measured by the Pierre Auger Collaboration considering Lorentz Invariance Violation*, GAP 2017-016, R. A. Batista, F. Catalani, E. Alves Júnion, R. M. de Almeida, J. R. T. de Mello Neto, J. S. de Oliveira, U. Giaccari, B. Lago, R. G. Lang, C. Todero, and C. A. V. Ventura [R. M. de Almeida et al., 2017].

Outline of this Thesis

- In Chapter 2 we will discuss in greater detail cosmic rays physics making a brief historical review. A special focus of the current knowledge of UHECRs is presented including a description of the phenomenology of extensive air shower and a summary of the most used techniques developed for primary composition studies. Furthermore, the propagation of UHECRs through the intergalactic medium is discussed. This will include the exploration of fundamental particle physics at energies beyond those accessible at man-made accelerators.

- In Chapter 3 we present a detailed development of the Pierre Auger Observatory. The detection systems composed by surface detectors and fluorescence detectors wil be discussed as well as the methods used to calibrate each one emphasizing the great advantages of a hybrid design.

- In Chapter 4 of this thesis we will describe the phenomenological analyzes with the objective of inferring the characteristics of cosmic ray sources such as: energy spectrum and composition. First, we will review a combined fit reported by the Pierre Auger Collaboration [di Matteo, 2016] using energy spectrum and composition data. In the next, we will present our phenomenological analyzes to improve this result, i.e., including information on the direction of arrival of events on Earth. Finally, we will investigate the effect of Lorentz invariance violation on the propagation of cosmic rays from sources to the Earth by comparing its prediction with Pierre Auger data.

And finally,

- Chapter 5 will contain a summary of the findings and conclusions. In particular, we suggest reading Appendix A for the reader who is unfamiliar with celestial coordinate systems. The appendix B gives an idea of the CRPropa3 code that is used to perform the simulations of UHECRs.

Chapter 2

Cosmic Rays Physics

The purpose of the study of Ultra-High Energy Cosmic Rays (UHECRs) is the understanding of their nature and origin. This is done through an incessant search for the characterization of the sources of cosmic rays, the understanding of the mechanisms of production and the identification of their chemical composition. With this aim, the experiments detect: the direction of incidence and the spectrum of the cosmic rays, looking for correlation with point sources or anisotropies in large scale, in order to determine the spectrum and parameters that relate to its composition.

The aim of this chapter is to present the physics of cosmic rays with a main focus on the study of UHECRs. In this chapter will briefly describe the energy spectrum, basic concepts of acceleration mechanisms, the main energy loss processes for UHECRs during propagation and the distribution of arrival directions

2.1 History

Cosmic rays are defined as charged particles, mostly protons and fully ionized nuclei, coming from the outer space to the Earth atmosphere. The cosmic rays were discovered at the beginning of the twentieth century by two scientists, the Austrian Victor Hess and the Italian Domenico Pacini. Their work was essential to determine the origin of the atmospheric radiation, the "penetrating radiation" today called cosmic rays. At our day the study of the cosmic rays plays a central role in Astroparticle Physics from the experimental and theoretical point of view.

Pacini in his pioneering work compared the rate of ionisation on mountains, over a lake and over the sea, for establishing the level of the fluctuations and of the daily variations. He published the results of his measurements in 1911 in an article titled “Penetrating radiation on the sea”. Pacini concluded that a certain part of the ionisation itself must be due to sources other than the radioactivity of the Earth, thus contributing to the extra-terrestrial interpretation of the “penetrating radiation”. The measurements of Pacini were perfectly known at that time in the world and are cited by several older reviews on the cosmic rays [Wolfendale, 1984],[Wilson, 1976],[Janossy, 1950],[Hillas, 1972]. In 1912, soon after the work of Pacini, the Austrian physicist Victor Hess published the results of his experiments of the rate of ionization made aboard a balloon. Hess showed that the rate of ionization increases with height, so reaching the same conclusions of Pacini about the origin of the radiation.

Despite the conclusions of Pacini, physicists were reluctant to abandon the hypothesis of a terrestrial origin of the mystery penetrating radiation. In 1936 Hess was awarded with the Nobel Prize for the discovery of the cosmic radiation. Pacini died in 1934 and his work was largely forgotten through the combination of historical and political circumstances.

In 1926 Robert Millikan confirmed Victor Hess’s thesis in which the origin of this ionizing radiation would be out of the Earth and used for the first time the term “cosmic rays” [Kampert and Watson, 2012]. Before the construction of the colliders, the study of the cosmic rays constituted the main channel for investigating the subatomic structure of the matter.

The contribution of the french physicist Pierre Auger was highlighted, in 1938. He set up an apparatus array detectors and concluded that several particles correlated in time were being produced by a single event. Hence the atmospheric shower of secondary particles is the result of the interaction of the primary cosmic ray with the molecules of the terrestrial atmosphere [Biermann and Sigl, 2001],[Stanev, 2010], a phenomenon previously suggested by Rossi (1934). After the discovery of the atmospheric showers generated by the interaction of cosmic ray with the atmosphere provided a first way to estimate the energy of cosmic rays, many other detection techniques were developed and some observatories were constructed.

Although the cosmic rays have been discovered one hundred years ago, the origin of these particles is still unknown and the mechanisms through which they are accelerated are also unclear. The fux of cosmic rays is described by a power law, decreases as energy increases, and has three very visible changes in the spectral index: the knee a $\sim 4 \times 10^{15}$ eV, the ankle around $\sim 4 \times 10^{18}$ eV and the cutoff region above $\sim 4 \times 10^{19}$ eV. Cosmic rays with energy above $\sim 10^{18}$ eV are called ultra-high energy cosmic rays (UHECRs) and is a object of the study of this thesis.

2.2 Possible sources and mechanisms of acceleration of UHECRs

One of the great questions to be answered in relation to UHECRs is how such particles can propagate through cosmological distances and still arrive at Earth with energies of the order of 10^{18} eV.

2.2.1 Acceleration Mechanisms

The Bottom-up model try to explain the existence of UHECRs, considering that particles with lower energies can reach higher energies through processes defined by diffusive and direct accelerations, in which charged particles of the interstellar matter are accelerated to highest energies e.g. by shock waves.

The astrophysical sources can accelerate cosmic rays through two kinds of acceleration mechanisms: inductive mechanism (one shot or direct acceleration) by a very high electric field and diffusive (stochastic) mechanism based on a Fermi acceleration model in a magnetized plasma.

In direct mechanism, the particles are accelerated continuously by a large-scale electric field. The acceleration is proportional to the charge of the particle, the strength of the field, and the extent of the field. There is no known way to produce a large static electric field in an astrophysical environment (conductive plasmas will quickly neutralize the field). Therefore, direct acceleration must be accomplished with dynamic electric or magnetic fields. The major disadvantage of this type of acceleration mechanisms is the difficulty to obtain the characteristic power law spectrum of the observed cosmic rays spectrum. However, the conditions for direct acceleration might arise through the motion of a rapidly rotating magnetised conductor, such as a black hole or pulsar, which establishes a potential difference between the surface of the object and infinity, in which the particle can be accelerated.

In relation to the diffusive mechanism model, as the statistical acceleration process proposed by Fermi [Fermi, 1949] where the cosmic ray particles gain energy by random scattering off of moving "magnetic clouds".

2.2.1.1 Fermi mechanisms

The cosmic rays energy spectrum follows a well-defined functional form, which will be seen in the section 2.4. This suggests that the acceleration mechanisms produce the particles respecting this function. Thus, through the spectrum, cosmic rays are messengers of physical processes that occur in their sources, providing experimental information on the mechanisms of acceleration. Fermi proposed the acceleration mechanisms around 1950, which reproduced the spectrum as a power law. The original basis of this theory is to consider the energy gain of the particles as a result of the interaction with electric fields, induced by the movement of magnetic fields present in the clouds of gas in the interstellar medium [Protheroe, 1999].

Diffusive acceleration can be highly efficient in the vicinity of shock fronts. Each time a particle is scattered across the shock front, it will, on average have gained energy. In particular, considering a process of cyclic energy injection with a gain $\Delta E = \epsilon E$. This proportional to the own energy E of the particle, after n interactions we will have $E_n = E_0(1+\epsilon)^n$, where E_0 is the initial energy of the particle. Considering this scenario the number of cycles needed to reach E_n is $k = \frac{\ln(E/E_0)}{\ln(1+\epsilon)}$. Since P_{esc} is the probability of the cosmic ray escaping from the region of acceleration in each energy gain interaction, $(1-P_{esc})^n$ is the probability to stay in the acceleration region. The number of particles with energy greater than E will be

$$N(>E) = N_0 \sum_{m=k}^{\infty} (1 - P_{esc})^m. \tag{2.1}$$

Rewriting equation (2.1) and changing the sum indices:

$$N(>E) = N_0(1 - P_{esc})^k \sum_{m=k}^{\infty} (1 - P_{esc})^{m-k},$$

$$N(>E) = N_0(1 - P_{esc})^k \sum_{m=0}^{\infty} (1 - P_{esc})^m. \tag{2.2}$$

Equation (2.2) is known as $\sum_{m=0}^{\infty} x^m = \frac{1}{1-x}$, for $x < 1$ and thus we have

$$N(>E) = N_0 \frac{(1 - P_{esc})^m}{P_{esc}},$$

$$k = \frac{\ln(P_{esc}\frac{N(>E)}{N_o})}{\ln(1 - P_{esc})} = \frac{\ln(E/E_o)}{\ln(1+\epsilon)}.$$

Finally can be write in the form of power law:

$$\frac{N(>E)}{N_o} = \frac{1}{P_{esc}}(\frac{E}{E_o})^{-\gamma}, \tag{2.3}$$

with spectral index

$$\gamma = \frac{\ln[1/(1 - P_{esc})]}{\ln(1+\epsilon)}.$$

Therefore, it has been shown that the cyclic acceleration mechanism, where the energy gain is proportional to the particle's own energy, leads naturally to a power law type spectrum. The astrophysical aspects of the sources of the cosmic rays would appear in the parameters ϵ, related to the energy gain per cycle, and P_{esc}, that is the probability of escaping from the source. The energy gain and exhaust efficiency depend on the particle type in question as well as the parameter ϵ and P_{esc}.

The acceleration mechanisms must have a limiting energy from which the production of particles is suppressed. This should essentially occur because the source can not keep the particle in the region of acceleration above a certain energy that is controlled by P_{esc}. It is important to note that this phenomenon has an impact on the energy spectrum since it will present a suppression for above a given energy $E > E_{max}$. Then, from astrophysical processes, Fermi showed energy injection mechanisms that reproduce the power law spectrum, which are called first and second order Fermi mechanisms.

The second order mechanism considers a gas cloud magnetized as the accelerator of these particles. The cosmic rays would then be accelerated after entering into one of these clouds and would suffer multiple random scatters. The average energy gain rate, ΔE, divided by the initial energy of the pre-collision particle, E, for ultra-relativistic particles can be expressed by:

$$\frac{\langle \Delta E \rangle}{E} \approx \frac{4}{3}\beta^2, \tag{2.4}$$

where β represents the velocity of the cosmic ray in unity of the speed of light in the vacuum. Because the energy gain rate depends on β^2, this mechanism is known as second order Fermi acceleration.

However, another more efficient version of the Fermi acceleration mechanism considers that shock waves produced by astrophysical objects are capable of accelerating cosmic rays so that the average rate of energy gain depends on the relative velocity in the first order, that is

$$\frac{\langle \Delta E \rangle}{E} \approx \frac{4}{3}\beta. \tag{2.5}$$

This process is known as first order Fermi acceleration, or diffusive shock acceleration mechanism [Axford et al., 1977],[Protheroe, 1999].

Shock waves are quite frequent in the universe, being able to generate a differential energy spectrum equal to $dN(E)/dE \propto E^{-\gamma}$, where $\gamma \approx 2.2$ is called spectral index [Achterberg et al., 2001]. When applied to shocks in Supernova remnants (SNR), which are believed to be the sites where galactic cosmic rays are accelerated via the first-order Fermi acceleration mechanism, it can generate particles up to a maximum energy of $\approx 10^{17}$ eV [Biermann, 1994]. Popular shock regions for UHECR acceleration are Gamma-ray Bursts (GRB) shocks, jets and hot spots of Active Galactic Nuclei (AGN), and gravitational accretion shocks.

Several studies [Lemoine and Pelletier, 2003],[Pelletier et al., 2009] argued that this is a rather complex process and the simplified assumptions commonly used may induce an overestimation of the efficiency of the process. For instance, in [Lemoine et al., 2006] it is suggested that Fermi acceleration at relativistic shock waves can not occur if the Larmor radius of the accelerated particle is much smaller than the typical coherence length of the magnetic field in the cloud. Moreover, in realistic scenarios, the cosmic ray can gain energy as in the first order Fermi mechanism only the first time it crosses the stream, and subsequently it behaves as a second order process, because the time available to isotropize the distribution of cosmic rays after it crosses the shock for the first time is not enough [Gallant and Achterberg, 1999].

However the most common versions of the Fermi acceleration face many problems. Some alternative models of diffusive shock acceleration inspired by the first-order Fermi mechanism predict that similar mechanisms can accelerate particles up to $E \approx 10^{18}$ eV, such as those presented in [Gialis and Pelletier, 2004],[Globus et al., 2015].

2.2.1.2 Other acceleration mechanisms

Among the different models proposed, one could consider acceleration of magnetic reconnection due to the magnetic fields in opposite directions, plasma wakefield acceleration (related to ponderomotive acceleration) and re-acceleration in sheared jets. In a plasma, a local reconfiguration of the magnetic field topology (reconnection) occurs when the plasma conductivity is not high enough to support the current associated with a magnetic field structure [Zweibel and Yamada, 2009]. The field reaches a lower energy level configuration, and the liberated energy can be devoted to particle acceleration. This mechanism, responsible for the generation of high energy particles in the solar flares, has been applied to the acceleration of the UHECR in the pulsar winds [Kirk et al., 2002], in gamma rays burst [Thompson, 2006]. The first-order Fermi acceleration could feed this mechanism, since the particles reflected in the magnetized plasma could converge in the reconnection region [de Gouveia Dal Pino and Kowal, 2015]. More details about these mechanisms can be found in [Blasi, 2013].

Plasma wakefield acceleration, a wake-field is created in a plasma when waves with high charge separation (electrons and ions) travel through the plasma. It leads to the formation of ponderomotive forces[1] that can accelerate particles if they are trapped in the wave [Chen et al., 2002].

2.2.1.3 Possible acceleration sites

Direct acceleration, would be the result of interaction between cosmic rays and astrophysical objects capable of generating magnetic fields of high intensity, like pulsars and black holes. It is also possible to correlate the intensity of the magnetic field generated by such objects with the acceleration capacity of the cosmic rays.

Considering an energy scale above 100 TeV, the Fermi mechanisms are not sufficient for cosmic rays to reach high energy. Astrophysical processes with higher energy release are needed to generate the UHECR. M. Hillas [Hillas, 1984] proposed in 1984 that the maximum energy that a cosmic ray could obtain from an astrophysical source is limited to the combination of the size and intensity of the magnetic field of the acceleration region, which can be expressed as follows

$$E_{max} = \beta ZeBR \;\approx\; \beta\Big(\frac{B}{\mu G}\Big)\Big(\frac{R}{kpc}\Big)10^{18}eV, \tag{2.6}$$

where $\beta = $ v/c, is the ratio between the speed of the particle (the velocity of transport of the magnetic field) and the speed of light, Ze is the charge of a nucleus, B is the intensity of the magnetic field, and R is the size of the acceleration region.

[1]ponderomotive force is a nonlinear force that a charged particle experiences in an inhomogeneous oscillating electromagnetic field

Such correlation has a representation called the "Hillas Diagram", where candidate sources are placed in a $B - R$ phase-space, which classifies some candidates for cosmic ray sources/accelerators according to their dimensions and intensity of the magnetic field produced. This relation can be seen in figure 2.1.

In the figure, above the blue and red lines, the possible sources that could confine protons and iron nuclei with energies superior to 10^{20} eV are represented respectively. The region occupied by each source indicates the uncertainty in its parameters (source size and intensity of the magnetic field produced). One can highlight potential sources of UHECRs leaving the best candidates for UHECR acceleration to be: neutron stars, Active Galactic Nuclei (AGN), Gamma-Ray Bursts (GRBs).

Neutron stars: are highly magnetized astrophysical objects capable of producing magnetic fields of the order of $\sim 10^{13}$ G (pulsars) or 10^{15} G (magnetars). These present a strong rotation movement capable of generating electric fields, by the variation of the magnetic field, to the point of producing UHECRs. This type of acceleration mechanism is capable of producing cosmic rays with a maximum energy of $\sim 10^{21}$ eV [Blasi, 2013].

Active Galactic Nuclei (AGNs): these are galaxies that host tremendously large black holes in their centers that feed on gas and stars and can eject plasma for the intergalactic space. Among the classifications of Active Galactic Nuclei, blazars and quasars are the largest candidates for UHECRs sources since they have jets oriented to directions close to Earth. A correlation between the positions of AGNs and the directions of arrival of cosmic rays above 57 EeV was observed by the Pierre Auger Collaboration in 2007 [Abraham et al., 2007]. However, with the increase in the statistics of events in this energy range, this correlation has decreased considerably, as will be treated in more detail in Section 2.8.1.

Gamma-Ray Burst (GRBs): are the result of hypernova (supernova) explosions or collisions between binary neutron stars. They are capable of generating shock waves that produce particles accelerated by the first order Fermi mechanism. A possible correlation between these explosions and the UHECR flux was suggested after the detection of two ultra-energy cosmic rays with reconstructed arrival directions that coincided with two of the most powerful explosions of Gamma-Ray Burst detected. The two events had energy of $\sim 10^{20}$ eV and were detected by the Fly's Eye experiments in 1991 and AGASA in 1993 [Milgrom and Usov, 1995].

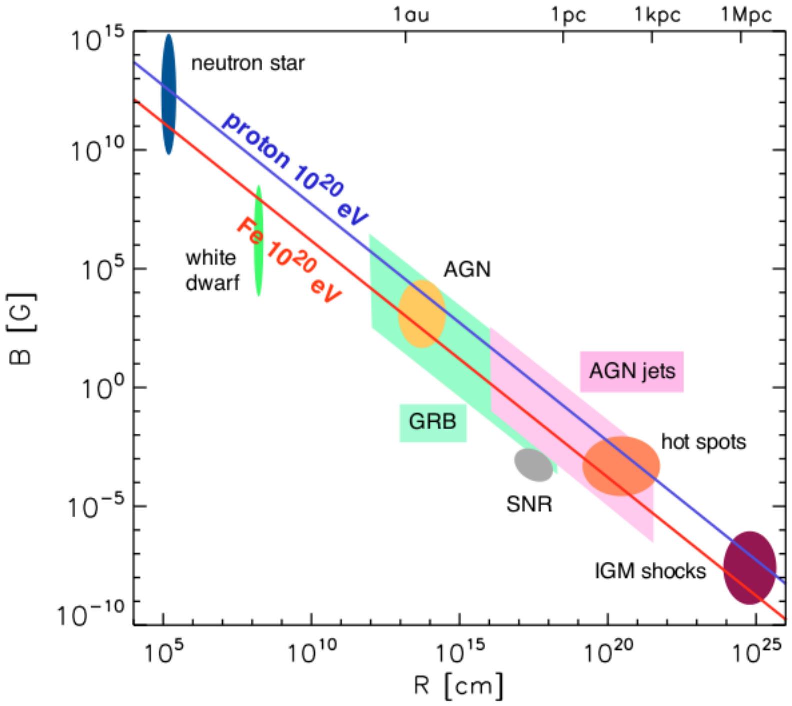

FIGURE 2.1: Hillas diagram, intensity of the magnetic field in relation to the size of several sources of acceleration of the cosmic rays, the candidate sources to produce UHECRs are shown with the uncertainties in their parameters. In this figure are Active Galactic Nuclei (AGN), Gamma Ray Burst (GRB), Intergalactic Medium (IGM) and Supernova remnant (SNR). Besides that, White dwarfs and so-called hotspots are also cited. [Blaksley, 2014].

2.2.2 Non-acceleration Mechanism

Other models of particle physics beyond the Standard Model have also been proposed for the origin of UHECRs. Top-down model predict by decay processes from topological defects as magnetic monopoles, cosmic strings and relics of the early universe [Pierre Auger Collaboration et al., 2009] the existence of the highest energy cosmic rays. Another Top-down theory claims that UHECRs originate from weakly interacting super-massive particles ("wimpzillas") [Kolb et al., 1999].

While Top-down models can explain the existence of UHECRs, they require a high fraction of photons (there would also be a significant fraction of neutrinos) in the flux of UHECRs after the decay of these exotic particles [Bhattacharjee and Sigl, 2000]. Thus, the parameters of these theories can be bound by measuring the limit in the flux of photons and neutrinos. Since these supermassive particles would tend to accumulate in the halo of galaxies, the origin of the cosmic rays should be galactic. These models were consistent with the results presented by the AGASA experiment [Chiba et al., 1992], which observed an excess of events towards the center of our galaxy but the most recent published cosmic ray spectra measured by the HiRes, Auger and Telescope Array experiments measure a cutoff in the CR spectrum which are firm predictions of top-down models, strongly constrain these models.

2.3 Propagation of cosmic rays

After leaving the sources with an initial energy E_i, the UHECRs begin to propagate in the extragalatic and galactic medium, and can reach the Earth with energy E_f and in a different direction from the original. The propagation changes the original conditions in which the cosmic rays were created.

During its propagation, cosmic rays can suffer energy losses processes through cosmological expansion and from the interactions with Cosmic Microwave Background (CMB) [Smoot and Scott, 1996] and Extragalactic Background Light (EBL) [Dwek and Krennrich, 2013]. The CMB is a field of photons that permeates the entire universe, in the range of the microwave, considered a relic of dissociation of matter after the Big Bang, being described by a spectrum of black body temperature of 2.7 K. On the other hand, the EBL is part of the diffuse extragalactic background radiation, which covers the overall electromagnetic radiation wide range of frequencies, with Cosmic Infrared Background (CIB) [Hauser and Dwek, 2001] being its most expressive component in relation to the propagation of ultra-high energy particles.

Furthermore, charged particles suffer deflection in their trajectories due to interactions with the extragalactic and galactic magnetic fields during their propagation. For protons the most important energy losses in the interaction on the CMB are the pion production and electron-positron pair production. These mechanisms of energy loss resulting from the propagation of cosmic rays will be described in the following.

2.3.1 Pair production e^+e^-

Considering that a proton interacts with the CMB photons. This takes place as the process of pair production (known as the Bethe-Heitler process) according to the reaction:

$$p + \gamma_{CMB} \rightarrow p + e^+ + e^-. \tag{2.7}$$

The threshold for the this reaction is $\sim 4.8 \times 10^{17}$ eV. The mean free path is about 1 Gpc and the attenuation length tends to become constant and equal to the energy loss due to the expansion of the universe ~ 4 Gpc.

2.3.2 Pion photo-production

At the ultra-high energy end of the cosmic ray spectrum, protons are above the threshold for the production of pions, the lightest mesons, upon collision with CMB photons. The production occurs in two channels through resonance $\Delta(1232\ MeV)$,

$$p + \gamma_{CMB} \rightarrow \Delta^+ \rightarrow \begin{cases} p + \pi_0 \\ n + \pi_+. \end{cases} \tag{2.8}$$

The energy threshold is about 10^{20} eV and the mean free path for a proton of about 10^{20} can be estimated as ~ 8 Mpc. Above E ~ 60 EeV, the distance that particles can travel without losing their energy shortens considerably.

2.3.3 GZK effect

After the discovery of the CMB [Smoot, 2007],[Durrer, 2015] it was proposed that ultra-high energy cosmic rays should interact with the photons, leading to a suppression of the observed flux at highest energies.

Its impact on cosmic ray physics had already been predicted in 1966 by Greisen [Greisen, 1966], Zatsepin and Kuzmin (GZK) [Zatsepin and Kuzmin, 1966]. The other point to be observed is that the GZK effect limits the possible universe to the origin of cosmic rays that reach the Earth with energy $E > 60$ EeV. On average, about 17% of the energy of the cosmic ray is lost in each interaction. Thus, above the minimum energy of pion photo-production, the flux of protons coming from a distance greater than GZK should be greatly suppressed [Abbasi et al., 2008],[Harari et al., 2014]. Therefore these cosmic rays can not originate very far from the Earth, (100 Mpc of us) otherwise, they would lose a lot of energy in the propagation and would not reach Earth with energy above E. In the figure 2.2 the attenuation lengths related to these processes are shown. Through the attenuation length it is clear that at high energy the impact of pions photoproduction is dominant. The action of the GZK effect on the propagation of cosmic rays is illustrated in figure 2.3, which shows a simulation of the propagation of a proton with initial energy of 10^{20}, 10^{21} and 10^{22} eV. The higher the energy of the cosmic ray, more intense the mechanism of energy loss in pion photo-production.

The curves represent the energy of the proton, changed in different order of magnitude in energy. After propagating for a distance up to 120 Mpc, cosmic rays has essentially energy around 40 EeV.

Another way to represent the impact of the GZK effect is to show the probability $\omega_{GZK}(E_{th}, D)$ of a cosmic ray arriving at Earth with energy E above a threshold E_{th} after propagating distance D. Figure 2.4 shows the fraction of cosmic rays arrive at Earth, for different energies and nuclei coming from sources whose distances are greater than D. Through these curves we define the GZK horizon, the distance R_{GZK} for which 90% of the cosmic rays are originate at a distance $D < R_{GZK}$, that

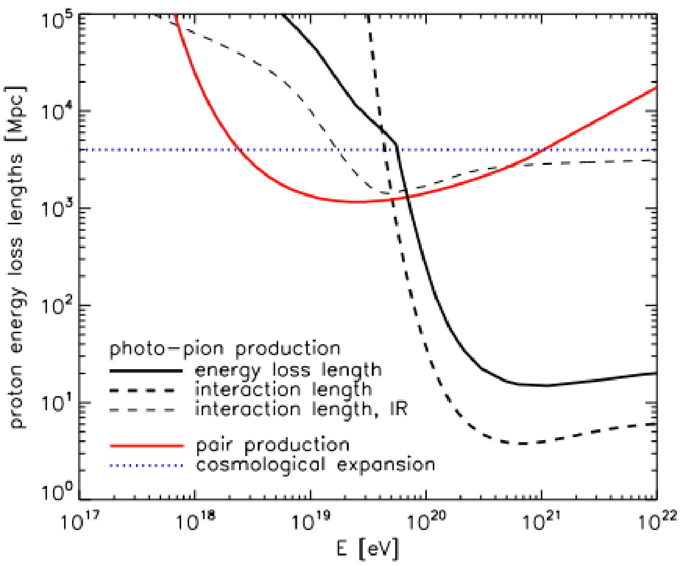

FIGURE 2.2: Energy loss length of protons as a function of their energy for different interaction processes. Black solid line corresponds to photo-pion production on CMB and IR-UV photons; red solid line for pair production on CMB photons. Dashed lines represent the interaction length (or mean free path to interaction) for photo-pion production. The dotted line indicates the losses due to cosmological expansion.[Kotera and Olinto, 2011].

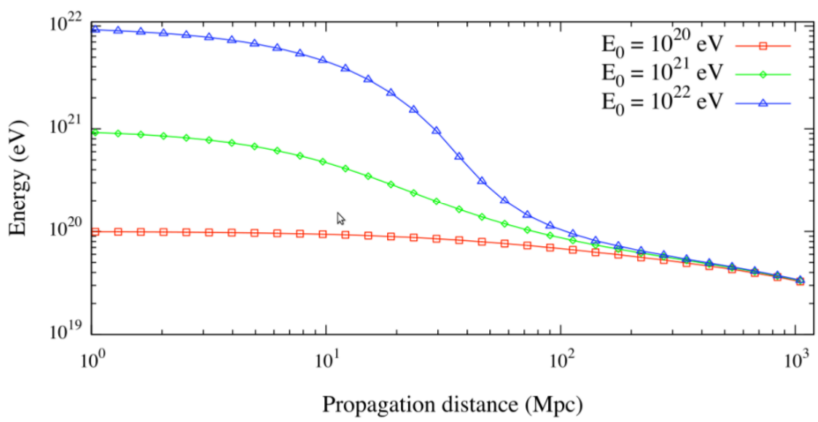

FIGURE 2.3: The energy of protons as a function of the propagation distance. As a consequence of the GZK effect, protons coming from a distance greater than ∼100 Mpc have lost memory of their initial energy of 10^{20}, 10^{21} and 10^{22} eV.[Boratav et al., 1992].

contribute to the flux of UHECRs on Earth. It is clear that only the 10% of cosmic rays, in this case for protons with energy above $E = 6 \times 10^{19}$ eV are originate at distance $D > 200$ Mpc from the Earth.

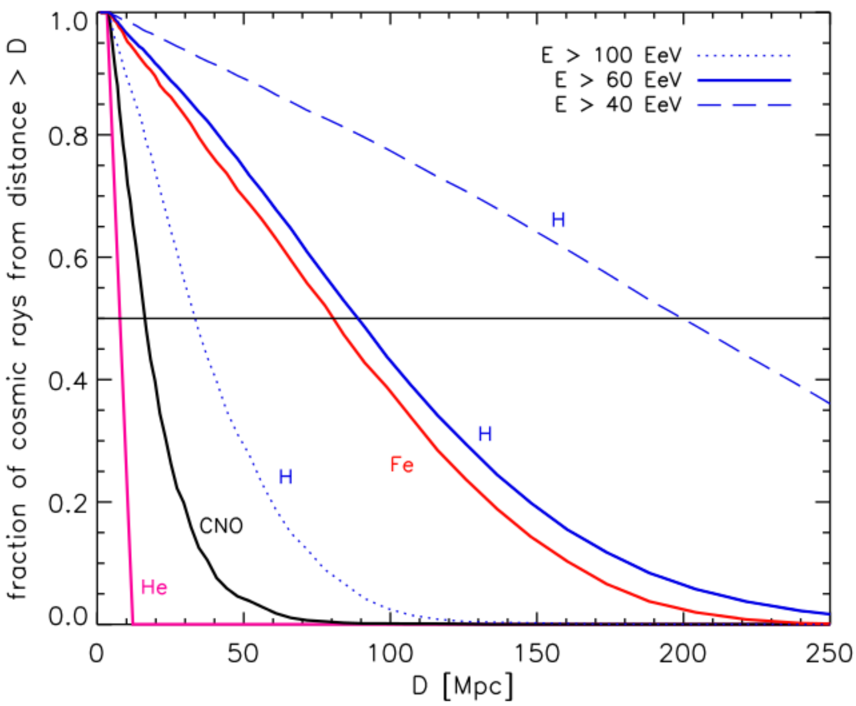

FIGURE 2.4: Fraction of cosmic rays arriving at Earth, for different energies and nuclei coming from sources whose distances are greater than D, for protons above 40, 60, and 100 EeV and for He, CNO, and Fe above 60 EeV. [Boratav et al., 1992].

2.3.4 Photodisintegration of nuclei

When we consider cosmic rays as a heavy nucleus type A, the interaction with CMB can be given by

$$A + \gamma_{CMB} \rightarrow (A-1) + N. \tag{2.9}$$

In this reaction, the photon γ_{CMB} excites the states of the heavy nucleus A giving rise to the phenomenon of giant nuclear resonance. The nucleus enters a state of resonance and breaks releasing nucleons N.

This process happens for energies comparable to the threshold 60 EeV of pion photo-production. As the loss of energy is very large, this reaction will also give rise to a suppression in flux particles.

2.3.5 Adiabatic energy loss

Simple expansion causes adiabatic energy loss. In this process, the cosmological parameters that define the evolution of the universe are central to determining the loss of energy. Adiabatic expansion of the universe is capable of causing loss of energy during the propagation of the particles. This energy loss is given by

$$E = \frac{E_0}{1+z}, \tag{2.10}$$

where E_0 represents the initial energy of the particle and z its redshift [Stanev et al., 2000], [Alves Batista, 2015].

2.3.6 Magnetic Deflection

Since the majority of cosmic rays are charged particles, they are deflected by the galactic (GMF) and the extragalactic (EGMF) magnetic fields while travelling through outer space. The radius of curvature of a relativistic charged particle in a uniform magnetic field (the Larmor radius) is

$$R_L \approx \; (1kpc)\frac{1}{Z}\frac{E/EeV}{B/\mu G}, \tag{2.11}$$

with E the energy of the particle, Z its number of charge carriers and B the magnetic field strength; $1pc = 3.086 \times 10^{16}$ m.[2] From that equation, we can see that the

[2] A parsec (pc) is a unit of length used to measure large distances to objects outside our Solar System.

deflections decrease with increasing magnetic rigidity[3] (E/Z). From the Larmor radius, we can obtain an angular scale of deflection for the cosmic rays in some propagation regimes controlled by rigidity. The cosmic ray trajectories in galactic and extragalactic magnetic fields become straighter as the energy increases, being for instance the typical deflection for a nucleus of charge Z traveling a distance L in the galactic field of

$$\delta^\circ = 3^\circ \left(\frac{60\ EeV}{E}\right)^{-1} \left(\frac{L}{kpc}\right)^{1/2} \left(\frac{B}{\mu G}\right) \tag{2.12}$$

Protons of energies around $E \approx 5 \times 10^{19}$ eV will be deflected by a few degrees or less and will suffer loss of energy by producing Δ-resonances with CMB photons. If one excludes certain regions of the galaxy, the average deflection is about 2°.

Magnetic fields are capable of generating an angular variation in the polarization of observed radiation, an effect known as Faraday's rotation [Pshirkov et al., 2011]. From measurements of Faraday's rotation it is possible to infer the intensity of the galactic magnetic fields and extragalactic magnetic fields between $\sim 2\ \mu$G and $\sim$ 1-40 nG respectively [Stanev, 2010],[Kotera and Olinto, 2011]. In this thesis we just considered the deflections in the GMF, we use the JF12 model (see Section 2.3.7) because is one of the most up to date.

2.3.7 The Jansson-Farrar model for the galactic magnetic field (GMF)

As already mentioned, the charged particles suffer deflections in their travel through the galaxy caused by the magnetic field. One of the most commonly used models for the GMF abbreviated as JF12, for having been proposed by Jansson and Farrar [Jansson and Farrar, 2012a], [Jansson and Farrar, 2012b]. It is the result of fit of the Galactic synchrotron emission map and more than 40 000 extragalactic rotation

[3]The magnetic rigidity is defined as $R = \frac{Pc}{Ze}$, where P is the total momentum of the nucleus, c is the speed of light and Ze is its electric charge. As particles with the same rigidity and injection direction exhibit identical trajectories in a given magnetic field configuration, this magnitude is appropriate to describe changes in the spectrum due to propagation and acceleration in magnetic fields.

measures to constrain its parameters. It is composed by three components: regular, turbulent and striated [Alves Batista, 2015]. A representation of the regular, turbulent, striated components of the JF12 model for the galactic magnetic field is shown in Figure 2.5. The total field, obtained from the three components, is shown below right in the same figure.

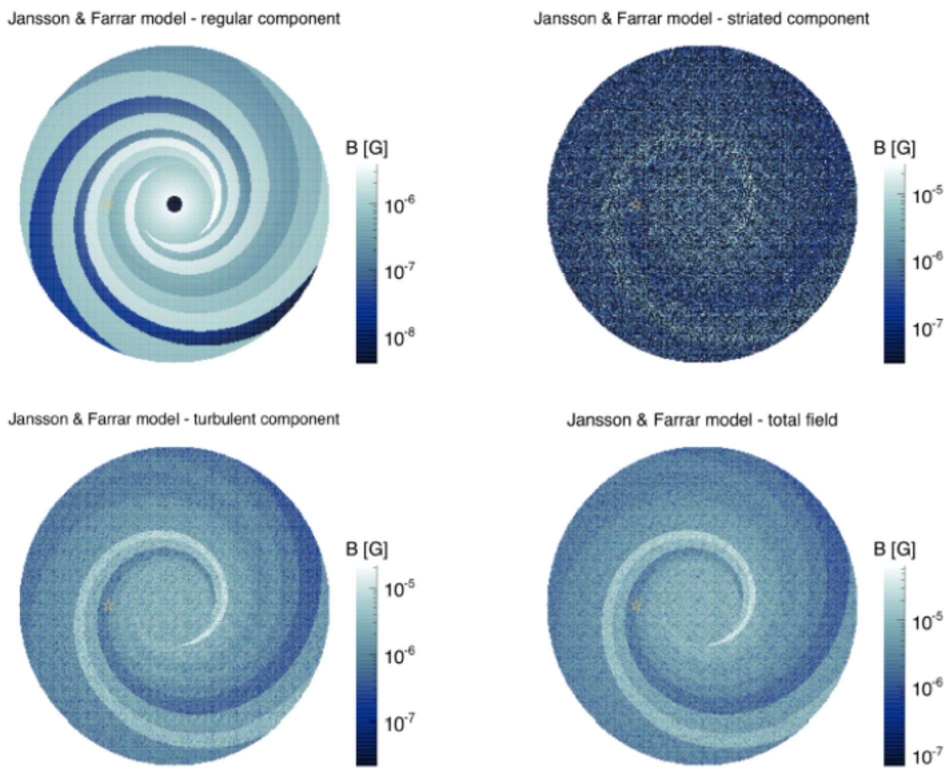

FIGURE 2.5: Regular (top left), striated (top right), turbulent (bottom left) and total (bottom right) components of the JF12 GMF model [Alves Batista, 2015].

Currently, Monte Carlo-based codes, such as CRPropa3 [Alves Batista et al., 2016] and SimProp [Aloisio et al., 2012], reconstruct the propagation of UHECRs in the universe considering their interaction with magnetized environments and the processes of energy loss. We will use the CRPropa3 code in the analysis described in chapter 4.

2.4 Energy spectrum

The cosmic ray spectrum i.e. the variation of the cosmic ray flux (number of particles per unit area per solid angle per unit time) with energy spans several orders of magnitude. Figure 2.6 shows a compilation of the measured spectrum, with data collection from several experiments, illustrating the wide range of energy and flux already investigated over decades with the involvement of several direct and indirect detection techniques, appropriate to each range of energy.

For very high energies, there are larger uncertainties in the spectrum since the flux of particles is reduced. The cosmic rays have been detected directly and indirectly, depending on the flux. It becomes possible for a direct detection when it goes to energies of 10^{15}; through instruments such as balls or satellites. For higher energies it is necessary the detectors with a very large area in agreement with the flux. Through air showers it is possible to make indirect measures to investigate higher energy ranges.

The cosmic ray flux is described as the particles flux N depending on the energy E. The differential expression commonly used as an approximation for several orders of magnitude is the following power law:

$$\frac{dN}{dE} \propto E^{-\gamma}, \tag{2.13}$$

where γ is called the spectral index. In figure 2.6 differential energy spectrum has been multiplied by $E^{2.6}$ in order to display the features of the steep spectrum that are otherwise difficult to discern. The flux of cosmic rays is described by a broken power law with few but apparent changes of the spectral index, see figure 2.6 taken from [J. J. Beatty and Wakely, 2015].

In the region of lower energies the spectrum is described by the function with γ equals 2.7. However, three structures stand out. The first one is characterized by the index change around E $\approx 4 \times 10^{15}$ eV, in this region the gamma spectral index γ goes from 2.7 to 3.1. This point is known as the “knee” or “first knee” of the spectrum and particles flux falls faster. Its interpretation is still debated

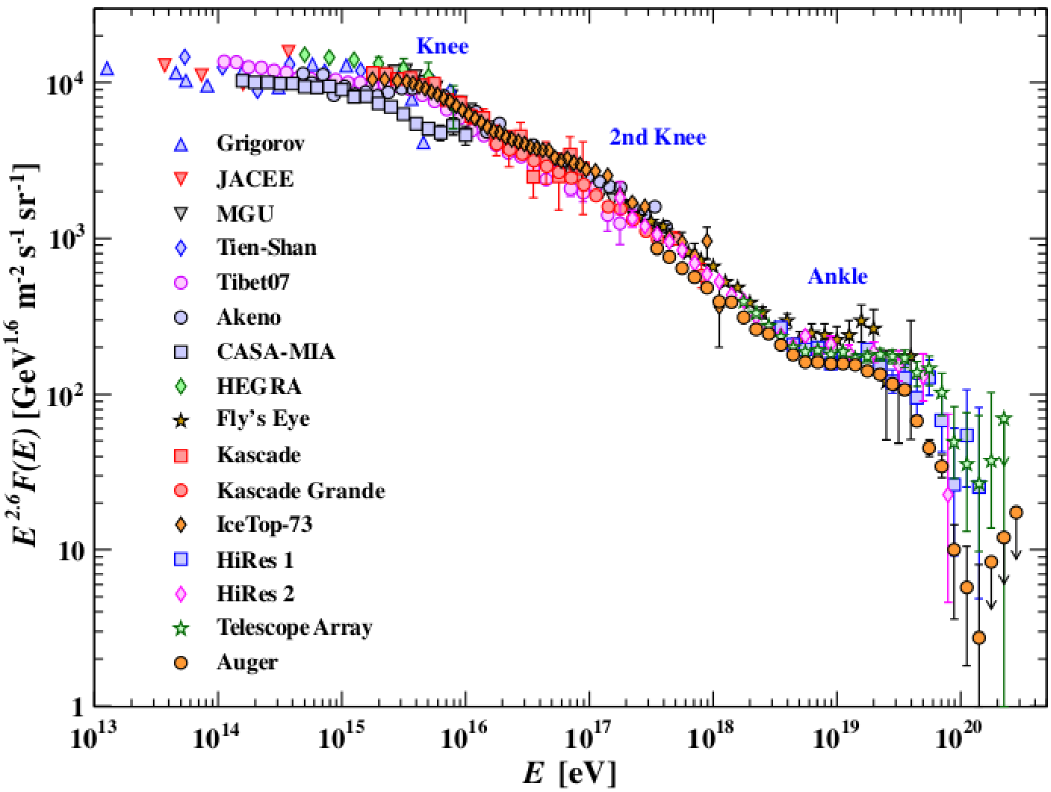

FIGURE 2.6: The all-particle spectrum as a function of E (energy-per-nucleus) from air shower measurements [J. J. Beatty and Wakely, 2015].

[Hoerandel, 2003]. There is another feature in the cosmic ray energy spectrum at $\sim 4\times10^{17}$ eV, called "the second knee" where the spectral index becomes 3.3. Although many questions are still open with respect to changes in particles flux, possible explanations have been presented. One of them is, described by Martirosov et al. [Martirosov, 2011], affirms that the "first knee" would consist of the contribution of a single source located near the Earth. However, the predicted cosmic ray anisotropy contradicts the experimental data considering this hypothesis from a single point source [Sveshnikova et al., 2013].

Now, another explanation of the "first knee" is based on the possible contribution of a specific group of supernova remnants [Sveshnikova et al., 2013][Knurenko et al., 2016]. For the "second knee" the possible explanation is a transition from the cosmic rays of the galaxy to the extragalactic cosmic rays [Knurenko et al., 2016]. This explanation uses the concept of magnetic rigidity because the maximum acceleration suffered by the particle is proportional to the charge of the particle.

Another change occurs in the energy range above 1 EeV (1EeV = 10^{18} eV), the Pierre Auger Collaboration confirmed two other changes in the spectral index, where a third change occurs in the energy for $E_{ankle} = (4.8 \pm 0.1 \pm 0.4) \times 10^{18}$ eV, there is a change in the γ from ~ 3.3 to ~ 2.6 this transition is known as "Ankle" of the spectrum. This region could be explained by the so-called "Dip Model". In this model, the particles, considered protons, would suffer degradation of their energy by the production electron-positron pair resulting from the interaction with the cosmic background radiation as they propagate through cosmological distances [Berezinsky et al., 2005]. The other model so-called "ankle model", based on the interpretation of the ankle as spectrum feature of the transition between galactic and extragalactic at the ankle [Hillas, 2006].

The last change is the suppression of the spectrum can be understood by two different scenario, that is $E_s = (42.1 \pm 1.7 \pm 7.6) \times 10^{18}$ eV the spectrum presents a suppression of the flux changing the spectral index from 2.7 to 4.2 [Abraham et al., 2008]. In this region, the dominant process would be the result of the loss of energy by photoproduction of pions, due to the interaction of the proton with the CMB, which would result in the rapid loss of energy of the proton. This change is consistent with the Greisen, Zatsepin and Kuzmin (GZK) effect.

However, considering energies as high as 60 EeV, it is possible that the sources may not have power to accelerate particles which also leads to a large suppression of the flux. The presence of suppression in this energy range is well established but its interpretation is still open and needs to be confirmed [Abraham et al., 2008]. Figure 2.7 shows the flux of UHECRs measured by the Auger Observatory in these energy ranges.

Within the systematic uncertainties, the energy spectrum measured by the Pierre Auger Collaboration is compatible with the measurements performed by the Telescope Array (TA) [Tinyakov, 2014] and HiRes [Abbasi et al., 2008].

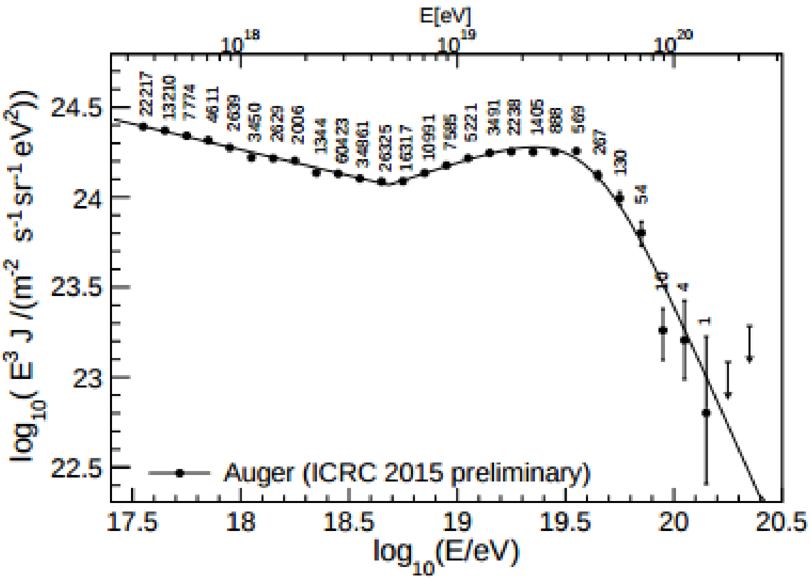

FIGURE 2.7: Combined energy spectrum, adjusted to a theoretical flux. The number of events is displayed above the points that are positioned at the mean values of log_{10}(E/eV). [Valino, 2016][Aab et al., 2015f].

2.5 Interaction with the atmosphere

The primary cosmic ray with energy above 10^{15} eV interacts with the nuclei of the atmosphere and produce a flux of secondary particles that form a cascade called the extensive atmospheric shower (EAS). An important parameter is the atmospheric depth (X), defined as the mass of air per unit area, which passed a particle through the atmosphere from infinity to the position along the path describing the motion

The secondary particles are generated in the process of scattering the primary cosmic ray with the molecules present in the air and subsequent collisions. These cascades provide information about the characteristics of the primary cosmic ray, either by detailed analysis of the longitudinal development in the atmosphere or by lateral distribution of the secondary particles. The development of the shower over the atmosphere is a complex process described by the physics of the particles.

Extensive air showers develop in a complex way, being in principle a combination of three main components. An electromagnetic component (photons, electrons, positrons), the hadronic portion (proton, neutron, pion and kaon) and the muonic part (muons) as shown in Figure 2.8. An excellent qualitative prediction of the

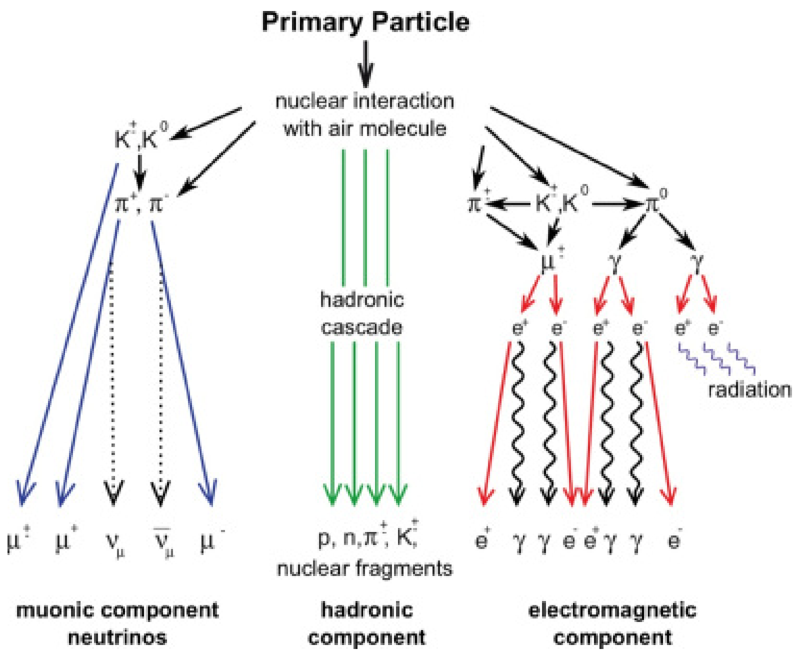

FIGURE 2.8: Representation of EAS components, showing their electromagnetic, hadronic and muonic components [Haungs et al., 2015].

characteristics of the atmospheric shower can be obtained using the Heitler model, originally developed for electromagnetic cascades and later modified for hadronic cascades [Matthews, 2005] According to this model, electromagnetic showers, initiated by photons or electrons with energy E_0, produce a cascade of secondary particles. Photons create electrons and positrons through the pairs production and electrons emit photons via emission *Bremsstrahlung*. If we consider that a photon produces a pair $e^+ \ e^-$, for each interaction n, the number of particles produced will be $N = 2^n$, with the energy of each particle given by $E = E_0/N$. The development of the shower continues until the energy of the particles produced is less than the critical E_c needed to form new pairs energy. At this point, the evolution of the shower reaches a maximum number of particles given by $N_{max} = E_0/E_c = 2^n = e^{n \ln 2}$. Although it is simplified, the Heitler model correctly reproduces an important property of the shower: the evolution of X_{max} where is the depth in the atmosphere in which the number of particles produced reaches a maximum value is given by $X^{\gamma}_{max} = X_0 + n\lambda_r \ln 2 = X_0 + \lambda_r \ln\left(\frac{E_0}{E_c}\right)$.

The Heitler model can be improved according to [Matthews, 2005], an extension of the Heitler model for hadronic showers. In this sophisticated model the calculations are similar to those presented by Heitler and the results are preserved. Shower simulations are also tools that show the relationship between $Xmax$ and energy obtained by Heitler. Currently, we know that showers carry information about the composition of cosmic rays and particle physics, which motivates the increasingly accurate measurement of this phenomenon.

2.6 Mass composition

Below 10^{14} eV, the elemental abundance in the cosmic ray flux can be directly measured using detectors above the atmosphere (see, e.g., [Ahn et al., 2010]). Since the detection of UHECRs is done indirectly, the composition of the primary particle is not directly accessible due to the decrease in flux with increased energy. It is necessary to use indirect methods of detection. Ground based experiments can give a statement about the mass of the primary cosmic ray particle by measuring the secondary particles and estimating the altitude of first interaction. This makes the identification of the primary cosmic ray dependent on models of interaction of the particles with the atmosphere, making research on composition even more complicated.

Heavy nuclei are supposed to interact higher in the atmosphere than light particles. Then the analysis of the depth of production of muons in the atmospheric shower and the depth at which the number of secondary particles is the maximum (X_{max}) is connected to the depth of the first interaction and, therefore, to primary particle mass. Frequently, the point of the first interaction is not accessible with the detector. Nevertheless, with a detector capable of measuring the longitudinal development of the particle cascade it is possible to determine the shower maximum, X_{max}, given in (g/cm^{-2}) the depth at which the number of secondary particles is largest.

The mean value of the maximum shower depth, $\langle X_{max} \rangle$, and measures of the fluctuation of X_{max}, $\sigma(X_{max})$[4], are shown in Figure 2.9, together with the theoretical prediction of models, considering proton and iron as the primary particle. The

[4] σ is the standard deviation.

measurements are compared with values obtained from air shower simulations various models of hadronic interaction at higher energies. We can see in Figure 2.9, the comparison of X_{max} and $\sigma(X_{max})$ with the hadronic interaction models such as EPOS-LHC [Pierog et al., 2015], Sibyll2.1 [Ahn et al., 2009] and QGSJetII-04 [Ostapchenko, 2014]. It shows that the composition of the primary particle tends to be predominantly lighter from 10^{18} eV to $\sim 3 \times 10^{18}$ eV and a possible transition to heavier elements would be observed at higher energies (above the ankle). This interpretation is supported by the behavior of the variance of X_{max} in the same energy region [Aab et al., 2014b].

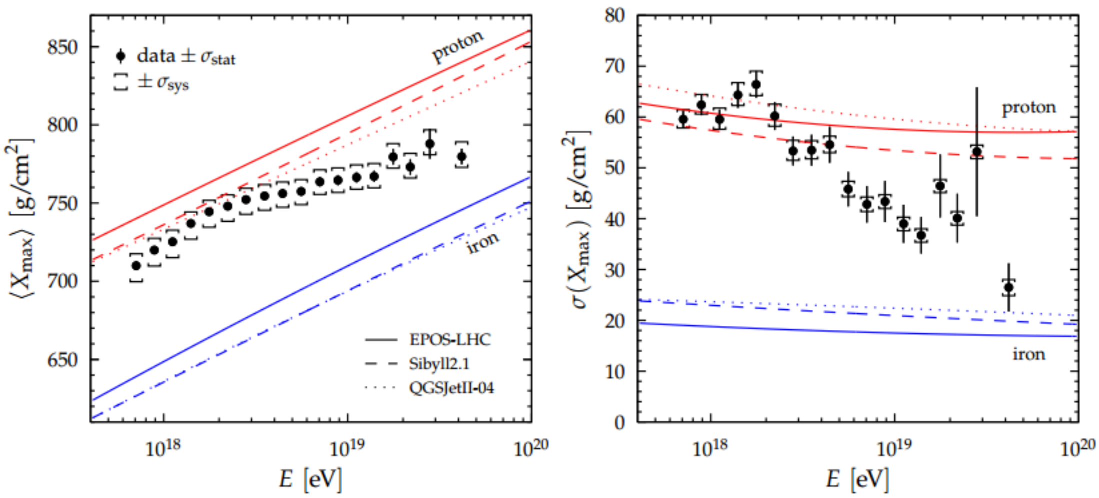

FIGURE 2.9: X_{max} and $\sigma(X_{max})$ as a function of energy. **Left:** values of the averages of X_{max} as a function of energy. Also shown are the predictions of the models EPOS-LHC, Sibyll2.1 and QGSJetII-04. **Right:** The fluctuations of the X_{max} measurements. In both figures, the last point represents the value corresponding to all events with energy $E > 3 \times 10^{19}$ eV. [Aab et al., 2014b].

The actual composition of these particles can not be inferred because it depends on comparisons with models. Considering the extrapolations for high energies, made in the hadronic models, it is concluded that at lower energies the composition is dominated by protons. With increased energy mixed compositions may appear and the behavior of the curve goes to heavy nuclei such as Fe.

However, it is important to emphasize that these conclusions depend on the validity of the hadronic interaction models, calibrated for typical particle accelerator energies, that is, some orders of magnitude below the energy of the cosmic rays measured by Pierre Auger Collaboration.

2.7 Neutrinos and photons

The search for photons and neutrinos is important to constraint the models related to the origin of cosmic rays and clarify if the observed suppression is due to the interaction with the cosmic microwave background.

Due to the fact that the neutrinos interaction cross section is extremely small, atmospheric showers can be induced by their interaction with the Earth's crust, for neutrinos with a zenith angle between 90°$< \theta <$95°, or by interaction with the atmosphere, for particles with a zenith angle between 60°$< \theta <$90° [Aab et al., 2015a].

Different types of inclined showers which can be detected by the Pierre Auger Observatory are shown in Figure 2.10.

In this figure, a regular inclined shower produced by a proton interacting in the top of the atmosphere, a much more inclined shower induced by a neutrino that travels a long distance penetrating the atmosphere, DGν (downward-going) and a neutrino τ, ν_τ, interacting with the Earth's crust, ESν_τ (Earth-skimming). This produces a lepton τ which, when decaying, induces a shower that travel in a slightly upward direction with respect to ground. Also, another tau neutrino, ν_τ, is shown, which, when interacting with the mountains (DGν_τ), produces a tau lepton τ that, when it also decays and initiating a shower very close to the SD.

On the other hand, showers induced by photons of ultra-high energy, are characterized by low muonic content and high average values of atmospheric depth of maximum shower, X_{max}, when compared with showers initiated by the same energy nuclei [Aab et al., 2014a].

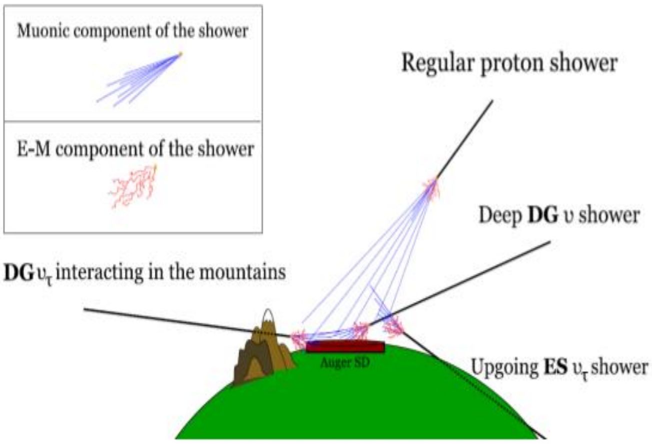

FIGURE 2.10: Representation of different types of inclined showers that can be detected by SD network of the Pierre Auger Observatory. A regular inclined shower induced by a proton, a shower induced by a DGν neutrino (downward-going) and two showers produced by neutrinos τ: ESν_τ (Earth-skimming) and DGν_τ, interacting with the Earth's crust and mountains,respectively.
[Aab et al., 2013].

The upper limits of photon fluxes and ultra-high energy neutrinos, established by the Pierre Auger Observatory, have helped discard some models of UHECR sources. Models such as the Top-down, as described in Subsection 2.2.2, are based on the idea that highly energetic cosmic rays could be the result of the decay of other supermassive particles and, therefore, would produce a large flux of photons and neutrinos [Bhattacharjee and Sigl, 2000]. On the other hand, models in which the production of photons and neutrinos originates from secondary generated in the propagation of the cosmic ray with the cosmic background radiation produce much smaller fluxes.

In Figure 2.11, the photon models are represented by GZK [Ahlers et al., 2010], top-down (TD), Z-burst, (SHDM) [Gelmini et al., 2008], SHMD' [Ellis et al., 2006], whereas neutrino models are represented by TD [Sigl et al., 1999], Z-burst [Kalashev et al., 2009]. As can be observed, the current upper limits for photon and neutrino fluxes significantly disfavor top-down models. For photons, the limits are even more reliable, since they depend only on the simulation of electromagnetic showers and not on assumptions about hadronic interactions at high energies For additional information on Top-down mechanisms [Aab et al., 2016b].

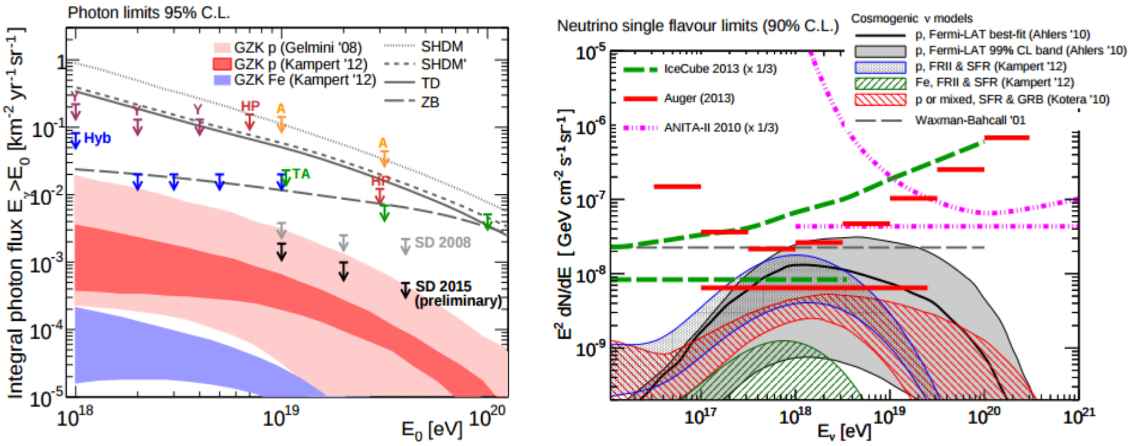

FIGURE 2.11: Limits on ultra-high energy photon and neutrino fluxes. **Left:** The expected values according to simulations based on Top-down and GZK models are displayed. The arrows identified by A, Y and TA represent the limits detected by the AGASA, Yakutsk and Telescope Array experiments, respectively. Those identified by SD and Hyb represent the results of the Auger Observatory detected by the SD and by the hybrid detection mode. **Right:** Limits on neutrino flux as measured by experiments such as IceCube, Auger and ANITA-II. Note that the limit imposed by the Auger Observatory data is the lowest among all experiments [Aab et al., 2016b].

2.8 The distribution of arrival directions

An important tool to reveal the origin of these particles is the distribution of the directions of arrival of the cosmic rays. In the following, we will present a detailed review of the results obtained by the Pierre Auger Collaboration with respect the identification of anisotropies in the cosmic ray flux.

2.8.1 Arrival directions of the most energetic cosmic rays detected by the Pierre Auger Observatory

As previously described, the identification of the origin of the most energetic cosmic rays is a difficult task due to the low intensity of its flow on Earth, also added the magnetic deflections that the particles suffer along their trajectories.
However, the distribution of the arrival directions can become an important tool for understanding the sources of cosmic rays if the distribution of these sources is not uniform and the magnetic deflections are small.

If the suppression observed in the flux of particles with energy above ~ 40 EeV is due to the GZK mechanism, a limitation on the distance at which a source could contribute to the flux on Earth is expected. If the distribution of sources in the local universe is not homogeneous, a correlation between the directions of events and nearby sources could be measured for the case of cosmic rays with low Z number. Using a first set of data from the Pierre Auger Collaboration in 2007 reported a correlation between the directions of arrival of the most energetic cosmic rays and potential extragalactic sources, using the Veron-Cetty and Veron catalog (VCV) of active galaxies nuclei [Véron-Cetty and Véron, 2006]. It measured the number of cosmic rays with energy above a threshold which reach a maximum angular distance of an active galactic nuclei (AGN), with distance $D < D_{max}$ and compared to predictions assuming isotropic distributions for the primary particles. Using vertical events, the most significant isotropy correlation was found for energy of 57 EeV, maximum angular distance 3.1° and maximum distance $D_{max} = 75$ Mpc. In 2010, the same analysis was applied to a data set with higher statistic a smaller correlation fraction was found, but still the result is only 2σ above the fraction expected by the isotropic distribution hypothesis and, therefore, does not provide significant indication of anisotropy.

Figure 2.12 shows the celestial maps obtained by the Pierre Auger Collaboration. The directions of arrival of the 27 events with energies above 57 EeV (black circle of 3.1° radius) and the directions of 472 AGNs at a distance of up to 75 Mpc from Earth are shown and also the direction of arrival of the 231 events used in the

2015 analysis. Black (white) circles represent vertical (inclined) events. The size of the circles refers to the energy of the event. The color scale is proportional to the relative exposure of the Pierre Auger Observatory. The white region is outside the field of view of the Auger Observatory for $\theta < 80°$. So far it has not been possible to

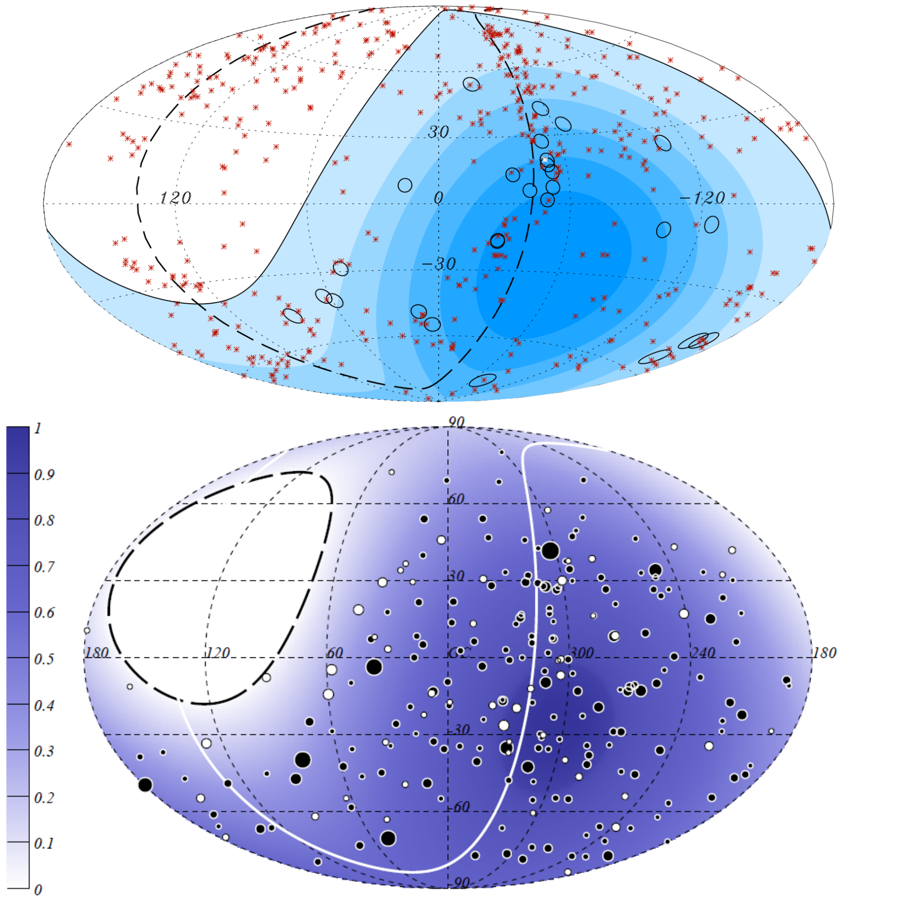

FIGURE 2.12: Map in Galactic coordinates: 27 events with energies above 57 EeV (black circles) and the directions of 472 AGNs (red dots) at a distance of up to 75 Mpc from the Earth, centered on an angular window of 3.1° **(Top)** and 231 events with energies above $E \geq 52EeV$. Black (white) circles represent vertical (inclined) events **(Bottom)**. The size of each circle scales with the energy of the event.[Aab et al., 2015d],[Abraham et al., 2007].

establish small scale correlations of the distribution of the arrival directions of the Auger data as possible sources or source regions. However, there is a region of 15°, centered in the direction of *Centarus A*, containing an excess of events. Although this excess has no statistical significance above 3σ, it is interesting to note that TA Collaboration has recently reported an excess for a similar angular scale.

2.8.2 Large Scale Anisotropy detected by the Pierre Auger Observatory

The distribution of arrival directions of cosmic rays on a large scale, carries an important clue to understanding the origin of these particles. In particular, establishing the energy for which the flux of extragalactic cosmic rays begins to prevail over the flux of particles originating in our galaxy would be an important step in understanding the links that should be imposed on possible sites accelerating in the galaxy and sources of the most energetic cosmic rays.

Thus, the large-scale distribution of the cosmic ray arrival directions as a function of their energies is an important tool for understanding the signatures of astrophysical scenarios, of galactic origin in the E $\sim$ 1 EeV region, and of extragalactic origin for higher energies. Currently there is no consensus on the energy at which the transition occurs in the cosmic ray flux detected galactic origin for extragalactic. Some models predict that such a transition occurs in the ankle region $\sim$ 4.8 EeV. In this case, large-scale anisotropies could be detected at lower energies, as a natural signature of the escape of cosmic rays from the interior of our galaxy, although the amplitude of such anisotropy patterns depends on the model of the galactic magnetic field adopted, the particle charge and distribution of sources. Furthermore, the possibility that the large scale galactic magnetic field is able to confine such particles, producing a dipole type anisotropy pattern, can not be ruled out. In this scenario, purely diffusive motions could confine lighter elements of galactic origin up to $\sim$ 1 EeV and the ankle of the spectrum would result from the longer confinement of heavier elements to higher energies [Calvez et al., 2010].

Dipole anisotropy or otherwise called dipole is an analogy to electromagnetism. Roughly it can be defined as an excess of events in a certain direction which is the direction of the dipole, and a deficit of events in the diametrically opposite direction. The dipole amplitude is defined as the difference between the number of cosmic rays observed in the excess region and the deficit region.

The flux of particles in a n direction to a dipole pattern with dipole amplitude defined as r in the $\hat{\mathrm{D}}$ direction is given by equation (2.14):

$$\Phi(\hat{n}) = \frac{\Phi_o}{4\pi}(1 + r\hat{D} \cdot \hat{n}). \tag{2.14}$$

The dipole pattern is very important in the study of cosmic rays since it is a structure that can appear in different physical situations. It can be through simulations, which shows that the cosmic rays generated in sources distributed in the galaxy and propagating by the magnetic field have a large scale, a dipolar anisotropy in the directions of arrival [Ptuskin et al., 1993].

In another case, when considering cosmic rays of extragalactic origin isotropically distributed, in this model considers that the transition between the galactic and extragalactic components occurs in energies below 1 EeV. In this case, the ankle would be the result of the degradation of the energy originated by the production of pairs and e^+ and e^- in the interaction of protons of extragalactic origin with the CMB [Berezinsky et al., 2005]. For energies below the GZK threshold of $\sim$ 60 EeV, cosmic rays can have a cosmological origin, traveling great distances until they are detected on Earth. Assuming that the effect of a possible distribution of sources is negligible, a dipole with an amplitude of 0.04% is induced by the relative motion of the galaxy in relation to the extragalactic referential. This effect is known as compton-getting [Compton and Getting, 1935]. Magnetic deflections could alter this dipole pattern leading to a complicated match between the incident direction of the particle in the halo of our galaxy and the direction of arrival on Earth. Additionally, as noted it is in [Harari et al., 2010], cosmic rays suffer a small variation in their momentum along their propagation through the galaxy, since the rotation of the Milky Way produces an electrical component for the galactic field, in the rest frame of the solar system. These two latter effects of magnetic deflections and particle momentum variation, lead to distortions of the dipole modulation as the magnetic rigidity decreases. Making relevant the contributions of harmonics of higher orders, such as quadrupoles and octopolos, for the anisotropies.

It is interesting to note that even at low energies where much of the information about the origin of the cosmic rays is lost, with the help of large scale anisotropy it is possible to obtain results on the cosmic particle production scenarios. Thus, the large-scale distribution of cosmic rays at various energy scales is an important observable that can provide information about the origin of the cosmic rays in the 10^{18} (EeV) scale.

Still in 2014, after the publication of the joint analysis of events of the Pierre Auger and TA (Telescope Array) Collaborations, a three-dimensional Rayleigh analysis was performed on the events detected only by the Pierre Auger Collaboration, including inclined events and an additional year of statistics, then combined the data set of showers with zenith angles up to 60° (usually used for anisotropy studies) and inclined showers ($60° < \theta < 80°$). From this analysis we found a large-scale dipole anisotropy for $E > 8 \times 10^{18}$ eV energies [Aab et al., 2015b]. An amplitude of the first harmonic in a straight ascension with $r = (4.4 \pm 1.0)\ 10^{-2}$ was measured with a probability of being a statistical fluctuation of $P(r) = 6.4 \times 10^{-5}$. Assuming that the only significant contribution to the anisotropy is given by the dipole component, this observation would correspond to a dipole of amplitude $d = 0.073 \pm 0.015$ pointing to $(\alpha, \delta) = (95° \pm 13°, -39° \pm 13°)$. No significant departure from isotropy is observed in the energy bin between 4 and 8 EeV the values is $d = 0.027 \pm 0.012$.

2.8.3 Angular power spectrum analysis

In general, from a mathematical point of view, any angle function $\Phi(\hat{\mathrm{n}})$ defined over the whole sphere can be expanded on a basis of spherical harmonics $Y_{\ell m}(\hat{\mathrm{n}})$

$$\Phi(\mathbf{n}) = \sum_{l \geq 0} \sum_{m=-\ell}^{m=\ell} a_{\ell m} Y_{\ell m}(\hat{\mathrm{n}}); \tag{2.15}$$

where $\hat{\mathrm{n}}$ represents a unit vector in a given direction (θ, ϕ) and the expansion coefficients are obtained from the following expression

$$a_{\ell m} = \int d\hat{\mathrm{n}}\ \Phi(\mathbf{n}) Y^{*}_{\ell m}(\hat{\mathrm{n}}). \tag{2.16}$$

Now take $\Phi(\hat{\mathrm{n}})$ as a function that describes the angular distribution of the directions of arrival of the cosmic rays on the celestial sphere. Thus, $\int \Phi(\hat{\mathrm{n}}) d\hat{\mathrm{n}} = N$, where N is the total number of observed cosmic rays. Also consider another function $\Delta(\hat{\mathrm{n}})$, with a mean value $\langle \Delta(\hat{\mathrm{n}}) \rangle = 0$, capable of measuring the deviation of the isotropy. In the case of a complete exposure of the sky, the functions $\Phi(\hat{\mathrm{n}})$ and $\Delta(\hat{\mathrm{n}})$ are related by

$$\Phi(\hat{\mathrm{n}}) = \frac{N}{4\pi}[1 + \Delta(\hat{\mathrm{n}})]. \tag{2.17}$$

The simplest non-trivial situation to describe the underlying process is then to consider that the anisotropies cancel in ensemble average and produce a second order moment that does not depend on the position on the sphere but only on the angular separation between $\hat{\mathrm{n}}$ and $\hat{\mathrm{n}}'$. Thus, the underlying $a_{\ell m}$ coefficients vanish in average and are not correlated to each other [Deligny, 2016]. By identification, we obtain a diagonal covariance for the coefficients a_{lm},

$$\langle a_{\ell_1, m_1} a^*_{\ell_2, m_2} \rangle = C_{\ell_1} \delta_{\ell_1 \ell_2} \delta_{m_1 m_2}, \tag{2.18}$$

where C can be identified as the angular power spectrum of the fluctuations of the function $\Delta(\hat{\mathrm{n}})$, defined by

$$C_\ell = \frac{1}{2\ell + 1} \sum_{m=-\ell}^{\ell} |a_{\ell m}|^2. \tag{2.19}$$

The angular power spectrum is a two-point function in space ℓ, that provides information on the correlation between variations of the flux on an angular scale $\simeq 1/\ell$ radians.

The Pierre Auger Collaboration recently reported a large-scale anisotropy for cosmic rays with E> 8 EeV [Aab et al., 2015b] and zenith angle $\theta < 80$. The aim to search anisotropy in multiple angular scales was reviewed in the Ph.D. thesis of Jaime Souza, student of our group [Souza de Oliveira, 2016], he studied the distribution of the directions of arrival of the cosmic rays of with energy above 4 EeV, by measuring its angular power spectrum, C_ℓ. The results obtained, after the correction due to the partial exposition of the Pierre Auger Collaboration, is shown in figure 2.13, for 4 EeV $\leq E \leq 8$ EeV, the left , and $E > 8$ EeV, the right.

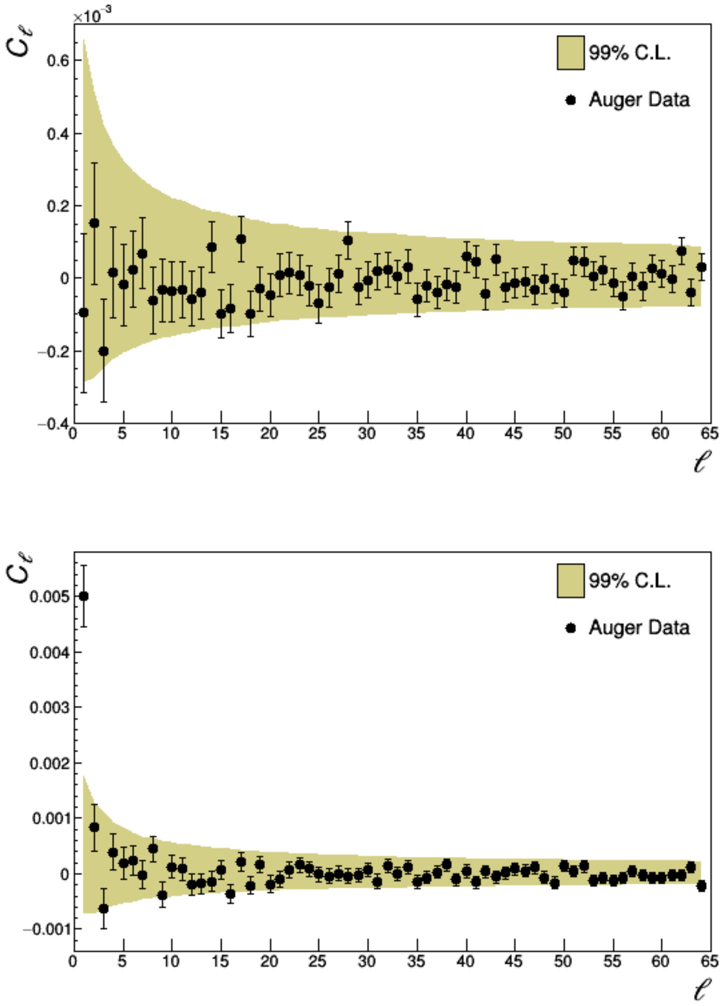

FIGURE 2.13: Results of the angular power spectrum to events measured by the Pierre Auger Observatory with **Top:** 4 EeV $\leq E \leq 8$ EeV. **Bottom:** $E > 8$ EeV. [Souza de Oliveira, 2016].

Although there is no evidence of anisotropy in the energy range of 4 EeV $\leq E \leq 8$ EeV, there is a significant deviation of isotropy at the dipole scale ($\ell = 1$) for $E \geq 8$ EeV, increasing the information reported in [Aab et al., 2015b]. The results of this analysis will be used in the section 4.3.

Chapter 3

The Pierre Auger Observatory

The Pierre Auger Observatory has been designed to study the nature of high energy cosmic rays and understand their origin and properties. The Pierre Auger Observatory is the largest cosmic ray observatory ever built. Located in the city of Malargüe, Province of Mendoza in Argentina it was planned to study the UHECRs with an emphasis on those with energy greater than $\sim 6 \times 10^{19}$ eV.

In this chapter, we will describe the characteristics of detectors: the surface (SD) and the fluorescence detectors (FD), used by the Pierre Auger Observatory in collecting data on ultra-energetic cosmic rays and also the methods of reconstructing the energy and the directions of arrival of these events.

3.1 The detectors of the Pierre Auger Observatory

The aim of the Pierre Auger Collaboration is to measure the flux, mass composition and arrival direction distribution of cosmic rays from 10^{18} eV up to the highest energies. The experiment is located between latitudes 35° and 35.3° and between longitudes 69.0° and 69.4° and at an average altitude of 1400 meters above sea level. The experiment began its operation in 2004, still without occupying all its current area and was finalized in 2008 covering a total of 3000 km^2. It has been operating for more than 10 years.

The figure 3.1 shows on the map the geographical location of the Observatory and its detectors. It features an array of 1660 water-Cherenkov particle detector stations spread over 3000 km^2 over looked by 24 air fluorescence telescopes. Besides that, three high elevation fluorescence telescopes overlook a 23.5 km^2, 61 detector array with spacing of 750 m (the Infill).

The atmospheric conditions at the place where the detectors are installed need to be constantly monitored, since they interfere significantly in the measurements made by the SD and the FD. In particular, the amount of clouds and aerosols (heavier particles suspended in the atmosphere) influence the production and attenuation of fluorescent light, causing variation in the measurements made by the FD.

The monitoring system for these parameters consists of LIDARs (Light Detection and Ranging) near the buildings where the fluorescence telescopes are installed. Their data provide information on altitude and cloud cover as well as their depth and opacity, in addition to the aerosol scattering and atmospheric absorption properties.

In addition to LIDAR, there are two laser devices of similar function, located approximately in the center of the network of surface detectors. They are: the CLF (Central Laser Facility), in operation since 2003, and the XLF (eXtreme Laser Facility), which was installed in 2008 and includes an automated calibration system capable of measuring the energy deposited in the atmosphere by the fired laser beam as well as its polarization [Aab et al., 2015e].

The main feature of the Auger Observatory is to use two independent high-energy cosmic ray detection techniques, fluorescence light recorded by telescopes and particles signals in surface Cherenkov stations. By combining each technique in order to complement each other, this combination leads to the concept of a hybrid detection. The information of the two detectors are combined together to give an accurate energy and direction measurement for those events simultaneously observed by SD and FD (hybrid events).

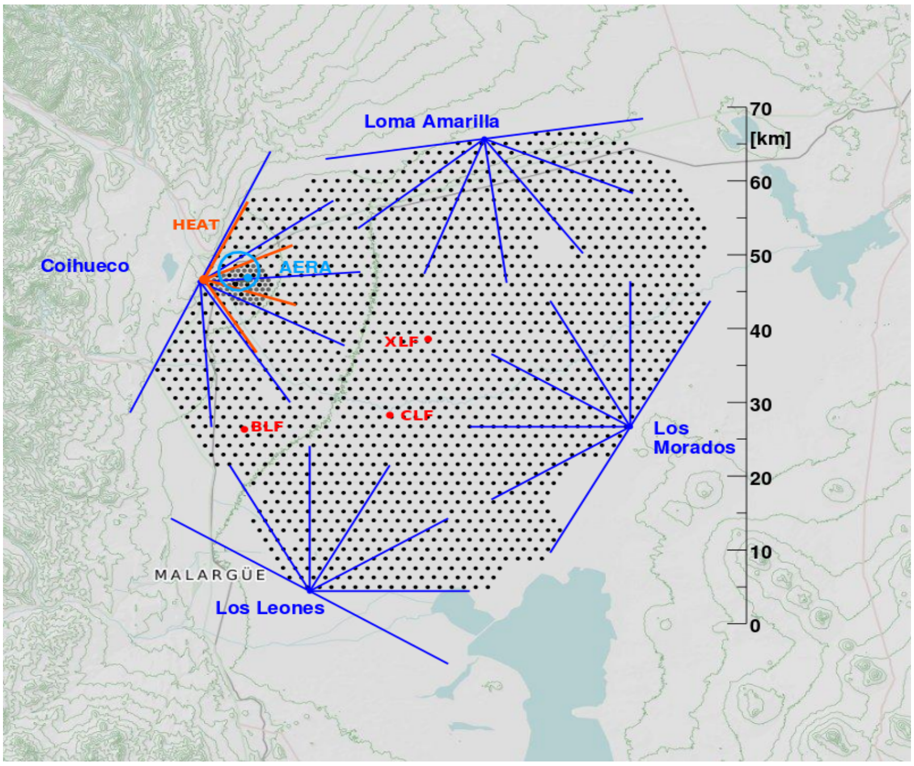

FIGURE 3.1: Geographical map showing the positions of the detectors at the site of the Pierre Auger Observatory. The black dots represent the 1600 surface detectors stations installed along 3000 km^2 and the blue lines show the field of view of the fluorescence telescopes, each with the field of view of its six telescopes [Aab et al., 2016b].

Below are explained the physics and functioning behind these techniques at the Pierre Auger Observatory.

3.2 The Fluorescence Detector

The Fluorescence Detector (FD) of the southern observatory uses the same detection method as the successful Hires (High Resolution Fly's Eye Experiment) experiment [Sokolsky and HiRes Collaboration, 2011].

The 24 telescopes of the FD overlook the SD array from four sites, each FD building houses six independent telescopes each covering a field of view of 30° × 30° in azimuth and elevation. The telescopes face inside the array so that the combination of the six telescopes provides full 180° coverage in azimuth.

In addition, the site Coihueco houses three more telescopes in one station apart, a subset known as HEAT (High Elevation Auger Telescopes). In the case of HEAT, the elevation of the telescopes is optimized for observing lower energy showers up to 10^{17} eV.

These buildings are on hills located at strategic points on the edges of the SD. Each building received a name equal to that of the hill where it is located: Los Leones, Coihueco, Loma Amarilla and Los Morados. Figure 3.2 shows a example of FD site.

FIGURE 3.2: FD building at Los Leones during the day. Behind the building there is a communication tower. This photo was taken during daytime when shutters were opened because of maintenance. [Aab et al., 2015e].

Therefore, a total of 27 fluorescence telescopes measure the development of the extensive air shower, focusing on the ultraviolet radiation generated by the interaction between the shower particles and the nitrogen molecules along their trajectory. Through this information compiled by FD, it is possible to determine the energy of the primary and the depth in the atmosphere in which the production of particles of the shower reaches a maximum value.

Each detector is an optical system composed of an entrance window with light filter, a circular aperture, corrector ring, focusing mirrors and a camera with photomultipliers. Fluorescence radiation is emitted isotropically and it is incident on a circular diaphragm of 1.1 m radius covered by a filter whose transmission is above 50% at a wavelength between 310 and 390 nm in the UV range, which contains all of the important fluorescence emission bands of molecular nitrogen. The function of this filter is to reduce background light flux and to improve the perceived signal-to-noise ratio. The corrector ring is an optical device with the function of correcting aberrations in the image obtained by the camera.

After passing through the filter, the fluorescent light is focused on a spherical focal surface with a radius of curvature of 3400 mm. Due to its large area (13 m^2), the mirror is segmented to facilitate transportation and production costs. This light is then focused on a camera built on a single aluminum block, as shown in Figure 3.3.

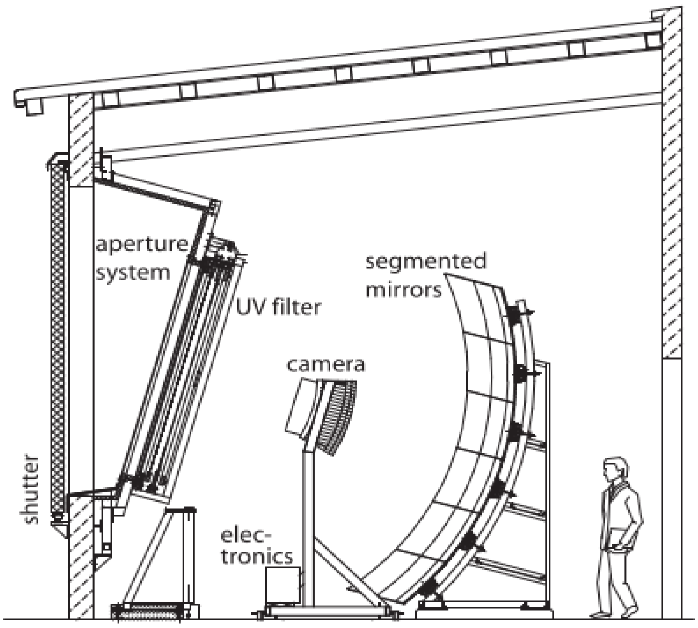

FIGURE 3.3: Schematic of the main components of an FD. [Aab et al., 2015e].

The detector aperture can be seen in Figure 3.4. The sensitive component of the detector is the camera located in the focus of the mirror. The function of the photomultiplier tube (PMT) is to convert fluorescence light into an electrical signal proportional to the amount of incident photons. The PMTs contained in this camera

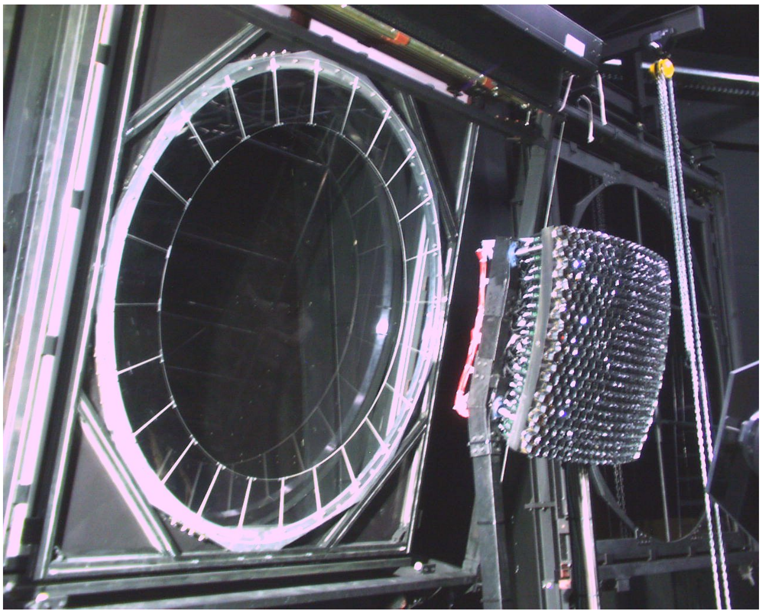

FIGURE 3.4: View of the aperture with the corrector rings and the camera on the right. [Aab et al., 2015e].

are arranged in a matrix of 22 rows by 20 columns, thus totaling 440 pixels. The passage of an air shower produces a trace in the PMTs, as shown in the figure 3.5, where the color code indicates the temporal differences in the arrival of the radiation in the camera, with the red indicating the photons that arrived last at the detector.

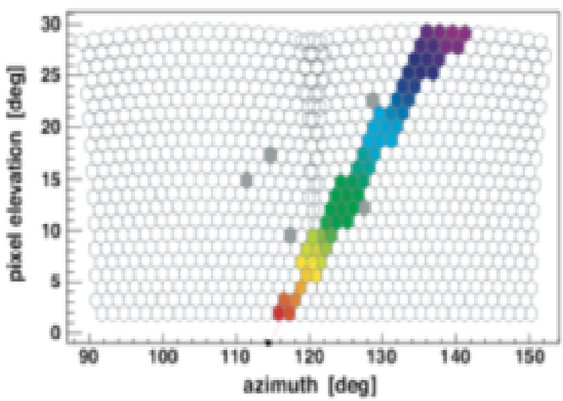

FIGURE 3.5: A trace produced by a shower showing pixels triggered. [Aab et al., 2015e].

The shower is essentially a front of relativistic particles propagating in the atmosphere along an axis and its passage will appear in the camera like a straight line of pixels with signals that present a temporal sequence.

The geometry of the trace obtained by the detector along with the temporal information of the signals of each pixel will be used by the Data Acquisition System (DAQ) in the discrimination of real events coming from showers and spurious events.

3.2.1 Calibration of fluorescence detectors

The fluorescence detector has two basic tasks: the first is to reconstruct the longitudinal profile of the shower and the total number of fluorescence photons generated. Detection is done at a certain distance from the shower which, due to the limited field of view of the detector and scattering of the photons by the molecules present in the air, involves the observation of only a fraction of the light originally generated.

First the detector must be calibrated relating the integrated signal of PMTs with the number of photons observed. The absolute calibration of the FD telescopes is done using accurately calibrated light sources and a cylindrical diffuser that illuminate the camera uniformly. It is an end-to-end procedure that takes into account the transmission of the filter, the reflectivity of the mirror and the response of the camera photomultipliers. In addition to the absolute calibration, a relative calibration is performed. Relative calibration is used to correct variations in absolute calibration that may occur due to seasonal changes, night-to-night fluctuations in the operation and difference in camera response. With the camera calibrated, the number of photons collected by the detector is only a fraction of the total generated along the axis of the shower. Obtaining the total number of photons emitted by the shower depends on the atmospheric absorption and scattering properties of the light and the geometry of the detector.

Furthermore, the conversion of light intensity measured in deposited energy through fluorescense yield requires the knowledge of the atmospheric conditions. The Pierre Auger Observatory has an extensive atmospheric monitoring program [Abraham et al., 2009] whose objective is to measure the parameters for the determination of the fluorescence yield and to study the Rayleigh scattering (scattering by the atmosphere molecules) and the Mie scattering (scattering by heavier particles called Aerosol). In summary, monitoring is done by:

CLF (Central Laser Facility): Located in the middle of the Auger Observatory, it is a center that houses a UV laser and an optical device capable of generating a light beam calibrated in the sky. The CLF is a test beam used to monitor the atmosphere and, in parallel, the absolute calibration.

Lidar (Light Detection And Ranging): High repetition pulsed UV laser, generate pulses of light in the atmosphere in directions of interest. Light scattered back to the detector is detected by photomultipliers installed in the parabolic mirror focus. Its goal is to monitor the atmosphere in the FD region. When a high energy event occurs, the region of the shower plane is also scanned. FD events in coincidence with LIDAR triggers are discarded.

APFs (Aerosol Phase Function Monitor): Determines aerosol scattering properties in the atmosphere using horizontal light beams produced by a Xenon lamp to calculate the probability of light scattering in a certain direction.

HAM (Horizontal Attenuation Monitor): Determines the horizontal extinction length combined with the Rayleigh and Mie scatterings by the light intensity measured near a light source (mercury vapor lamp) and away from that source (approximately 50 km).

The properties of the Mie and Rayleigh scatterings are used to infer the total number of fluorescence photons generated in the passage of the shower. As photons coming Cherenkov effect may also contribute to the signal in FD, this effect must also be taken into account. At the end, after including the dependence with the atmospheric parameters, the flourescence yield converts to energy the total number of photon. Due to the limited field of view of the telescopes only part of the longitudinal profile is observed and an adjustment with the function Gaisser Hillas is employed. The measurement of the longitudinal profile of the showers is based on the empirical formula of Gaisser and Hillas, which gives the total energy deposited longitudinally by the shower and its maximum (dE/dX_{max}) as a function of the amount of matter traversed in the atmosphere, $X = X_{max}$.

$$f_{GH}(X) = \left(\frac{dE}{dX_{max}}\right)\left(\frac{X - X_o}{X_{max} - X_o}\right)^{(X_{max}-X_o)/\lambda} exp((X_{max} - X)/\lambda). \qquad (3.1)$$

Where the free parameters, X_o, λ are determined by the maximum likelihood method.

The fluorescence technique is based on the use of the atmosphere on the observatory site as a kind of gigantic calorimeter, where the emitted fluorescence light is proportional to the energy deposited in the air by the charged particles of the showers. The Gaisser–Hillas fit provides a measurement of the total track length. The calorimetric measurement of the energy provided by the fluorescence technique has to be corrected for the missing energy essentially due to muons and neutrinos, which are not contributing to the observed energy, this correction is evaluated with simulation programs. The telescope used at the Pierre Auger Observatory has systematic uncertainty of 14% [Aab et al., 2013] in determining the energy. This total uncertainty is the result of systematic errors in calibration, reconstruction, atmospheric parameters, fluorescence yield and invisible energy. The disadvantage of this detector is its sensitivity that only allows it to operate about 10% - 15% of the time.

3.3 The Surface Detector

This is a technique well known and used in other experiments such as AGASA (The Akeno Giant Air Shower Array) [Yoshida et al., 1994], which was previous to the Pierre Auger Observatory and to TA (Telescope Array) [Kawai et al., 2008]. In the Pierre Auger observatory, water Cherenkov tanks are used as surface detectors.

The Cherenkov effect occurs when a charged particle crosses a material medium with velocity v greater than the velocity of light in this medium of refractive index n. Under these conditions, a cone of light is emitted with a spectrum centered mainly on the ultraviolet range. The emission angle of the Cherenkov radiation is described by $\cos\theta = \frac{1}{n\beta}$, where θ is the emission angle, n the refractive index of the medium and $\beta = v/c$ is related to the velocity v of the particle.

The surface detector network (SD) consists of 1660 detectors, spaced 1,500 m apart, forming a network of 3000 km^2 (SD-1500 m) fully efficient in the detection of primary energy particles above 3×10^{18} eV. As from 2008, another smaller network, with an area of 23.5 km^2, consisting of 61 stations SD spaced 750m (SD-750 m), was added and configured to detect the energy of the primary particles below 3×10^{17} eV. Continuously the two networks record the signs left by the SD muonic and electromagnetic components from the air shower formed by the interaction of primary particle with atmospheric molecules [Aab et al., 2015e].

Each surface detector station (SD) consists of a 3.6 m diameter water tank containing a sealed liner with a reflective inner surface. The liner contains 12,000 liters of ultrapure water which is expected to maintain its quality without degradation for the lifetime of the experiment, estimated at 20 years. Three nine-inch-diameter PMTs are symmetrically distributed on the surface of the liner at a distance of 1.20 m from the center of the tank and look downwards into the water to collect the Cherenkov light produced by the transit of relativistic charged particles.

The water height of 1.2 m makes it also sensitive to high energy photons, which convert to electron-positron pairs in the water volume. The function of these photomultiplier cells is to record the signals produced by the Cherenkov light reflection inside the tank, measured in VEM[1] units.

The signal recorded by the PMTs is digitized and filtered by Flash Analog to Digital Converter (FADC) at a frequency of 40 Mhz. The amplitude of the signal is encoded in 1024 channels and both the anode signal (low gain) and the last dynode signal (high gain) are recorded. These two information are used so that the SD matrix is able to accurately collect information from the detector tanks near the center of the shower with a flow of 1000 particles/μs (due to the low gain the anode does

[1]Vertical Equivalent Muon (VEM), represents the total charge in the PMTs deposited by a muon which completely traverses a station vertically through its center.

not saturate), as well as further away from that point with a flux of the order ~ 1 particles/μs (the low flux allows the use of the dynode) [Abraham et al., 2010].

In this way the detector has the dynamic domain necessary to properly observe the entire lateral distribution[2] of the shower. Even with this flexibility, very energetic showers can generate a number of particles capable of saturating the detector and these cases should be analyzed separately. Although they operate together, each station is a unit that operates autonomously with its own electronics and communication system.

The surface detector station is self-contained. A solar power system provides the electrical power for the PMTs and the electronics package consisting of a processor, GPS receiver, radio transceiver and power controller.

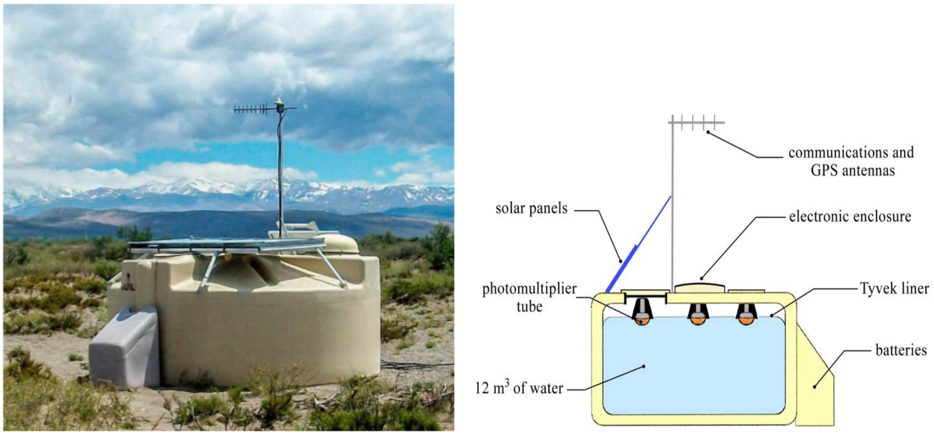

FIGURE 3.6: Parts of a detector tank. **Left:** real tank installed in the Pierre Auger Observatory. **Right:** Illustration of the main components of the tank and their respective positions. [Aab et al., 2016b].

3.3.1 Calibration of surface detectors

Calibration is the procedure that relates the FADC signals with physical quantities [Aab et al., 2016b]. The calibration of the detector is deduced from the background muons. The amount of Cherenkov light produced will be proportional to the energy

[2]Lateral Distribution Function (LDF) of the showers, which describes how the particles are distributed as a function of distance from the shower core.

deposited by the muon. This information resulted in the definition of a standard unit of measurement known as vertical equivalent muon (VEM), previously described.

The measurement of the muon charge spectrum allows to deduce the charge value for the signal produced by a single, central, vertical muon, Q_{VEM} , from which the calibration is inferred for the whole dynamic range. The decay constant of the muon signal is related to the absorption length of the light produced which depends on the inner reflectivity and the purity of the water. The signal decay constant correlates with the so called area-to-peak (A/P) ratio of the signal:

$$A/P = \frac{Q_{VEM}}{I_{VEM}} \tag{3.2}$$

where I_{VEM} is the maximum current of the muon signal. This area-to-peak ratio is a routine monitoring quantity that is directly available from the local station software.

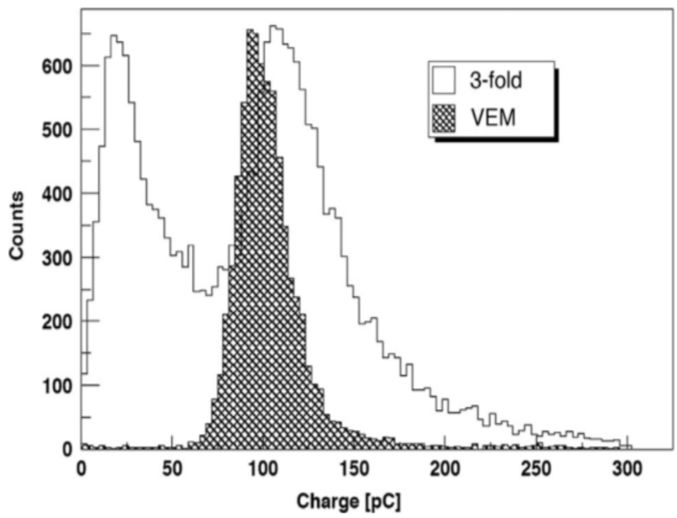

FIGURE 3.7: Charge spectrum obtained when a surface detector is triggered by a 3-fold coincidence among its photomultipliers (open histogram). The shadow histogram shows the spectrum when triggered to select only vertical and central muon. The bin containing the peak of the scintillator triggered spectrum is defined as a vertical equivalent muon. The first peak in the open histogram is due to low energy and corner-clipping muons convolved with the 3-fold low threshold coincidence, the second peak is due to vertical throughgoing atmospheric muons. [Aab et al., 2015e].

3.3.2 Trigger system and performance of SD stations

To avoid the selection of stations in the SD network, which are driven by atmospheric muons instead of particles from the shower generated by UHECRs, a selection algorithm is adopted in the triggers performed at each station in the ground [Abraham et al., 2010]. The trigger consists of a hierarchical structure of five levels (T1, T2, T3, T4 and T5). The first two levels of trigger selection occur in the same station, i.e., individually in each tank, while the other levels already occur in the CDAS, that is central data acquisition system.

The T3 trigger is based on the spatial-temporal correlation between the different stations. This allows to define an event as a set of signals from at least three surface stations with the appropriate temporal and spatial distance to be considered as a possible shower generated by UHECR.

Finally, during the processing of the data, the next triggers are activated: T4 (physical event). Once spatial compatibility between neighboring detectors is confirmed according to a shower, the T4 trigger is applied. This is a new algorithm that involves the physics of showers. Since it eliminates the tanks with accidental signals of atmospheric muons and results the first step in the identification of vertical shower pausibles to be reconstructed.
The T5 trigger (high quality events), known as fiducial trigger is associated with a quality cut of the event. It consists of the largest signal station having the first 6 closest neighbors in operation (not necessarily all with signal) at the time of measurement, ensures that the shower core is not located at the edge of the SD network. More details in [Abraham et al., 2010], [Aab et al., 2016b].

3.3.3 Reconstruction of events by Pierre Auger Observatory surface detector

The Pierre Auger Observatory combines information obtained from data collected by surface and fluorescence detectors in order to obtain greater accuracy in the reconstruction of these quantities.

3.3.3.1 Reconstruction of vertical events

The reconstruction of the energy and direction of arrival of the vertical events is based on the time registers and the values of the signals collected in each SD station triggered by the atmospheric shower. Through these parameters, it is possible to obtain the "geometry" of the shower, that is, the position where the shower axis touches the ground, called the core, and from there, reconstruct the direction of arrival of the primary particle. The energy of the events detected by the SD is reconstructed using a characteristic value of the shower signal measured at a distance where its fluctuation is minimal.

The first part of the reconstruction of a particle shower is the identification of real events. For a shower created by a ultra-high energy cosmic ray to be detected by the SD, it is necessary that many conditions, related to the signals left by the shower in the tanks Cherenkov, are satisfied. This is possible through the trigger system developed for the detector. This system is described in [Abraham et al., 2010].

The second part is the actual reconstruction of the characteristics of the showers. First, an adjustment of the geometric parameters is made. The direction of arrival of the shower is obtained by adjusting a model that considers the front of the shower as a ball inflating with the speed of light, c. This information is obtained through the activation time of the detectors. A simple way to visualize the setting used in the experiment is considering a flat front of particles. In this case the activation time of the i-th detector is given by: t_i^{pl} is the expected time of arrival of the particle to a detector located at (x_i, y_i);

$$t_i^{pl} = T_o - (ux_i + vy_i)/c. \tag{3.3}$$

Where we can adjust the parameters T_o (the time of arrival in the center of the shower), u, v (where the last two give the shower direction). From the equation (3.3), modifications are made to be able to include curvature effects that is equivalent to a delay in the signal. At this point, the accuracy in determining the triggering time of the detectors and the synchronization between the tanks are essential for a good determination of the geometric parameters of the shower. In particular, angular resolution in the direction of arrival of the cosmic rays detected by the Pierre Auger Observatory.

The surface detector only samples the properties of an air shower at a limited number of points at different distances from the shower axis, is not able to record all the air shower. Therefore, an adjustment in the lateral distribution that describes the decay of the signal with the distance to the core of the shower needs to be implemented. Studies show that there is a specific distance in relation to the core of the shower, which should serve as a parameter to minimize errors in the reconstruction of energy and the direction of arrival of the primary particle [Newton et al., 2007]. From the signal recorded in each detector, the lateral distribution function (LDF) or the particle density as a function of the distance from the core can be derived. The LDF for an atmospheric shower models the signal registered in the surface detectors according to some parameters: the perpendicular distance to the shower axis, r, the shower signal at a specific distance, k, and the slope of the signal, β, which depends on the zenith angle. The modified Nishimura-Kamata-Greisen (NKG) function is classically the most used to model the lateral distribution of the shower [Kamata and Nishimura, 1958], defined by

$$S(r) = k\left(\frac{r}{r_s}\right)\left(1 + \frac{r}{r_s}\right)^{-\beta}, \tag{3.4}$$

where β is the slope of the LDF, $r_s = 700$ m, $k = 250$ m and $S(1000)$ is the sign of a station at 1000 m from the shower axis. The value of β is fixed and depends only on the zenith angle of the shower as: $\beta = 3.3 - 0.9\sec\theta$. From the adjustment of the LDF the values of $S(1000)$ and the position of the nucleus are obtained.

The parameter $S(1000)$ is used as an energy estimator because simulations show that the fluctuations of the signals in the tanks have a minimum near the region $r = 1000$ m from the core. The error of $S(1000)$ has been experimentally determined and found to be better than 12% for the highest energies [Ave, 2007]. The parameter

$S(r)$ has dependence on the zenith angle θ of the shower, decreasing as the inclination increases.

This relation is empirically removed through the CIC - Constant Intensity Cut method. Assuming an approximately isotropic flux of cosmic rays on Earth with a given energy E, the intensity of that flux must be equal when observed at the same solid angle [Aab et al., 2016b]. Using the data measured in the experiment, the CIC method [Abreu et al., 2011] consists of constructing a histogram as a function of the zenith angle. From this histogram can be obtained the cut-off value $S(1000)_{cut}$ such that the particles flux with S(1000) $> S(1000)_{cut}$ is constant in the solid angle element. This procedure gives rise to the curve shown in figure 3.8 and parameterized by equation 3.5.

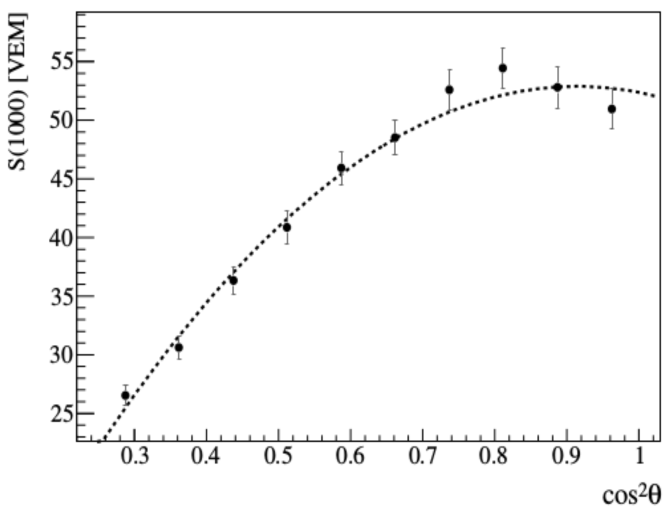

FIGURE 3.8: The derived signal attenuation curve, CIC(θ) to eliminate the dependence of the energy estimator S(1000) with the zenith angle, The solid line represents the fit described by a polynomial of second order [Abreu et al., 2011].

$$CIC(\theta) = 1 + ax + bx^2. \tag{3.5}$$

With $x = \cos^2(\theta)$ - $\cos^2(\theta_0)$. The mean angle $\theta_0 = 38°$ is the reference used to convert S(1000) to S_{38} = S(1000)/CIC(θ), thus eliminating angle dependence. Relating S_{38} measured in VEM with the energy of the cosmic ray finally a calibration in terms of the energy is obtained. This relation can be obtained via Monte Carlo simulations or using the information from the fluorescence detector in a cross-calibration procedure. The second method is the one employed in the Observatory because it minimizes the systematic errors resulting from the simulations.

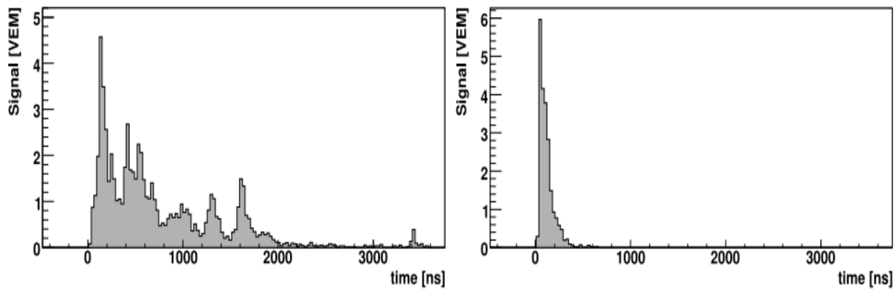

FIGURE 3.9: Comparison between the signal of an SD station generated by a vertical event with reconstructed zenith angle $\sim 22°$ (left) and inclined with reconstructed zenith angle of $\sim 80°$ (right). Both signals measured 1 km from the core of the shower. [Aab et al., 2014c].

3.3.3.2 Reconstruction for Inclined Events

The analysis of inclined showers, that is, with zenith angles greater than 60°, allows for an increase in detector exposure of $\sim$ 30%, extending the coverage of the sky to unobservable regions when considering only vertical events. They are characterized by a predominance of muonic component on the ground (the electromagnetic component is absorbed before reaching the ground) and a very elongated shape and asymmetric due to the curvature of the trajectory of the muon by the geomagnetic field. Inclined showers are quite different from vertical and require different reconstruction techniques. Figure 3.9 shows the signal of a vertical event ($\theta \sim 22°$) compared to another signal produced by an inclined event ($\theta \sim 80°$), both recorded by tanks distant 1 km from the shower core. Due to the contribution of the electromagnetic component, the signal recorded by the vertical event is more scattered in time, whereas in the inclined event the signal is more concentrated because it is basically dominated by the muonic component of the shower. In addition, inclined events are capable of triggering a much larger number of SD stations and, consequently increase detection efficiency, since it depends on $\sec\theta$ [Aab et al., 2014c].

This fact leads to changes in the LDF. The selection of inclined events basically follows the same algorithm considered for vertical events. The arrival direction for events with zenith angles greater than 60° is also obtained similarly to events with zenith angles of less than 60° by adjusting the initial times measured by the driven stations relative to a flat shower front corrected for small delays associated with the propagation of muons [Cazon et al., 2004].

Instead of an LDF, density maps of the number of muons in the ground are obtained in Monte Carlo simulations for different zenith angles and azimuths in the presence of the geomagnetic field at the Auger site. These simulations are used to adjust the location of the shower core and the normalization of the total number of muons for a shower, originated by a proton 10 EeV (10^{19}) eV, called parameter N_{19}, which is used as an energy estimator.

3.3.4 Hybrid detection technique

In the hybrid mode the FD information are combined with SD, improving the geometry determination and taking advantages of the calorimetric measurement of the energy from FD.

Hybrid events detected by SD and FD provide independent energy reconstructions. As the energy reconstructed by FD is more accurate than that reconstructed by SD, it is used to calibrate the reconstructed energy of the events (vertical and inclined) detected by the SD. FD measurements must pass through quality cuts to select high quality longitudinal profiles, observed in good weather conditions, including the condition that the maximum depth of shower X_{max} is within the field of view of the telescopes.

The high quality hybrid events, with reconstruction of smaller zenith angles 60° are used as a reference to relate the SD signal with the quasi-calorimetric measurement by the FD of the energy deposited by the shower, E_{FD}. The correlation between E_{FD} and S_{38} is obtained by the maximum likelihood method, taking into account the evolution of uncertainties with energy. It can be described as a power law:

$$E_{FD} = A(S_{38}/VEM)^B. \tag{3.6}$$

Where the parameters A and B are adjusted from the data with values equal to $(1.90 \pm 0.05) \times 10^{17}$ eV and 1.025 ± 0.007, respectively. Due to the large number of events recorded, the systematic errors associated with the reconstruction of SD energy due to cross-calibration are less than 2% over the measured energy range [Aab et al., 2013].

Finally, in the case of inclined events with zenith angles between 60° and 80°, it is possible to relate the value of N_{19}, with the energy of the primary particle, similarly to that used in the reconstruction of vertical events. Taking into account the differences in quality cuts and in the reconstruction of inclined events, hybrid events with zenith angles greater than 60° are used. The cross-calibration is described by a power law that adjusts to the shower signal as a function of the deposited energy collected by the fluorescence telescopes

$$N_{19} = A'(E_{FD}/10^{19}eV)^{B'}, \tag{3.7}$$

where the parameters A' and B' are obtained by the maximum likelihood method. Inverting the adjusted function, the energy estimated by SD is given by $E_{SD} = A(N_{19})^B$, with the following calibration parameters: $A = (5.701 \pm 0.086) \times 10^{18}$ eV and $B = (1.006 \pm 0.018)$. The figure 3.10 shows the correlation between the parameter N_{19} and the energy reconstructed by FD, E_{FD}, for 255 hybrid events with zenith angle $\theta \geq 60°$. Such adjustment generates a resolution of $(19 \pm 1)\%$ for the resulting mean energy reconstructed by SD.

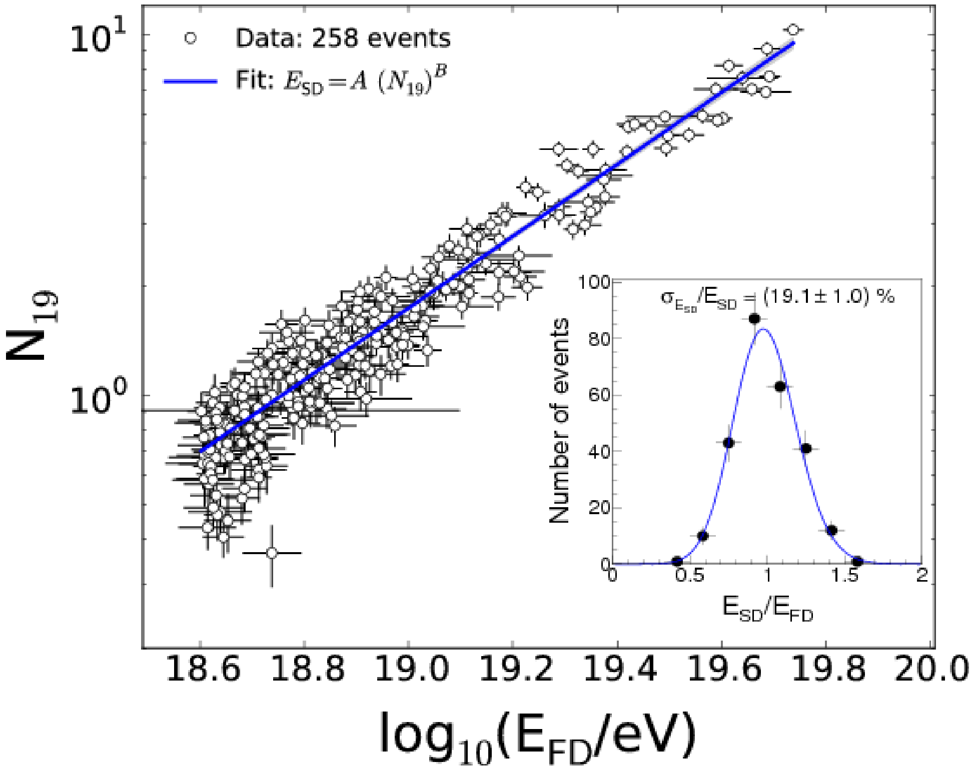

FIGURE 3.10: Correlation between shower size and energy deposited in the atmosphere, as collected by the FDs, for inclined hybrid events. The blue line represents the best fit for the data. The corresponding distribution of the ratio of the energy of the SD, E_{SD}, and the energy of the FD, E_{FD}, is shown in detail [Aab et al., 2015c].

Chapter 4

Phenomenological analyzes using Pierre Auger data

This chapter, last part of the thesis, is dedicated to describe the phenomenological analyzes that we have performed aiming to infer characteristics of the cosmic ray sources such as energy spectrum and composition. First, we will review a combined fit reported by the Pierre Auger Collaboration [di Matteo, 2016] using energy spectrum and composition data. In the following, we will present our phenomenological analyzes to improve this result, i.e., including also informations about the events arrival direction on Earth. Finally, we investigate the effect of Lorentz invariance violation on propagation of cosmic rays from sources to Earth by comparing its prediction with Pierre Auger data.

4.1 Combined spectrum-composition fit

An attempt to simultaneously reproduce the data of the Pierre Auger Collaboration related to the Auger spectrum (Figure 2.7) and to the maximum shower depth, X_{max} (Figure 2.9) with a simplified model was reported in [di Matteo, 2016]. This model assumes identical sources of UHECRs homogeneously distributed, characterized by the emission of Hydrogen (^{1}H), Helium (^{4}He), Nitrogen (^{14}N), and Iron (^{56}Fe), with an emission spectrum having a suppression factor dependent on the R_{cut} rigidity of the particles,

$$\frac{dN_{inj,i}}{dE} = \begin{cases} J_{oa_i}(E/E_o)^{-\gamma}, & E/Z_i < R_{cut} \\ J_{oa_i}(E/E_o)^{-\gamma} exp[1 - E/(Z_i R_{cut})], & E/Z_i > R_{cut} \end{cases} \tag{4.1}$$

where J_o is a normalization factor, $E_o = 10^{18}$ eV, and Z_i is the atomic number of the $i-th$ injected nuclide, whose fraction in the sources, a_i, is normalized in such a way that, $\sum_i a_i = 1$. This model is not able to reproduce the data measured over the entire energy range. Therefore, the data are fitted only for energies above the ankle ($E \geqslant 10^{18.7}$ eV). Moreover, there is no hypothesis about the nature of a possible component responsible for the contribution of UHECRs to the energy spectrum in the region below the ankle.

The free parameters of the fit are: the injection normalization factor of the J_o, the injection spectral index γ, the cut-off rigidity R_{cut} and the fractions of the elements in the sources, (three free parameters: a_H, a_{He}, a_N, since the fourth is subject to the bond $a_H + a_{He} + a_N + a_{Fe} = 1$). The best fit obtained occurs for $\gamma = 0.94^{+0.9}_{-0.10}$, $R_{cut} = 10^{18.67 \pm 0.03}$ V, with a deviance (generalized χ^2) per degree of freedom $D_{min}/n = 178.5/119$.

Figure 4.1 shows the deviation from D_{min} as a function of (γ, R_{cut}). The best fit can be seen to be part of a long "valley", extending to lower values of γ and R_{cut}, approximately along the shown curve. Although there is a much greater deviation, there is also another local minimum for $\gamma \approx 2$. The values of the parameters obtained for the first and second minimums are displayed on the panel.

Therefore, when interpreted in terms of a simple model of UHECRs injection, the Pierre Auger Observatory data are best fitted by a very hard ($\gamma \lesssim 1$) injection spectrum and the flux is mainly limited by the maximum energy acquired by the events in the sources.

However, it is important to mention that the assumption that the sources

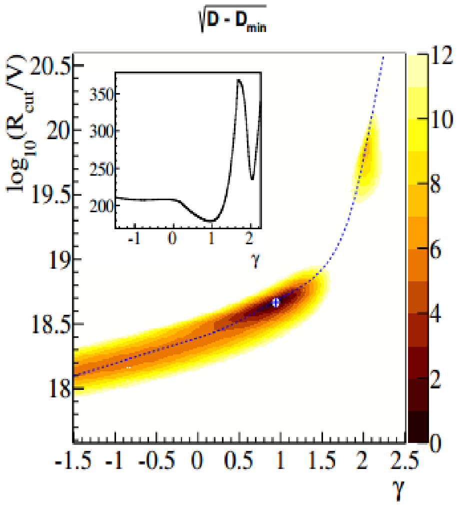

model SPG	best fit	2nd local min
J_0 [eV^{-1} Mpc^{-3} yr^{-1}]	7.17×10^{18}	4.53×10^{19}
γ	$0.94^{+0.09}_{-0.10}$	2.03
$\log_{10}(R_{\mathrm{cut}}/\mathrm{V})$	18.67 ± 0.03	19.84
p_{H}	$0.0^{+29.9}\%$	0.0%
p_{He}	$62.0^{+3.5}_{-22.2}\%$	0.0%
p_{N}	$37.2^{+4.2}_{-12.6}\%$	94.2%
p_{Fe}	$0.8^{+0.2}_{-0.3}\%$	5.8%
D/n	178.5/119	235.0/119
$D(J)$, $D(X_{\mathrm{max}})$	18.8, 159.8	14.5, 220.5
p	2.6%	5×10^{-4}

FIGURE 4.1: **Left:** deviation from D_{min} as a function of (γ, R_{cut}). The color diagram indicates the confidence levels: 1σ, 2σ, ... In detail the values of D along the dashed curve are shown. **Right:** the parameter values obtained for the first and second minimum. [Aab et al., 2016a].

of UHECRs are identical and uniformly distributed across the space contradicts the observed dipolar anisotropy previously described [Aab et al., 2015b],[Aab et al., 2014d]. Therefore, the inclusion of non-uniform distributions of sources in the simulations as well as information about events arrival direction at Earth is fundamental for the correct interpretation of the different measures performed by the Pierre Auger Collaboration. This way, we will present in the next sections our contributions to improve this analysis.

4.2 Dipolar anisotropies detected by the Pierre Auger Observatory for E > 8 EeV

As was previously seen in chapter 2, the Pierre Auger Collaboration has reported large scale anisotropies for energies above E > 8 EeV [Aab et al., 2015b, Souza de Oliveira, 2016] and this information was not included in the combined fit reported in [di Matteo, 2016]. In the following, aiming to include this result in the Pierre Auger data interpretation, we will describe our results about a fit of the large scale anisotropies detected by the Pierre Auger Observatory for E > 8 EeV.

We assume that the reason for the observed dipolar pattern in the arrival direction of the events detected by the Pierre Auger Collaboration is the non-homogeneous distribution of the local matter. This way, following the arguments presented in reference [Harari et al., 2013], we assume that the cosmic ray flux is a combination of an isotropic part resulted from the contributions of distant sources (homogeneous distributed) and an anisotropic contribution from local sources (non-homogeneous distributed). If the fraction of the flux coming from the isotropic sources is f and, assuming that the non-homogeneous source distribution is represented by the 2 $Micron$ $All - Sky$ $Redshift$ $Survey$ catalog (2MRS) [Erdogdu et al., 2006], the total flux of cosmic rays can be written as

$$\Phi(\hat{n}) = f\Phi_{isotropic}(\hat{n}) + (1-f)\Phi_{2MRS}(\hat{n}), \tag{4.2}$$

where $\Phi_{isotropic}(\hat{n})$ is the flux coming from the homogeneously distributed sources and $\Phi_{2MRS}(\hat{n})$ is the flux of events coming from 2MRs sources.

Figure 4.2 presents the celestial map of the 2MRS catalog sources smoothed by a gaussian filter of $\sigma = 60°$. We can see that there is a dipole in its mass distribution with a magnitude $D \simeq 0.24$ pointing in the direction $(l, b) = (251° \pm 12°, 37° \pm 10°)$ in galactic coordinates or $(\alpha, \delta) = (153°, -9°)$ in equatorial coordinates. Considering this dipolar amplitude D in the local matter distribution and equation (4.2), the dipolar amplitude in the arrival directions of cosmic rays with energy between E_1 and E_2 is given by:

$$\Delta_{CR}(E_1, E_2) = f(E_1, E_2, R)D(R), \tag{4.3}$$

where $f(E_1, E_2, R)$ is the fraction of cosmic rays with energies between E_1 and E_2 coming from distances smaller than R. This fraction can be evaluated by simulating the propagation of particles from their sources to Earth.

As an initial exercise, we computed the dipolar amplitude expected for protons and

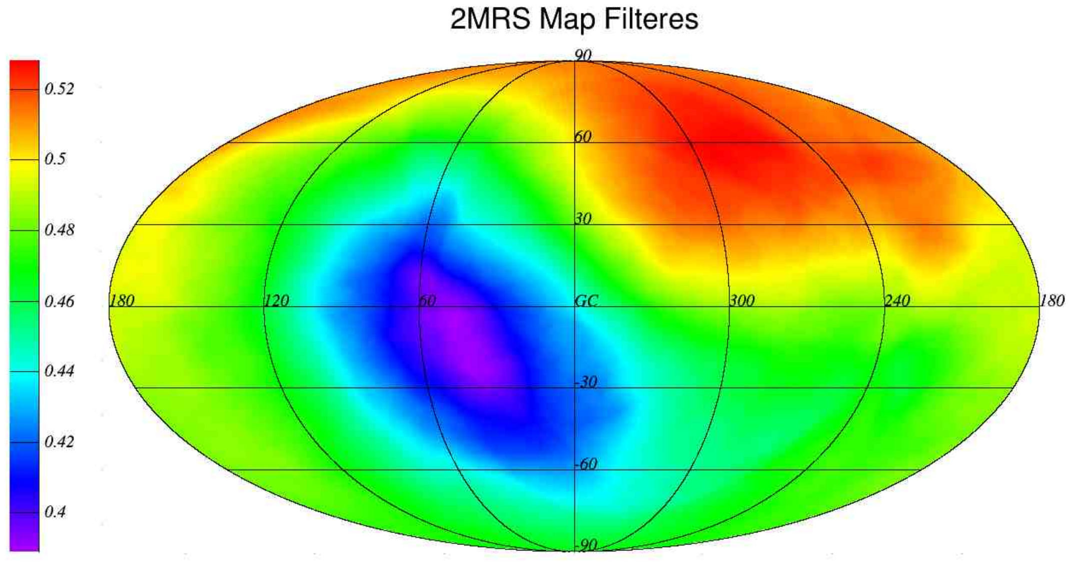

FIGURE 4.2: Maps of the distribution of matter calculated with the 2MRS catalog and smoothed in 60° .

iron for several energy bins in order to compare them with those reported in [Aab et al., 2015b]. For this, we have simulated one million of each particle with the CRPropa3 code [Alves Batista et al., 2016] [1] by assuming a power law spectrum with spectral index $\gamma = 2.2$, uniformly distributed sources up to 4000 Mpc and $R = 285$ Mpc. The reason for using this value of R is that the sources at distances larger than R are roughly uniformly distributed.

As illustration, figure 4.3 shows the number of protons and irons reaching the Earth as a function of the source distance for $E > 8$ EeV. We can see that the energy attenuation for iron particles is smaller than the energy attenuation for protons. As a consequence, the fraction of the flux coming from nearby sources is smaller for iron particles, producing a dipolar amplitude smaller than that in case of protons. Tables 4.1 and 4.2 present, for several energy bins, the fractions of the flux of proton and iron, respectively, coming from sources with distances $R < 285$ Mpc as well as the expected dipolar amplitudes.

[1]For more details about the CRPropa3 code, see Appendix B

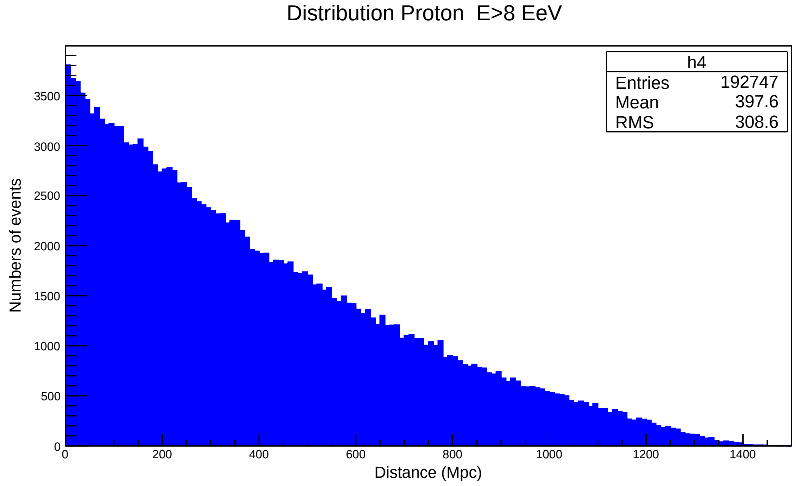

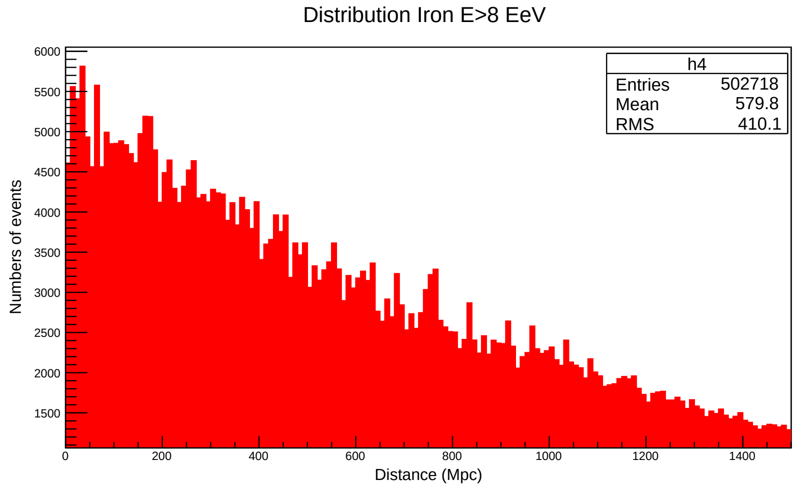

FIGURE 4.3: Distribution of proton (**Top**) and iron (**Bottom**) particles that arrive at Earth as a function of the source distance with energy $E > 8$ EeV.

Energy [EeV]	$f(E_1, E_2, R)$	Dipole CR - Δ_{CR}
$1 < E < 2$	0.131	0.031
$2 < E < 4$	0.178	0.043
$4 < E < 8$	0.220	0.053
$E > 8$	0.396	0.095

TABLE 4.1: Fraction of CR coming from distances smaller than R for different ranges of energy for proton. In the third column the expected dipole is calculated using equation (4.3).

The dipolar amplitude calculated as a function of energy for both primary particles is shown in figure 4.4. As previously mentioned the Pierre Auger Collaboration reported a dipole amplitude of 0.073 (7.3%) for energies above 8 EeV and of 0.027 (2.7%) for energies between 4 and 8 EeV while the dipolar amplitude obtained for

Energy [EeV]	$f(E_1, E_2, R)$	Dipole CR - Δ_{CR}
$1 < E < 2$	0.079	0.019
$2 < E < 4$	0.086	0.021
$4 < E < 8$	0.114	0.027
$E > 8$	0.266	0.064

TABLE 4.2: Fraction of CR coming from distances smaller than R for different ranges of energy for iron. In the third column the expected dipole is calculated using equation (4.3).

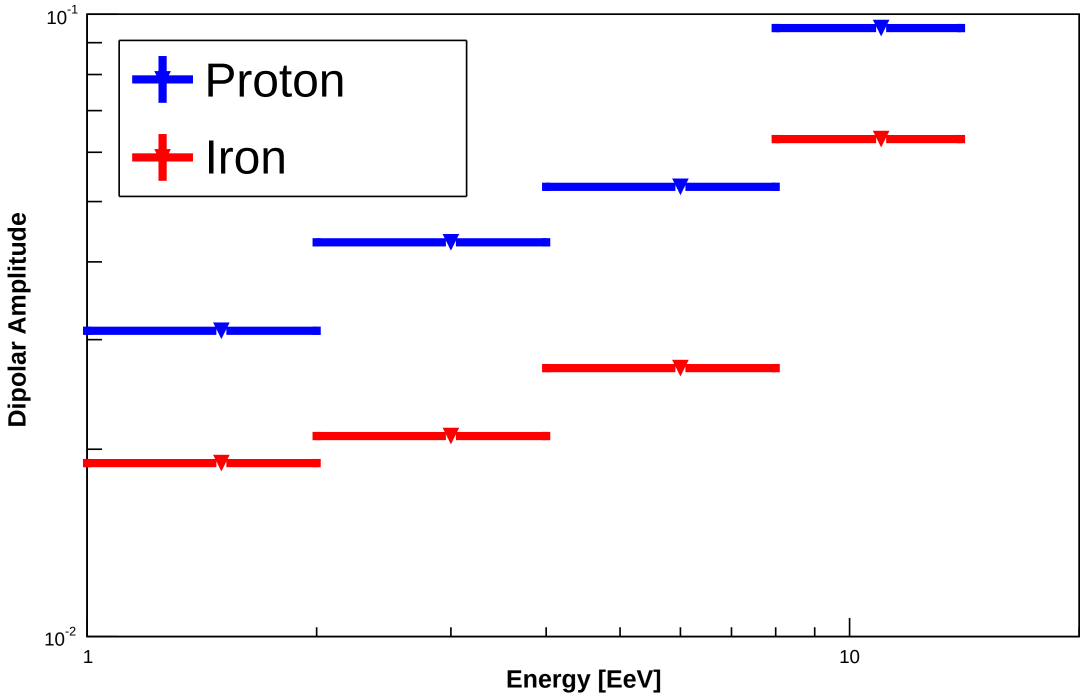

FIGURE 4.4: Expected amplitude of the dipolar component of the cosmic ray flux as a function of the energy for proton primaries (solid blue line) and for iron primaries (solid red line).

us is 0.095 (9.5%) and 0.053 (5.3%) respectively.

Besides the presence of additional nuclei, a possible reason for these differences is that we did not use the intergalactic and galactic magnetic fields along the particles propagation. In the following, we will improve the analysis to infer the sources characteristics by considering also the galactic magnetic field and an extension the anisotropies searches up to $\ell = 64$, by using the measures of the Angular power spectrum reported in [Souza de Oliveira, 2016].

4.3 Fit of the Angular Power Spectrum measured by the Pierre Auger Collaboration for E > 8 EeV

In this section, we attempt to fit the Angular power spectrum reported in [Souza de Oliveira, 2016] aiming to infer characteristics of the cosmic ray sources. For this, we have used a very simple model that assumes that the cosmic ray sources up to 285 Mpc are those from the 2MRS catalog and homogeneously distributed for distances $R > 285$ Mpc, characterized by the emission of Hydrogen (^{1}H), Helium (^{4}He), Nitrogen (^{14}N), and Iron (^{56}Fe), with an emission spectrum having a suppression factor dependent on the R_{cut} rigidity of the particles, given by equation (4.1). The free parameters of the fit are: the injection normalization factor of the J_o, the injection spectral index γ, the cut-off rigidity R_{cut} and the fractions of the elements in the sources, (three free parameters: a_H, a_{He}, a_N, since the fourth is subject to the bond $a_H + a_{He} + a_N + a_{Fe} = 1$).

The simulations are performed using the CRPropa3 code including the galactic magnetic field parametrized by the Janson-Farrar model - JF12, described in section 2.3.7. We have divided the simulations in 2 parts: a) Propagation of particles from 2MRS catalog to Earth and b) Propagation of particles from uniformly distributed sources to Earth.

a) Propagation of particles from 2MRS catalog to Earth: since we do not consider the inter-galatic magnetic field, particles move in a straight line from their sources until hit the observer's surface. After hit the observer, the particle is subject to deflections in the galactic magnetic field, using the magnetic lens method [Bretz et al., 2014]. An important issue of all codes that simulate particle propagation through universe is that the Earth's size is too small in comparison with the volume of the universe. In order to solve this issue, we considered as observer an sphere with a radius of 10 kpc, and to increase the speed of the simulation all the particles are emitted by a source within an angle θ, defined by the distance between the source and the Earth and the observer radius. After the sources are drawn from the catalog, we randomly assign it a weight that $\propto r^{-2}$, where r is the source distance. Figure 4.5 presents an illustration of such emission.

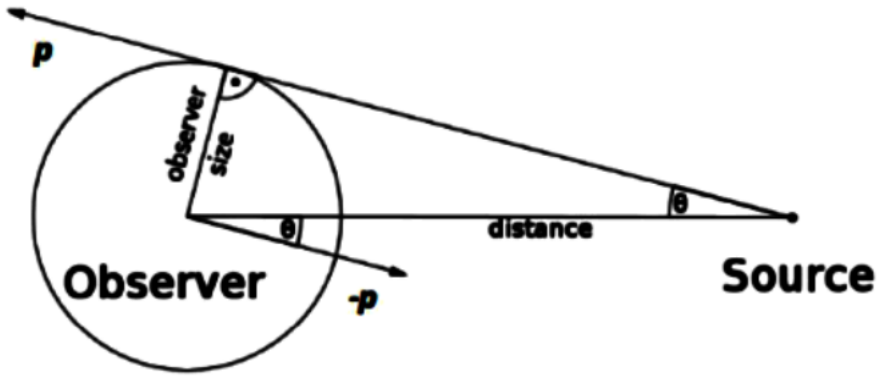

FIGURE 4.5: Representation of uniform random emission inside a cone.

100,000 particles of each nucleus are simulated with energy spectrum flat in $\log E$ (dN/dE $= kE^{-1}$). When they hit the observer, a weight $w = E^{1-\gamma}$ is assigned to it before they pass by the magnetic lens in order to emulate the emission energy spectrum $dN/dE \sim E^{-\gamma}$ at source. For each nucleus and each pair (γ, R_{cut}), a celestial flux map is produced and saved to posterior use. For illustration, figure 4.6 presents the flux map observed at Earth for each nucleus with $\gamma = 1$ and $\log_{10}(R_{cut}/V) = 20.3$.

b) Propagation of particles from uniformly distributed sources to Earth: although the background isotropic map consists of a very simple map with all pixels set to 1, it is necessary to simulate events from uniformly distributed sources because this map must be properly added to the flux map of events coming from the 2MRS sources. The total flux is given by equation (4.2). The fraction f of isotropic events that should be used to complete the catalog depends on γ, E_{cut} and abundances of four nuclei. Let N_i be the number of events that arrive at Earth in a given energy range resulted from the injection of nucleus i at sources. We can write N_i in the following way

$$N_i = N_{i<} + N_{i>}, \tag{4.4}$$

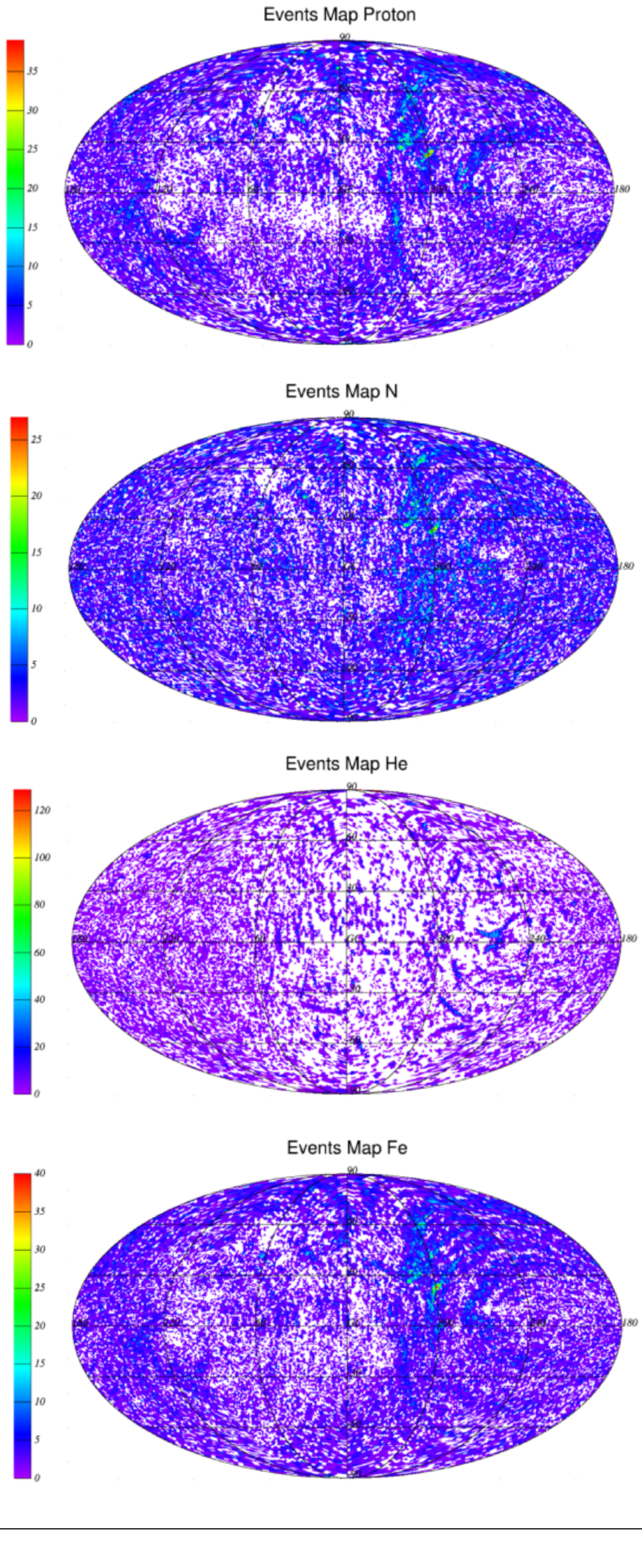

FIGURE 4.6: Flux map observed at Earth for each nucleus with $\gamma = 1$ and $\log_{10}(R_{cut}/V) = 20.3$.

where $N_{i<}$ is the number of particles coming from sources whose distance is smaller than 285 Mpc and $N_{i>}$ is the number of particles coming from sources whose distance is larger than 285 Mpc. Thus

$$\begin{aligned} N_H &= N_{H<} + N_{H>} \\ N_{He} &= N_{He<} + N_{He>} \\ N_N &= N_{N<} + N_{N>} \\ N_{Fe} &= N_{Fe<} + N_{Fe>}. \end{aligned} \tag{4.5}$$

The fraction of particles that arrive at Earth coming from sources whose distance are smaller than 285 Mpc for each nucleus is

$$f_i = \frac{N_{i<}}{N_i}. \tag{4.6}$$

The fraction of flux coming from distances smaller than 285 Mpc considering all nuclei is given by

$$f = \frac{N_{H<} + N_{He<} + N_{Ni<} + N_{Fe<}}{N_H + N_{He} + N_N + N_{Fe}}. \tag{4.7}$$

Using equation (4.6) for each nucleus it is possible to replace the $N_{i<}$ by $f \times N_i$ so that

$$f = \frac{N_H \times f_H + N_{He} \times f_{He} + N_N \times f_N + N_{Fe} \times f_{Fe}}{N_H + N_{He} + N_N + N_{Fe}}. \tag{4.8}$$

However, this equation assumes that the abundances of each nucleus at the sources are the same. In order to consider different abundances, we need to replace:

$$N_i \rightarrow N_i^*$$

with

$$N_i^* = N_i \times a_i,$$

where N_i^* is the number of particles that reached the Earth multiplied by the abundance a_i of each nucleus at the sources. Therefore the fraction of the flux coming from distances less than 285 Mpc that should be used in equation (4.2) is

$$f = \frac{a_H \times N_H \times f_p + a_{He} \times N_{He} \times f_{He} + a_N \times N_N \times f_N + a_{Fe} \times N_{Fe} \times f_{Fe}}{a_H \times N_H + a_{He} \times N_{He} + a_N \times N_N + a_{Fe} \times N_{Fe}}. \quad (4.9)$$

The map of the flux coming from 2MRS sources $\Phi_{2MRS}(\hat{n})$ including the contribution of all nuclei is given by

$$\Phi_{2MRS}(\hat{n}) = \sum_{i=1}^{i=4} a_i \times (1 - f_i) \times N_i \times \Phi_{i,2MRS}(\hat{n}), \quad (4.10)$$

where $N_i = 100,000$ is the number of simulated particles that reached Earth and $\Phi_{i,2MRS}$ is the map of the flux of events for each nucleus coming from 2MRS sources after passing by the galactic magnetic lens. For each pair (γ, R_{cut}), 500 random combinations of the abundances a_i at the sources were generated. For illustration, figure 4.7 shows the total map $\Phi(\hat{n})$ for $\gamma = 1$, $\log_{10}(R_{cut}/V) = 20.3$ and given combination of abundances.

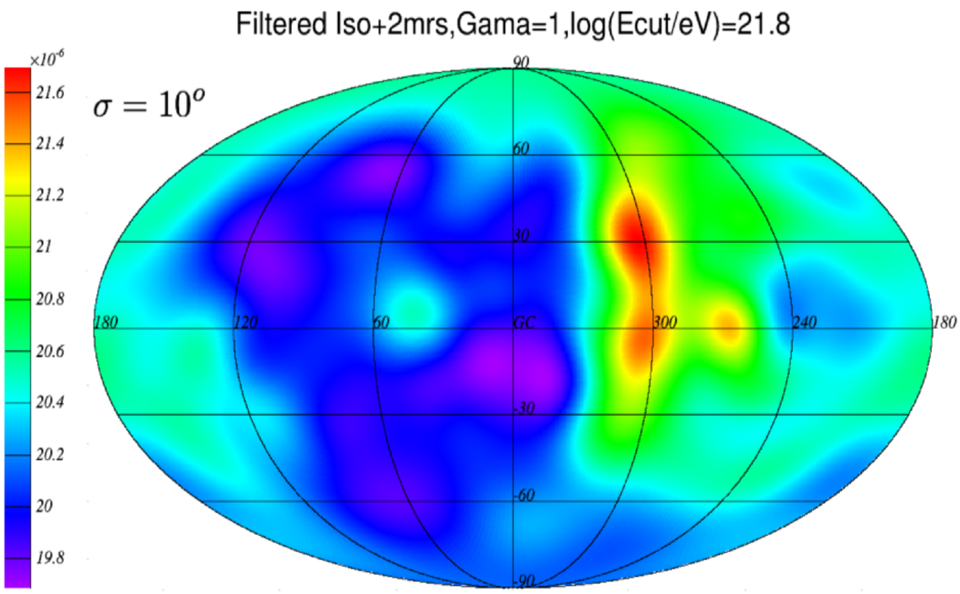

FIGURE 4.7: Total map of the flux: Isotropic background + 2MRS events.

Finally, after expanding the map of the flux $\Phi(\hat{n})$ in spherical harmonics by using the Healpix package [Gorski et al., 2005] and computing the angular power spectrum, given by equation (2.19), a χ^2 is evaluated in comparison with the measured power spectrum (right panel of figure 2.13) in order to search the set of parameters that best fit the data. The Minimum values of $\log(\chi^2)$ as a function of $(\gamma, \log(R_{cut}/V))$ are shown in figure 4.8. The white mark is the position of the best fit, $\gamma = 1.95$ and $R_{cut} = 10^{19}$. The corresponding abundances of the best fit are $a_H = 27\%$, $a_{He} = 13\%$, $a_N = 7\%$ and $a_{Fe} = 53\%$.

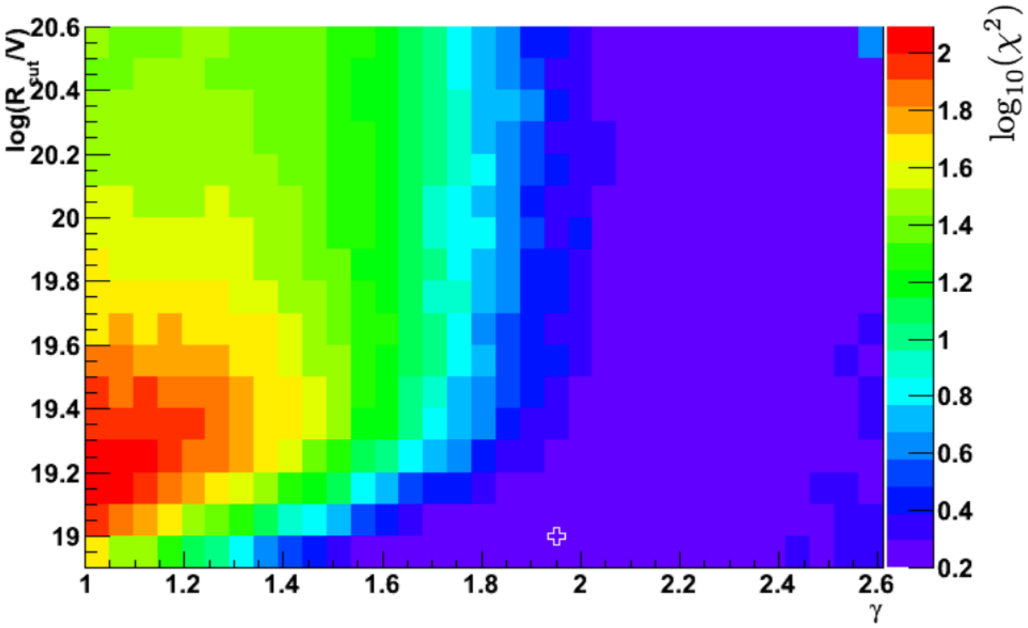

FIGURE 4.8: Minimum values of $\log(\chi^2)$ as a function of $(\gamma, \log(R_{cut}/V))$. The white mark is the position of the best fit, $\gamma = 1.95$ and $R_{cut} = 10^{19}$.

Figure 4.9 shows the angular power spectrum corresponding to the best fit. The black dots corresponds to the Pierre Auger data while red color corresponds to the best fit scenario. It is clear that simulations reproduced very well the data including the dipole $\ell = 1$.

The difference between this result and the one presented in [di Matteo, 2016] shows that one only analysis combining the data of energy spectrum, composition and arrival direction should be produced. Our group is working on this analysis and new results will be produced soon.

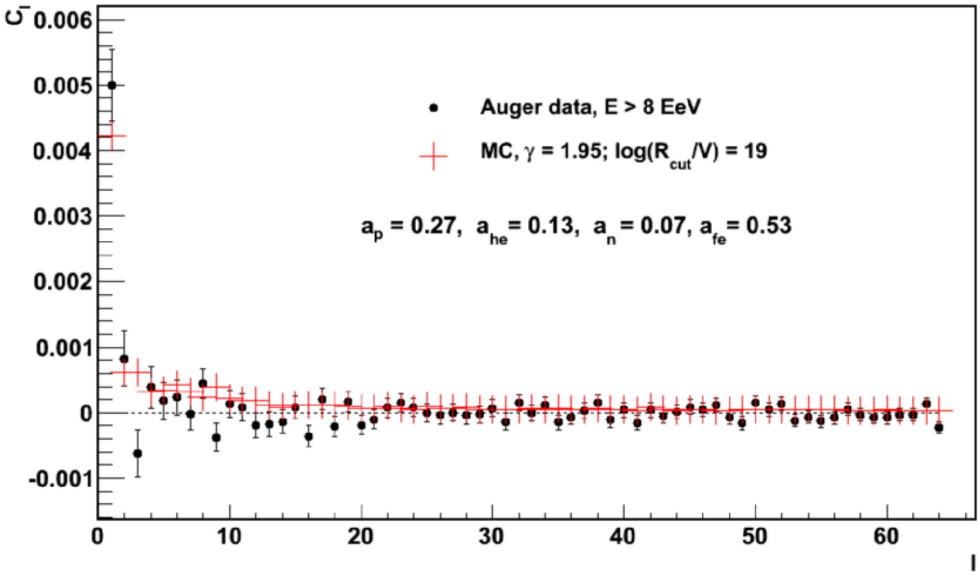

FIGURE 4.9: The power spectrum as a function of the angular scale for $E > 8$ EeV.

4.4 Effect of the Lorentz invariance violations on the large scale anisotropy

Quantum mechanics and general relativity are theories that describe very well our universe and in small and large scales, respectively. However, the correct way to unify these theories is still unknown. Quantum gravity is an excellent candidate to explain this unification, predicting that space-time is subject to quantum fluctuations and the symmetries present in the world in which we live emerge in the semi-classical limit. The Lorentz Invariance (LI) is one of these symmetries and therefore is not guaranteed to be exact, i.e., possible Lorentz Invariance Violation (LIV) can be observed for a higher energy scale.

Being the most energetic particles in the universe, the ultra-high energy cosmic rays are a natural tool to test LIV or put limits on its parameters. In particular, the GZK prediction has been recognized for some time as an interesting possibility for studying the violation of Lorentz invariance, given the low energy of the background radiation photons. Thus, after the indubitable confirmation of a suppression in the energy spectrum for energies $\sim 5 \times 10^{19}$ eV by the Pierre Auger Collaboration [Abraham et al., 2010], limits on the parameters of LIV theories were obtained. However, as previously commented in section 4.1, the combined fit of the spectrum and composition data as measured by the Pierre Auger Collaboration [di Matteo, 2016] suggests that the suppression observed in the spectrum is due to the maximum injection energy of particles at sources rather than to interactions in the background radiation. This result made the astrophysics community returned again to consider the possibility of LIV by using UHECRs data. This is the motivation to study the impact of LIV in the interpretation of Auger data whose results will be describe in the following sections.

Such LIV effects may be introduced by changes in dispersion relation as follows

$$E_i^2 - p_i^2 = m_i^2 \rightarrow \mu_i^2 \left(E, p, M_P\right) \approx m_i^2 + \frac{f_i}{M_P^n} E_i^{2+n}, \tag{4.11}$$

where p is the particle three-dmensional momentum, μ is a function of the momentum and energy, $M_P \approx 1.2 \times 10^{28}$ eV is the Planck mass, for which deviations of quantum gravity becomes relevant, andf_i parametrizes the magnitude of LIV for particle i. Thus, it can be noticed that the term of correction in negligible, even for $E \approx 10^{20}$ eV. Nevertheless, as soon as $p \geq \left(m_i^2 M_P^n / |f_i|\right)^{1/(2+n)}$, important effects can arise [Aloisio et al., 2000]. In the case that we will investigate in this thesis, the energy threshold for photo-pion production due to interaction with CMB photons is modified as follows:

$$E_{\mathrm{GZK}} \approx \frac{m_p m_\pi}{2\omega_\gamma} \rightarrow E_{\mathrm{GZK}} \approx \frac{\mu\left(E_p, p_p, m_p, M_P\right) \mu\left(E_\pi, p_\pi, m_\pi, M_P\right)}{2\omega_\gamma}, \tag{4.12}$$

with ω_γ representing the CMB photon energy.

For somes values of f_i, this equation has no more real solution for $E_p = E_{GZK}$ in parameters space $(E_p, p_p, m_p, E_\pi, p_\pi, m_\pi, \omega_\gamma, M_p)$. Thus, the photo-production reaction shall be kinematically forbidden and protons would move freely throughout the universe. A similar result can be obtained if we consider heavier nuclei rather than protons. This would bring profound changes on the the interpretation of the energy spectrum, mass composition and arrival directions of UHECRs on Earth. In section 4.5 we will present results of the fit of the Auger energy spectrum and X_{max} data by using a very simple astrophysical model similar to the one used in [Aab et al., 2016a], added to a extreme LIV scenario while in section 4.6 we will present a fit of the dipolar amplitudes measured by the Pierre Auger Collaboration considering a LIV scenario.

4.5 A combined fit of spectrum and composition Auger data considering a very simple case of Lorentz Invariance Violation along the cosmic ray propagation

In this section we describe the analysis performed by our group to fit the Auger energy spectrum and X_{max} data by using a LIV scenario. For this, we consider a very simple astrophysical model similar to the one used in [Aab et al., 2016a], described in section 4.1. However, instead of using the usual processes of energy losses, we consider a extreme LIV scenario, i.e., we neglected all interactions with background photons, taking into account only energy losses due to the expansion of the universe.

We assume uniform distribution of identical sources within a comoving volume of $(4000\ \text{Mpc})^3$, with no source evolution. Four types of nuclei are injected at the sources (H, He, N and Fe) with energies ranging from 10^{17} eV to 10^{22} eV following the power-law injection spectrum with rigidity-dependent broken exponential cutoff given by equation 4.1. The simulated data sample was obtained by using the CR-Propa3 code [Alves Batista et al., 2016]. In order to reproduce a scenario where LIV occurs, we neglected all interactions with background photons, only accounting for energy losses due to the expansion of the universe. It is also worth mentioning that the extragalactic magnetic field was not included in this simulation.

We simulated the propagation of 10^5 particles of each type of nucleus from the sources to the Earth with injected energy at source following a flat distribution in $\log(E_{\rm inj}/{\rm eV})$, i.e., $dN/dE \propto E$, therefore the spectrum (4.1) was obtained by assigning a weight $\propto E_{\rm inj}^{1-\gamma}$ to each nucleus at Earth. These values were used to build the energy spectrum for each type of injected nucleus. The sum of these histograms (using the abundances a_i as weights) provides the energy spectrum that is used to evaluate the χ^2 through a comparison with the Auger data. The fit range in this case was set to $18.7 \leq \log(E/{\rm eV}) \leq 20.2$.

The values of $X_{\rm max}$ that these simulated cosmic rays would produce in the atmosphere were evaluated using the Gumbel parametrization [De Domenico et al., 2013], assuming the EPOS-LHC interaction model [Pierog et al., 2015]. These values were used to build $X_{\rm max}$ distributions as a function of the detected energy for each type of injected nucleus. By adding these histograms, using the abundances a_i as weights, one is able to obtain the $< X_{\rm max} >$ and $\sigma_{X_{\rm max}}$ for each energy bin and build a χ^2 to be minimized in comparison with the Auger data. For the $X_{\rm max}$ and $\sigma_{X_{\rm max}}$ distributions the fit was performed in the range $18.7 \leq \log(E/{\rm eV}) \leq 20$.

The data points used in the fit of the $< X_{\rm max} >$ and $\sigma_{X_{\rm max}}$ were taken from [Porcelli, 2015], and for the spectrum we used the data from [Schulz, 2013]. Using these data and the simulated histograms previously described, one is able to build a combined χ^2 and optimize the parameters of the model.

The parameter space was divided in 91 bins of γ, ranging from -1.5 to 3.0, and 31 bins of $\log(R_{\rm cut}/{\rm V})$, from 17.6 to 20.6. For each pair (γ,$\log(R_{\rm cut}/{\rm V})$) the parameters J_0 and a_i were fit using the Minuit package. The minimum χ^2 for each bin of $(\gamma, \log(R_{\rm cut}/{\rm V}))$ is shown in figure 4.10. In this case, $\gamma = 2.5$ and $R_{\rm cut} = 10^{18.5}$ V provide the best fit of the model to the Auger data, and the corresponding abundances at the source are $a_{\rm H} = 42.0\%$, $a_{\rm He} = 44.0\%$, $a_{\rm N} = 14.0\%$ and $a_{\rm Fe} = 0.06\%$.

The spectrum fit and the fits for the $< X_{\rm max} >$ and $\sigma_{X_{\rm max}}$ obtained are shown in figures 4.11 and 4.12. It is important to emphasize that these results are very preliminary and that the position of the minimum as well as the nuclei abundances

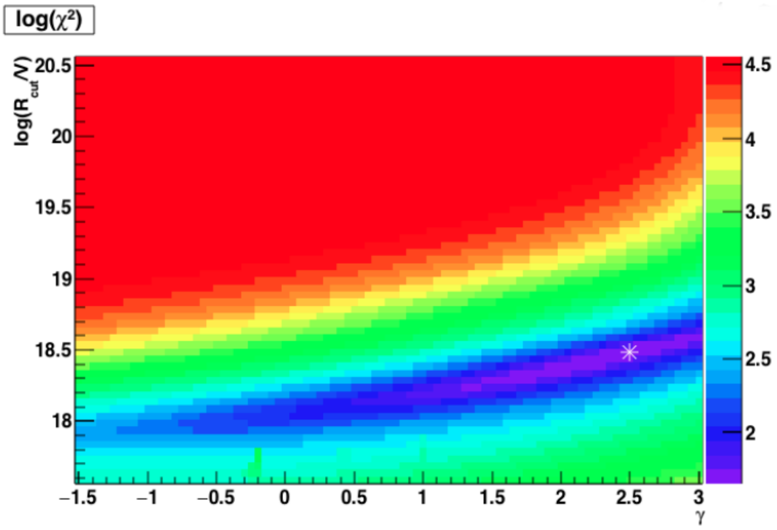

FIGURE 4.10: Minimum values of $\log(\chi^2)$ as a function of $(\gamma, \log(R_{\text{cut}}/\text{V}))$ obtained using the Minuit. The white star marks the position of the best fit, $\gamma = 2.5$ and $R_{\text{cut}} = 10^{18.5}$ V.

at the sources are sensitive to the minimization procedure. Therefore, we continue investigating these dependencies.

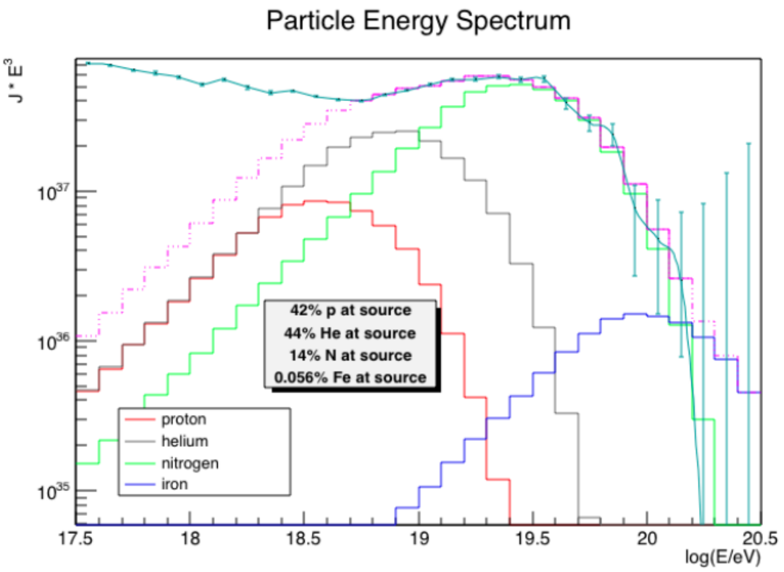

FIGURE 4.11: Spectrum fit ($18.7 \leq \log(E/\text{eV}) \leq 20.2$) for H (42.0%), He (44.0%), N (14.0%) and Fe (0.06%) injected at the sources with $\gamma = 2.5$ and $R_{\text{cut}} = 10^{18.5}$ V.

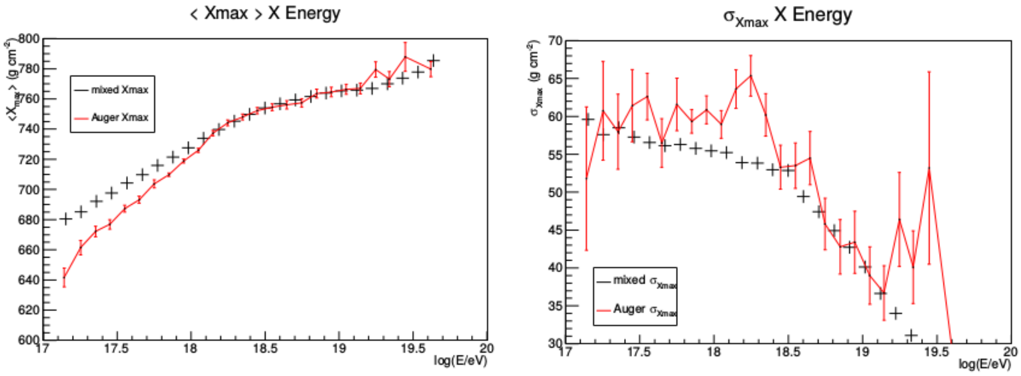

FIGURE 4.12: Fits of $< X_{\max} >$ (left) and $\sigma_{X_{\max}}$ (right) as a function of energy in the range $18.7 \leq \log(E/\mathrm{eV}) \leq 20$ for H (42.0%), He (44.0%), N (14.0%) and Fe (0.06%) injected at the sources with $\gamma = 2.5$ and $R_{\rm cut} = 10^{18.5}$ V.

4.6 Fit of dipolar measurements reported by Pierre Auger Collaboration using LIV scenario

As mentioned before, the Pierre Auger Collaboration reported dipolar amplitudes of 7.3% for energies above 8 EeV and 2.7% for $4 \leq E/EeV \leq 8$ [Aab et al., 2015b]. In this section we search for the injected UHECR composition at sources that best reproduce the Auger measurements. For this, we consider the astrophysical scenario assumed in section 4.5 with $\gamma = 2.5$ and $R_{\rm cut} = 10^{18.5}$ V, as obtained before.

According to section 4.2, for each combination of abundances at source (a_H, a_{He}, a_N and a_{Fe}), the resulting dipolar amplitude, for each bin, is obtained by

$$\Delta = D \times \frac{a_H \times N_H \times f_p + a_{He} \times N_{He} \times f_{He} + a_N \times N_N \times f_N + a_{Fe} \times N_{Fe} \times f_{Fe}}{a_H \times N_H + a_{He} \times N_{He} + a_N \times N_N + a_{Fe} \times N_{Fe}}, \tag{4.13}$$

where $D \sim 0.24$ is the dipolar component from our local matter distribution, f_i are the fractions of the flux of each nucleus coming from sources with distance smaller than 285 Mpc and a_i, the abundance of each nucleus at source, are the parameters that we want to determine.

To calculate the fraction of CRs f_i of each nucleus coming from distances < 285 Mpc, we generated 1 million events from uniformly distributed sources up to 4.000 Mpc with injection power law spectrum with maximum rigidity of $R_{cut} = 10^{18.5}$ V and spectral index of $\gamma = 2.5$. Figure 4.13 shows the distribution of particles simulated with CRPropa3 code that arrived at Earth as a function of distance. Since the maximum rigidity at the sources is very low, $R_{cut} = 10^{18.5} \sim 3 \times 10^{18}$, there is no contribution of protons for both energy bins and of Helium for $E > 8$ EeV.

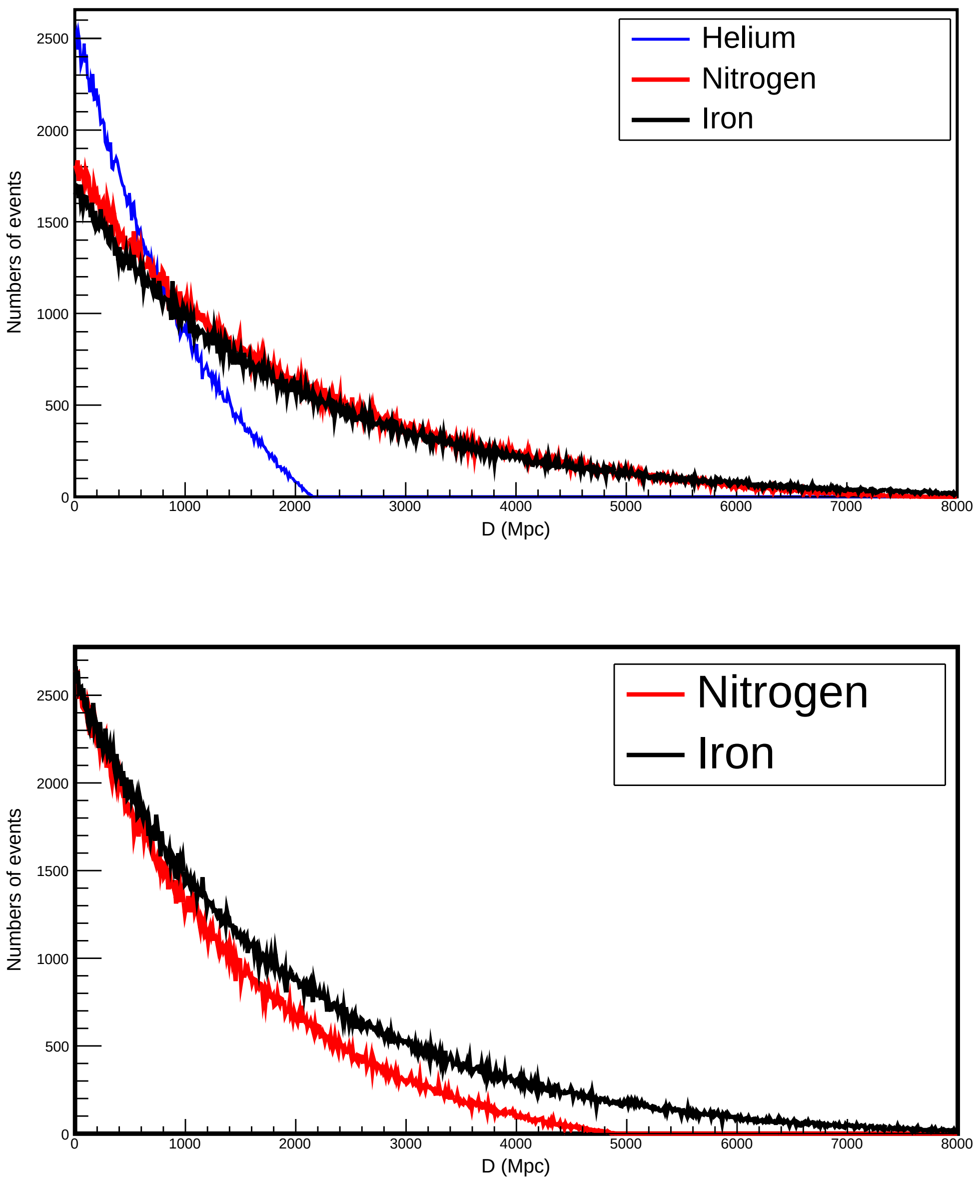

FIGURE 4.13: Number of particles that arrive at Earth as a function of the distance in two energy bins: 4 EeV $\leq$ E $\leq$ 8 EeV (**Top**), and $E > 8$ EeV (**Bottom**).

The resulting fractions of the flux coming from sources at distances smaller than 285 Mpc are presented in table 4.3.

	$4 < E < 8$ [EeV]	$E > 8$[EeV]
Proton	-	-
Helium	0.326	-
Nitrogen	0.118	0.194
Iron	0.105	0.162

TABLE 4.3: Fraction of particles f coming from $D < 285$ Mpc.

We randomly generated 500 sets of abundances at sources a_i and performed a χ^2 analysis looking for the best fit between the dipolar amplitude given by equation (4.13) and the dipolar measurements reported by the Pierre Auger Collaboration. The best values of the abundances obtained are: $a_H = 0.3\%$, $a_{He} = 1.6\%$, $a_N = 98\%$, $a_{Fe} = 0.002\%$, corresponding to a dipolar amplitude of 0.027 for $4 \leq E/EeV \leq 8$ and of 0.05 for $E > 8$ EeV.

Chapter 5

Final Remarks and Perspectives

The phenomenology of UHECRs is a field of research that requires knowledge of many branches of physics, including astrophysics, cosmology, nuclear and particle physics. There are large uncertainties in many aspects of these phenomena: particles of unknown chemical composition are accelerated through unknown mechanisms by astrophysical objects of uncertain nature, achieving an unknown energy spectrum of injection. These particles travel through intergalactic space, interacting with the background photons and can be deflected by galactic and intergalactic magnetic fields.

In this thesis we have performed phenomenological analyzes aiming to infer characteristics of the cosmic ray sources such as the emission energy spectrum and composition. These analyzes contribute not only for the better understanding of the universe, regarding the identity of astrophysical sources and the mechanisms of production, acceleration and propagation in the interstellar medium, but also for the study of fundamental physics in energies that can not be reached at particle accelerators.

The main motivation for this work was to improve the combined fit analysis reported by the Pierre Auger Collaboration using energy spectrum and composition data. This analysis tried to infer characteristics of the sources using a simple model of identical sources homogeneously distributed characterized by the emission of Hydrogen (^{1}H), Helium (^{4}He), Nitrogen (^{14}N), and Iron (^{56}Fe), with an emission spectrum having a suppression factor dependent on the rigidity R_{cut} of the particles. However, as it was mentioned in the thesis, the assumption that the sources of UHECRs are identical and uniformly distributed through the space contradicts the observed dipolar anisotropy reported by the Pierre Auger Collaboration.

Therefore, we performed a fit of the angular power spectrum measured by the Pierre Auger Collaboration by assuming that the cosmic ray flux is a combination of an isotropic part resulted from the contributions of distant sources (homogeneous distributed) and an anisotropic contribution from local sources (non-homogeneous distributed), represented by the 2MRS catalog. The parameters obtained that best fit the data are $\gamma = 1.95$, $\log(R_{cut}/V) = 19$ and abundances of the nucleus at sources $a_H = 27\%,\ a_{He} = 13\%,\ a_N = 7\%,\ a_{Fe} = 53\%$. The differences between these results and the one reported by the Pierre Auger Collaboration ($\gamma = 0.94$, $\log(R_{cut}/V) = 18.67,\ a_H = 0.0,\ a_{He} = 62\%,\ a_N = 37.2\%,\ a_{Fe} = 0.8\%$.) show that the informations about the arrival direction of the events at Earth should be include in the fit, in combination with informations about the energy spectrum and composition.

Also, the best fit parameters reported by Pierre Auger Collaboration suggest that the suppression observed in the spectrum is due to the maximum injection energy of particles at sources rather than to interactions in the background radiation. This motivated us to study the impact of LIV in the interpretation of Auger data since for some values of LIV parameters the photo-pion production could be kinematically forbidden. Thus, we first fit the Auger energy spectrum and composition data by considering a very simple astrophysical model similar to the one used in the Auger combined fit added to a extreme LIV scenario, i.e., neglecting all interactions with background photons, taking into account only energy losses due to the expansion of the universe. We found that, in this maximal LIV scenario, the parameters that best fit the data are $\gamma = 2.5$, $\log(R_{cut}/V) = 18.5$, $a_H = 42\%,\ a_{He} = 44\%,\ a_N = 14\%,\ a_{Fe} = 0.06\%$. Finally, under the same extreme LIV scenario and assuming the same γ and $\log(R_{cut}/V)$, we also searched for the abundances at source that best fit the Auger dipolar measurements for $4 \leq E/EeV \leq 8$ and $E > 8$ EeV. The obtained results are $a_H = 0.3\%$, $a_{He} = 1.6\%$, $a_N = 98\%$, $a_{Fe} = 0.002\%$ I intend to improve and extend this work in my Ph.D. thesis with the following topics:

- Perform a global fit of the data including informations about the energy spectrum, chemical composition and angular power spectrum;
- Perform a global fit of the data, under the assumption of LIV scenario, including informations about the energy spectrum, chemical composition and angular power spectrum.

The analyzes described in this work were reported in the following internal notes of the Pierre Auger Collaboration:

1. GAP 2017-012, R. A. Batista, F. Catalani, E. Alves Júnion, R. M. de Almeida, J. R. T. de Mello Neto, J. S. de Oliveira, U. Giaccari, B. Lago, R. G. Lang, C. Todero, and C. A. V. Ventura , *A combined fit of spectrum and composition Auger data considering a very simple case of Lorentz Invariance Violation along the cosmic ray propagation* [R. A. Batista et al., 2017].
2. GAP 2017-016, R. A. Batista, F. Catalani, E. Alves Júnion, R. M. de Almeida, J. R. T. de Mello Neto, J. S. de Oliveira, U. Giaccari, B. Lago, R. G. Lang, C. Todero, and C. A. V. Ventura , *Phenomenological analysis of the large scale anisotropies measured by the Pierre Auger Collaboration considering Lorentz Invariance Violation* [R. M. de Almeida et al., 2017].

Bibliography

A. van Vliet, A., Kampert, K.-H., Kulbartz, J., Maccione, L., Nierstenhoefer, N., Schiffer, P., and Sigl, G. (2013). CRPropa 2.0. Public Software to Model Extra-galactic Propagation of Ultra-High Energy Nuclei. In *European Physical Journal Web of Conferences*, volume 52 of *European Physical Journal Web of Conferences*, page 06006. 100

Aab, A. et al. (2013). The Pierre Auger Observatory: Contributions to the 33rd International Cosmic Ray Conference (ICRC 2013). In *Proceedings, 33rd International Cosmic Ray Conference (ICRC2013): Rio de Janeiro, Brazil*. 30, 47, 57

Aab, A. et al. (2014a). A search for point sources of EeV photons. *The Astrophysical Journal*, 789(2):160. 29

Aab, A. et al. (2014b). Depth of maximum of air-shower profiles at the pierre auger observatory. i. measurements at energies above $10^{17.8}$ eV. *Physical Review D*, 90:122005. 28

Aab, A. et al. (2014c). Reconstruction of inclined air showers detected with the Pierre Auger Observatory. *Journal of Cosmology and Astroparticle Physics*, 1408(08):019. 55, 56

Aab, A. et al. (2014d). Searches for Large-Scale Anisotropy in the Arrival Directions of Cosmic Rays Detected above Energy of 10^{19} eV at the Pierre Auger Observatory and the Telescope Array. *The Astrophysical Journal*, 794(2):172. 61

Aab, A. et al. (2015a). Improved limit to the diffuse flux of ultrahigh energy neutrinos from the Pierre Auger Observatory. *Physical Review*, D91(9):092008. 29

Aab, A. et al. (2015b). Large Scale Distribution of Ultra High Energy Cosmic Rays Detected at the Pierre Auger Observatory With Zenith Angles up to 80°. *The Astrophysical Journal*, 802(2):111. 36, 37, 38, 61, 63, 77

Aab, A. et al. (2015c). Measurement of the cosmic ray spectrum above 4×10^{18} eV using inclined events detected with the Pierre Auger Observatory. *Journal of Cosmology and Astroparticle Physics*, 1508:049. 58

Aab, A. et al. (2015d). Searches for Anisotropies in the Arrival Directions of the Highest Energy Cosmic Rays Detected by the Pierre Auger Observatory. *The Astrophysical Journal*, 804(1):15. 33

Aab, A. et al. (2015e). The Pierre Auger Cosmic Ray Observatory. *Nuclear Instruments and Methods in Physics Research A*, A798:172–213. 40, 42, 43, 44, 48, 50

Aab, A. et al. (2015f). The Pierre Auger Observatory: Contributions to the 34th International Cosmic Ray Conference (ICRC 2015). 25

Aab, A. et al. (2016a). Combined fit of spectrum and composition data as measured by the Pierre Auger Observatory. *Journal of Cosmology and Astroparticle Physics*. 61, 74

Aab, A. et al. (2016b). The Pierre Auger Observatory Upgrade - Preliminary Design Report. *ArXiv e-prints*. 31, 41, 49, 51, 54

Abbasi, R. U. et al. (2008). First observation of the Greisen-Zatsepin-Kuzmin suppression. *Physical Review Letters*, 100(10):101101. 16, 24

Abraham, J., Abreu, P., Aglietta, M., Ahn, E. J., Allard, D., Allen, J., Alvarez-Muñiz, J., Ambrosio, M., Anchordoqui, L., Andringa, S., and et al. (2010). Measurement of the energy spectrum of cosmic rays above 10^{18} eV using the Pierre Auger Observatory. *Physics Letters B*, 685:239–246. 73

Abraham, J. et al. (2007). Correlation of the highest energy cosmic rays with nearby extragalactic objects. *Science, American Association for the Advancement of Science*, 318:938–943. 12, 33

Abraham, J. et al. (2008). Observation of the suppression of the flux of cosmic rays above 4×10^{19}eV. *Physical Review Letters*, 101:061101. 24

Abraham, J. et al. (2009). Calibration and Monitoring of the Pierre Auger Observatory. In *31st International Cosmic Ray Conference (ICRC 2009): Lodz, Poland*. 45

Abraham, J. et al. (2010). Trigger and aperture of the surface detector array of the Pierre Auger Observatory. *Nuclear Instruments and Methods in Physics Research Section A: Accelerators, Spectrometers, Detectors and Associated Equipment*, A613:29–39. 49, 51, 52

Abreu, P. et al. (2011). The Pierre Auger Observatory I: The Cosmic Ray Energy Spectrum and Related Measurements. In *Proceedings, 32nd International Cosmic Ray Conference (ICRC 2011): Beijing, China*. 54

Achterberg, A., Gallant, Y. A., Kirk, J. G., and Guthmann, A. W. (2001). Particle acceleration by ultrarelativistic shocks: theory and simulations. *Monthly Notices of the Royal Astronomical Society*, 328:393–408. 9

Ahlers, M., Anchordoqui, L. A., Gonzalez-Garcia, M. C., Halzen, F., and Sarkar, S. (2010). GZK Neutrinos after the Fermi-LAT Diffuse Photon Flux Measurement. *Astroparticle Physics*, 34:106–115. 30

Ahn, E.-J., Engel, R., Gaisser, T. K., Lipari, P., and Stanev, T. (2009). Cosmic ray interaction event generator sibyll 2.1. *Physical Review D*, 80:094003. 28

Ahn, H. S. et al. (2010). Measurements of the Relative Abundances of High-energy Cosmic-ray Nuclei in the TeV/Nucleon Region. *The Astrophysical Journal*, 715(2):1400–1407. 27

Aloisio, R., Blasi, P., Ghia, P. L., and Grillo, A. F. (2000). Probing the structure of space-time with cosmic rays. *Physical Review D*, D62:053010. 73

Aloisio, R., Boncioli, D., Grillo, A., Petrera, S., and Salamida, F. (2012). Simprop: a simulation code for ultra high energy cosmic ray propagation. *Journal of Cosmology and Astroparticle Physics*, 2012(10):007. 21

Alves Batista, R. (2015). *On the cosmological propagation of high energy particles in magnetic fields*, pages 1–187. DESY-THESIS, Germany. 19, 21

Alves Batista, R., Dundovic, A., Erdmann, M., Kampert, K.-H., Kuempel, D., Müller, G., Sigl, G., van Vliet, A., Walz, D., and Winchen, T. (2016). CRPropa 3 - a Public Astrophysical Simulation Framework for Propagating Extraterrestrial Ultra-High Energy Particles. *Journal of Cosmology and Astroparticle Physics*, 1605(05):038. 21, 63, 74

Alves Batista, R., Erdmann, M., Evoli, C., Kampert, K.-H., Kuempel, D., Mueller, G., Sigl, G., Van Vliet, A., Walz, D., and Winchen, T. (2015). Cosmic ray propagation with CRPropa 3. *Journal of Physics: Conference Series*, 608(1):012076. 102

Armengaud, E., Sigl, G., Beau, T., and Miniati, F. (2007). CRPropa: A numerical tool for the propagation of UHE cosmic rays, γ-rays and neutrinos. *Astroparticle Physics*, 28:463–471. 100

Astronomy, J. (2013). Celestial coordinates: equatorial and galactic coordinate system. http://www.jtwastronomy.com/tutorials/celestialcoordinates.html. 98, 99

Ave, M. (2007). Reconstruction accuracy of the surface detector array of the Pierre Auger Observatory. In *Proceedings, 30th International Cosmic Ray Conference (ICRC 2007): Merida, Yucatan, Mexico*, volume 4, pages 307–310. 53

Axford, W. I., Leer, E., and Skadron, G. (1977). The acceleration of cosmic rays by shock waves. *International Cosmic Ray Conference*, 11:132–137. 9

Berezinsky, V., Gazizov, A. Z., and Grigorieva, S. I. (2005). Dip in UHECR spectrum as signature of proton interaction with CMB. *Physics Letters B*, B612:147–153. 24, 35

Bhattacharjee, P. and Sigl, G. (2000). Origin and propagation of extremely high-energy cosmic rays. *Physics Reports*, 327:109–247. 14, 30

Biermann, P. L. (1994). The Origin of cosmic rays. In *Exotic nuclei and nuclear/particle astrophysics. Proceedings, Carpathian Summer School of Physics, CSSP05, Mamaia-Constanta, Romania, June 13-24, 2005*, pages 225–232. 10

Biermann, P. L. and Sigl, G. (2001). *Introduction to Cosmic Rays*, pages 1–26. Springer Berlin Heidelberg, Berlin, Heidelberg. 5

Blaksley, C. (2014). Photodetection Aspects of JEM-EUSO and Studies of the Ultra-High Energy Cosmic Ray Sky. *ArXiv e-prints*. 13

Blasi, P. (2013). Theoretical challenges in acceleration and transport of ultra high energy cosmic rays: A review. In *European Physical Journal Web of Conferences*, volume 53 of *European Physical Journal Web of Conferences*, page 01002. 11, 12

Boratav, M., Cronin, J., and Watson, A. (1992). Preface. *Nuclear Physics B - Proceedings Supplements*, 28(2):v –. 17, 18

Bradt, H. (2004). *Astronomy methods: a physical approach to astronomical observations*. Cambridge : University Press, [15a ed.] edition. 97

Bretz, H.-P., Erdmann, M., Schiffer, P., Walz, D., and Winchen, T. (2014). Parsec: A parametrized simulation engine for ultra-high energy cosmic ray protons. *Astroparticle Physics*, 54:110 – 117. 66

Calvez, A., Kusenko, A., and Nagataki, S. (2010). Role of galactic sources and magnetic fields in forming the observed energy-dependent composition of ultrahigh-energy cosmic rays. *Physical Review Letters*, 105:091101. 34

Cazon, L., Vazquez, R. A., Watson, A. A., and Zas, E. (2004). Time structure of muonic showers. *Astroparticle Physics*, 21:71–86. 56

Chen, P., Tajima, T., and Takahashi, Y. (2002). Plasma wakefield acceleration for ultrahigh-energy cosmic rays. *Physical Review Letters*, 89:161101. 11

Chiba, N., Hashimoto, et al. (1992). Akeno Giant Air Shower Array (AGASA) covering 100 km ^{2} area. *Nuclear Instruments and Methods in Physics Research A*, 311:338–349. 14

Compton, A. H. and Getting, I. A. (1935). An apparent effect of galactic rotation on the intensity of cosmic rays. *Physical Review*, 47:817–821. 35

De Domenico, M., Settimo, M., Riggi, S., and Bertin, E. (2013). Reinterpreting the development of extensive air showers initiated by nuclei and photons. *Journal of Cosmology and Astroparticle Physics*, 1307:050. 75

de Gouveia Dal Pino, E. M. and Kowal, G. (2015). Particle Acceleration by Magnetic Reconnection. In Lazarian, A., de Gouveia Dal Pino, E. M., and Melioli, C., editors, *Magnetic Fields in Diffuse Media*, volume 407 of *Astrophysics and Space Science Library*, page 373. 11

Deligny, O. (2016). Cosmic-Ray Anisotropies: A Review. In *25th European Cosmic Ray Symposium (ECRS 2016) Turin, Italy, September 04-09, 2016*. 37

di Matteo, A. (2016). Combined fit of spectrum and composition data as measured by the Pierre Auger Observatory. *PoS*, ICRC2015:249. 3, 59, 62, 71, 73

Durrer, R. (2015). The cosmic microwave background: the history of its experimental investigation and its significance for cosmology. *Classical and Quantum Gravity*, 32(12):124007. 16

Dwek, E. and Krennrich, F. (2013). The extragalactic background light and the gamma-ray opacity of the universe. *Astroparticle Physics*, 43:112–133. 14

Ellis, J., Mayes, V. E., and Nanopoulos, D. V. (2006). Ultrahigh-energy cosmic rays particle spectra from crypton decays. *Physical Review D*, 74:115003. 30

Erdogdu, P. et al. (2006). The Dipole anisotropy of the 2 Micron All-Sky Redshift Survey. *Monthly Notices of the Royal Astronomical Society*, 368:1515–1526. 62

Fermi, E. (1949). On the origin of the cosmic radiation. *Physical Review*, 75:1169–1174. 7

Gallant, Y. A. and Achterberg, A. (1999). Ultra-high-energy cosmic ray acceleration by relativistic blast waves. *Monthly Notices of the Royal Astronomical Society*, 305:6. 10

Gelmini, G., Kalashev, O. E., and Semikoz, D. V. (2008). GZK photons as ultra high energy cosmic rays. *Journal of Experimental and Theoretical Physics*, 106:1061–1082. 30

Gialis, D. and Pelletier, G. (2004). Which acceleration process for UHE - cosmic rays in gamma-ray bursts? *Astronomy and Astrophysics*, 425:395–403. 10

Globus, N., Allard, D., Mochkovitch, R., and Parizot, E. (2015). UHECR acceleration at GRB internal shocks. *Monthly Notices of the Royal Astronomical Society*, 451(1):751–790. 10

Gorski, K. M., Hivon, E., Banday, A. J., Wandelt, B. D., Hansen, F. K., Reinecke, M., and Bartelman, M. (2005). HEALPix - A Framework for high resolution discretization, and fast analysis of data distributed on the sphere. *The Astrophysical Journal*, 622:759–771. 70

Greisen, K. (1966). End to the cosmic-ray spectrum? *Physical Review Letters*, 16:748–750. 16

Harari, D., Mollerach, S., and Roulet, E. (2010). Effects of the galactic magnetic field upon large scale anisotropies of extragalactic Cosmic Rays. *Journal of Cosmology and Astroparticle Physics*, 1011:033. 35

Harari, D., Mollerach, S., and Roulet, E. (2013). On the large scale anisotropies of extragalactic cosmic rays. *GAP 2013-025*. 62

Harari, D., Mollerach, S., and Roulet, E. (2014). Anisotropies of ultrahigh energy cosmic rays diffusing from extragalactic sources. *Physical Review*, D89(12):123001. 16

Haungs, A., Blumer, J., and et al. (2015). KCDC The KASCADE Cosmic-ray Data Centre. In *Journal of Physics Conference Series*, volume 632 of *Journal of Physics Conference Series*, page 012011. 26

Hauser, M. G. and Dwek, E. (2001). The Cosmic Infrared Background: Measurements and Implications. *Annual Review of Astronomy and Astrophysics*, 39:249–307. 14

Hillas, A. M. (1972). *Cosmic rays*. Oxford ; New York : Pergamon Press, [1st ed.] edition. 5

Hillas, A. M. (1984). The Origin of Ultra-High-Energy Cosmic Rays. *Annual Review of Astronomy and Astrophysics*, 22:425–444. 11

Hillas, A. M. (2006). Cosmic Rays: Recent Progress and some Current Questions. In *Conference on Cosmology, Galaxy Formation and Astro-Particle Physics on the Pathway to the SKA Oxford, England*. 24

Hoerandel, J. R. (2003). On the knee in the energy spectrum of cosmic rays. *Astroparticle Physics*, 19:193–220. 23

J. J. Beatty, J. M. and Wakely, S. (2015). Cosmic rays. http://pdg.lbl.gov/2016/reviews/rpp2016-rev-cosmic-rays.pdf. 22, 23

Janossy, L. (1950). *Cosmic rays*. Oxford At The Clarendon Press. Osmania University. 5

Jansson, R. and Farrar, G. R. (2012a). A New Model of the Galactic Magnetic Field. *The Astrophysical Journal*, 757:14. 20

Jansson, R. and Farrar, G. R. (2012b). The Galactic Magnetic Field. *The Astrophysical Journal*, 761:L11. 20

Kalashev, O. E., Rubtsov, G. I., and Troitsky, S. V. (2009). Sensitivity of cosmic-ray experiments to ultra-high-energy photons: reconstruction of the spectrum and limits on the superheavy dark matter. *Physical Review*, D80:103006. 30

Kamata, K. and Nishimura, J. (1958). The Lateral and the Angular Structure Functions of Electron Showers. *Progress of Theoretical Physics Supplement*, 6:93–155. 53

Kampert, K.-H., Kulbartz, J., Maccione, L., Nierstenhoefer, N., Schiffer, P., Sigl, G., and van Vliet, A. R. (2013). CRPropa 2.0 - A public framework for propagating high energy nuclei, secondary gamma rays and neutrinos. *Astroparticle Physics*, 42:41–51. 100

Kampert, K.-H. and Watson, A. A. (2012). Extensive air showers and ultra high-energy cosmic rays: a historical review. *European Physical Journal H*, 37:359–412. 5

Kawai, H., Yoshida, S., Yoshii, H., Tanaka, K., Cohen, F., Fukushima, M., Hayashida, N., Hiyama, K., Ikeda, D., Kido, E., et al. (2008). Telescope array experiment. *Nuclear Physics B-Proceedings Supplements*, 175:221–226. 47

Kirk, J. G., Skjøraasen, O., and Gallant, Y. A. (2002). A wind model for high energy pulses. In Becker, W., Lesch, H., and Trümper, J., editors, *Neutron Stars, Pulsars, and Supernova Remnants*, page 136. 11

Knurenko, S., Petrov, I., Petrov, Z., and Sleptsov, I. (2016). The spectrum of cosmic rays in the energy range $10^{16} - 10^{18} eV$ according to the Small Cherenkov Array in Yakutsk. *PoS*, ICRC2015:252. 23

Kolb, E. W., Chung, D. J. H., and Riotto, A. (1999). WIMPZILLAS! In Klapdor-Kleingrothaus, H. V. and Baudis, L., editors, *Dark matter in Astrophysics and Particle Physics*, page 592. 14

Kotera, K. and Olinto, A. V. (2011). The Astrophysics of Ultrahigh-Energy Cosmic Rays. *Annual Review of Astronomy and Astrophysics*, 49:119–153. 17, 20

Lemoine, M. and Pelletier, G. (2003). Particle transport in tangled magnetic fields and Fermi acceleration at relativistic shocks. *The Astrophysical Journal*, 589:L73–L76. 10

Lemoine, M., Pelletier, G., and Revenu, B. (2006). On the efficiency of Fermi acceleration at relativistic shocks. *The Astrophysical Journal*, 645:L129–L132. 10

Martirosov, R. (2011). Energy spectrum and mass composition of primary cosmic radiation in the region above the knee from the GAMMA experiment. *International Cosmic Ray Conference*, 1:178. 23

Matthews, J. (2005). A Heitler model of extensive air showers. *Astroparticle Physics*, 22:387–397. 26

Milgrom, M. and Usov, V. (1995). Possible association of ultrahigh-energy cosmic ray events with strong gamma-ray bursts. *Astrophysical Journal*, 449:L37. 13

Newton, D., Knapp, J., and Watson, A. A. (2007). The Optimum Distance at which to Determine the Size of a Giant Air Shower. *Astroparticle Physics*, 26:414–419. 53

Ostapchenko, S. (2014). Lhc data on inelastic diffraction and uncertainties in the predictions for longitudinal extensive air shower development. *Physical Review D*, 89:074009. 28

Pelletier, G., Lemoine, M., and Marcowith, A. (2009). On Fermi acceleration and MHD-instabilities at ultra-relativistic magnetized shock waves. *Monthly Notices of the Royal Astronomical Society*, 393:587. 10

Pierog, T., Karpenko, I., Katzy, J. M., Yatsenko, E., and Werner, K. (2015). EPOS LHC: Test of collective hadronization with data measured at the CERN Large Hadron Collider. *Physical Review Letters*, C92(3):034906. 28, 75

Pierre Auger Collaboration, Abraham, J., Abreu, P., Aglietta, M., Aguirre, C., Ahn, E. J., Allard, D., Allekotte, I., Allen, J., Allison, P., and et al. (2009). Upper limit on the cosmic-ray photon fraction at EeV energies from the Pierre Auger Observatory. *Astroparticle Physics*, 31:399–406. 13

Porcelli, A. (2015). Measurements of x_{max} above 10^{17} ev with the fluorescence detector of the pierre auger observatory. In *Proceedings of the 34th International Cosmic Ray Conference (ICRC 2015): The Hague, Netherlands*. 75

Protheroe, R. J. (1999). Acceleration and interaction of ultra high energy cosmic rays. In Duvernois, M. A., editor, *Topics in Cosmic-Ray Astrophysics*, volume 230, page 247. 7, 9

Pshirkov, M. S., Tinyakov, P. G., Kronberg, P. P., and Newton-McGee, K. J. (2011). Deriving the global structure of the galactic magnetic field from faraday rotation measures of extragalactic sources. *The Astrophysical Journal*, 738(2):192. 20

Ptuskin, V. S., Rogovaya, S. I., Zirakashvili, V. N., Chuvilgin, L. G., Khristiansen, G. B., Klepach, E. G., and Kulikov, G. V. (1993). Diffusion and drift of very high energy cosmic rays in galactic magnetic fields. *Astronomy and Astrophysics*, 268:726–735. 35

R. A. Batista, F. C. et al. (2017). A combined fit of spectrum and composition Auger data considering a very simple case of Lorentz Invariance Violation along the cosmic ray propagation. *GAP 2017-012*. 2, 82

R. M. de Almeida, C. A. V. V. et al. (2017). Phenomenological analysis of the large scale anisotropies measured by the Pierre Auger Collaboration considering Lorentz Invariance Violation. *GAP 2017-016*. 2, 82

Schulz, A. (2013). The measurement of the energy spectrum of cosmic rays above 3×10^{17} ev with the pierre auger observatory. In *Proceedings of the 33th International Cosmic Ray Conference (ICRC 2013): Rio de Janeiro, Brazil*. 75

Sigl, G., Lee, S., Bhattacharjee, P., and Yoshida, S. (1999). Probing grand unified theories with cosmic ray, gamma-ray and neutrino astrophysics. *Physical Review*, D59:043504. 30

Smoot, G. F. (2007). Nobel lecture: Cosmic microwave background radiation anisotropies: Their discovery and utilization*. *Reviews of Modern Physics*, 79:1349–1379. 16

Smoot, G. F. and Scott, D. (1996). The Cosmic Background Radiation. *ArXiv Astrophysics e-prints*. 14

Sokolsky, P. and HiRes Collaboration (2011). Final Results from the High solution Fly's Eye (HiRes) Experiment. *Nuclear Physics B Proceedings Supplements*, 212:74–78. 41

Souza de Oliveira, J. (2016). *Estudo em multiresolução de anisotropias nas direções de chegada dos raios cósmicos detectados no Observatório Pierre Auger*. THESIS, Brasil. 37, 38, 61, 65, 66

Stanev, T. (2010). *High Energy Cosmic Rays*. Springer Science Business Media, Science Business Media. 5, 20

Stanev, T., Engel, R., Mucke, A., Protheroe, R. J., and Rachen, J. P. (2000). Propagation of ultrahigh-energy protons in the nearby universe. *Physical Review*, D62:093005. 19

Sveshnikova, L. G., Strelnikova, O. N., and Ptuskin, V. S. (2013). Spectrum and Anisotropy of Cosmic Rays at TeV-PeV-energies and Contribution of Nearby Sources. *Astroparticle Physics*, 50-52:33–46. 23

Thompson, C. (2006). Deceleration of a Relativistic, Photon-rich Shell: End of Preacceleration, Damping of Magnetohydrodynamic Turbulence, and the Emission Mechanism of Gamma-Ray Bursts. *The Astrophysical Journal*, 651:333–365. 11

Tinyakov, P. (2014). Latest results from the telescope array. *Nuclear Instruments and Methods in Physics Research Section A: Accelerators, Spectrometers, Detectors and Associated Equipment*, 742:29 – 34. 4th Roma International Conference on Astroparticle Physics. 24

Valino, I. (2016). The flux of ultra-high energy cosmic rays after ten years of operation of the Pierre Auger Observatory. *PoS*, ICRC2015:271. 25

Véron-Cetty, M.-P. and Véron, P. (2006). A catalogue of quasars and active nuclei: 12th edition. *Astronomy and Astrophysics, EDP Sciences*, 455:773–777. 32

Wilson, J. G. J. G. (1976). *Cosmic rays*. London; Wykeham Publications; Andover. Distributed in the Western Hemisphere by Springer Verlag, New York. 5

Wolfendale, A. W. (1984). Cosmic rays of very high energy. *Reports on Progress in Physics*, 47:655–706. 5

Yoshida, S. et al. (1994). Lateral distribution of charged particles in giant air showers above 1 eev observed by agasa. *Journal of Physics G: Nuclear and Particle Physics*, 20(4):651. 47

Zatsepin, G. T. and Kuzmin, V. A. (1966). Upper limit of the spectrum of cosmic rays. *Journal of Experimental and Theoretical Physics Letters*, 4:78–80. [Pisma Zh. Eksp. Teor. Fiz.4,114(1966)]. 16

Zweibel, E. G. and Yamada, M. (2009). Magnetic reconnection in astrophysical and laboratory plasmas. *Annual Review of Astronomy and Astrophysics*, 47(1):291–332. 10

Appendix A

Celestial Coordinates

It is helpful to understand how to locate celestial objects as they move across the sky. A celestial coordinate system was created thatmaps an imaginary sphere surrounding the Earth upon which all stars appear to be placed. To specify the position of a point on the celestial sphere being observed from Earth, such as the position of a cosmic ray source, different coordinates are needed.

A.1 Local Coordinates

System of coordinates defined by the experiment to represent the arrival direction of a cosmic ray from two angles. The zenith angle θ, is angle between the axis of the shower and a vertical line perpendicular to the plane of the experiment, with $\theta = 0$ in case of a vertical shower. The zenith angle varies from 0 to 90°. The coordinate system is completely defined with the determination of the azimuth angle ϕ, the angle that the axis of the shower makes around the vertical, in the plane of he experiment. Starting with $\phi = 0$ (the definition is arbitrary). Once a reference direction has been chosen, this angle varies up to 360°. Local coordinates, however, may also be given in altitude *alt* and azimuth angle, where the altitude is the elevation of an object.

This coordinate system is also known as the horizontal coordinate system because the angles are defined from the horizontal plane where the experiment is located.

Figure A.1 shows the local coordinate system used at the Pierre Auger Observatory. The angles measured locally are the two experimental quantities which we have access. The positions of celestial objects depend on the observer position and the time of observation. Thus, the local reference frame is inappropriate as a coordinate system for determining celestial positions and it difficult to study cosmic ray anisotropy because every moment the experiment is observing differents parts of the sky. Thus, it is necessary to use other coordinate system that eliminate this dependence temporal.

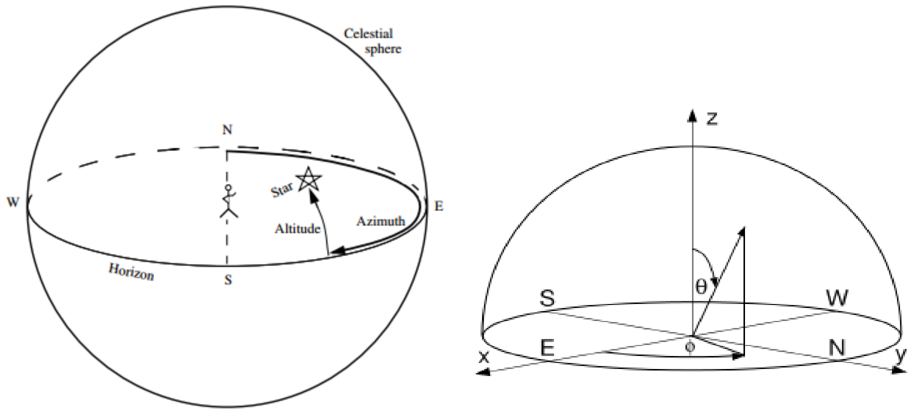

FIGURE A.1: Local coordinate system. **Left:** The objects are located with two angles the altitude alt and the azimuth ϕ. **Right:** Representation of the local coordinate system that defines the direction of arrival of a cosmic ray on Earth. [Bradt, 2004].

A.2 Equatorial Coordinates

The position of a celestial object can be specified independently of time and observer position in an equatorial reference frame, see figure . Equatorial coordinates are spherical and the reference plane is given by the Earth's equatorial plane, identified by all observers, regardless of where they are on that surface. The equator is the circle determined by the intersection of the celestial sphere with the plane formed by the terrestrial equator.

The latitudinal angle of the equatorial system is called Declination (δ). It measures the angle of an object above or below the celestial equator. The longitudinal angle

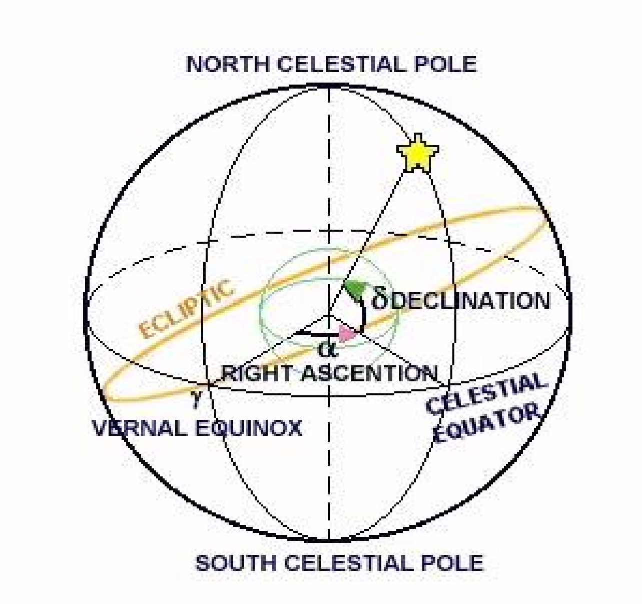

FIGURE A.2: Representation of the equatorial coordinates system. [Astronomy, 2013].

is called the Right Ascension (α). It measures the angle of an object East of the Vernal Equinox[1] γ. Unlike longitude, Right Ascension is usually measured in hours instead of degrees, because the apparent rotation of the equatorial coordinate system is closely related to Local Sidereal Time (LST) and Hour Angle (h).

The equatorial coordinate system is used in the study of cosmic ray anisotropy, making it possible to compare the directions of arrival these particles with the position of astrophyisical objects. From the local angles and the instant t of observing an event, the conversion of local coordinate system to the equatorial system can be done.

A.3 Galactic coordinates

The galactic coordinate system also identifies positions in the sky without the temporal dependence of the horizontal coordinates and for that reason they are used in

[1]the Vernal Equinox is the point on the celestial sphere in which the celestial equator and the ecliptic intersect. The ecliptic is an imaginary great circle on the celestial sphere along which the Sun appears to move over the course of a year.

anisotropy studies. As a definition of the equatorial plane, this coordinate system uses the projection of the plane of the galaxy on the celestial sphere. Similarly to the systems shown above, there are two angles that are defined in relation to this plane: Galactic latitude b and galactic longitude l. The galactic center has the coordinates $(1, b) = (0°, 0°)$ in the galactic system and $(\alpha, \delta) = (266.3°, -29.0°)$ in the celestial equatorial system.

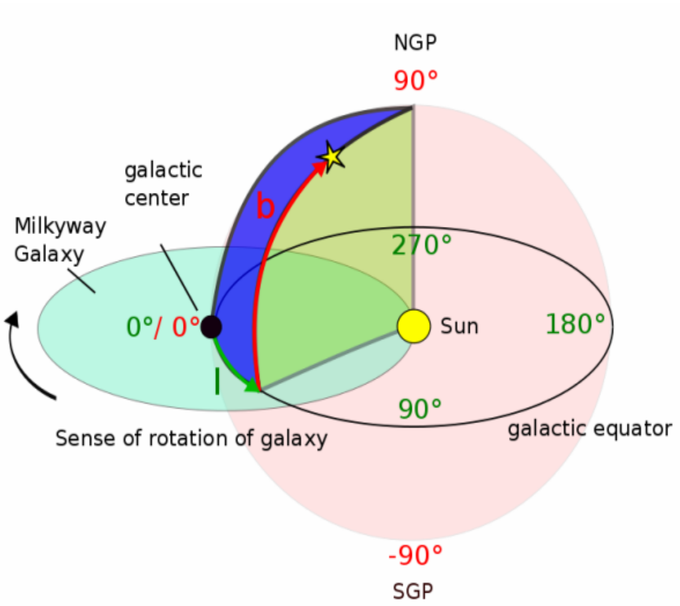

FIGURE A.3: Representation of the Galactic coordinates system. [Astronomy, 2013].

Appendix B

CRPROPA 3.0

CRPropa is a publicly available software package designed to simulate the extragalactic propagation of UHECRs and their secondaries. A numerical tool that is able to simulate the deviations and interactions of UHECRs in several orders of magnitude in energy and length scales, ranging from thousands of megaparsecs to galactic scales of the order of kiloparsecs. It is CRPropa version 3.0. CRPropa 3.0 aims to interpret experimental data available from UHECRs above 10^{17} eV in the context of realistic concrete astrophysical scenarios. Currently the propagation can be done in one (1D), three (3D) or four dimensions (4D). This version consists on a completely redesign of the previous ones, CRPropa [Armengaud et al., 2007] and CRPropa 2 [Kampert et al., 2013],[A. van Vliet et al., 2013], and is highly modular, with many new features, namely: parallel processing; Python steering; four-dimensional propagation; new models of CIB; propagation in the galactic magnetic field; galactic magnetic field lensing; enhanced calculation of interaction rates.

With the CRPropa program, the measured UHECR data, as well as secondary neutrino spectra and secondary photons can be tested in specific astrophysical scenarios for the distribution of sources, their injection characteristics such as energy spectrum, maximum energy and mass composition. It includes all relevant interactions such as photodisintegration, photo-pion production, pair production and nuclear decay, the magnetic field deflections and cosmological evolutionary effects (redshift).

More information on CRPropa 3.0 can be obtained at https://crpropa.desy.de. Information on downloading the code, usage and example applications can be found at .

For the cosmic rays propagation part in CRPropa 3.0 is composed of independent modules that access and modify a candidate cosmic ray. Due to this modular structure all parts of the software can be used and tested individually. As there are no direct dependencies between the modules, it is possible to select a combination of modules, allowing to use and study in detail the individual photo-nuclear interactions, boundary conditions, observers, etc.

The single interface between the modules is the cosmic ray candidate class. The simulation modules provide a method to update the cosmic ray particle according to the module's purpose. These cosmic-ray candidates contain information about all aspects of their propagation: the particle states at different times, a list of created secondary particles and their properties, a list of states for stochastic interactions, a list of arbitrary properties and some module specific information. All information about the propagation state, including the states of the modules, is stored in the cosmic-ray candidates themselves. In this way modules can process multiple cosmic rays at the same time, which is required for high performance parallel computing. Cosmic ray candidates can be created manually or by a modular source model class, in which source properties such as position, energy spectrum and composition are included. The simulation itself is a user-defined sequence of simulation modules, that are called in turn to update the cosmic ray candidate until the propagation is completed.

CRPropa 3 is written in C++ and interfaced to Python using SWIG[1]. This allows the user to set up and steer simulations in a high level scripting language while all computations are performed with the underlying C++ code. The SWIG interface enables cross-language polymorphism, which can be used to extend a CRPropa simulation directly from the Python script that runs it. The user can for example

[1]SWIG is an interace compiler for cross-language polymorphism, making it possible for codes written, for example, in C++ to be extended to other language such as Python, allowing one to tailor the wrapping process as desired. It is available in www.swig.org

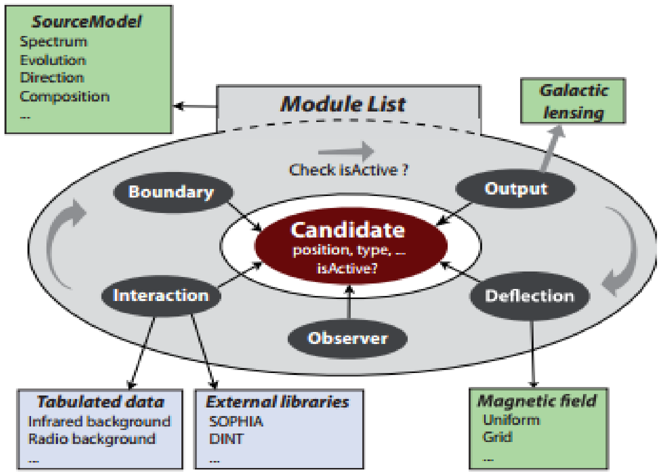

FIGURE B.1: Illustration of the CRPropa 3.0 modular structure. Each module contained in the module list acts on the candidate class. [Alves Batista et al., 2015].

write a custom simulation module in Python to be used in combination with the existing C++ modules.